Pt

protective Cr_2O_3

W-matrix

internal Cr_2O_3

Cr-rich phase

1 µm

Studies of oxidation resistant tungsten alloys at temperatures of 1100 K to 1475 K

Felix Klein

JÜLICH
Forschungszentrum

Studies of oxidation resistant tungsten alloys at temperatures of 1100 K to 1475 K

Felix Klein

1. Gutachter:

        Prof. Dr. Christian Linsmeier

2. Gutachter:

        Prof. Dr. Achim von Keudell

Tag der Disputation: 06.11.2019

Inhaltsangabe

Elektrizität aus Kernfusion ist ein aussichtsreicher Ansatz. Ein Unfallszenario eines Kraftwerkes nimmt einen Kühlmittelausfall und ein beschädigtes Reaktorgefäß an. In diesem Fall werden Temperaturen der plasmazugewandten Materialien von über $1200\,K$ erwartet. Diese Arbeit untersucht W-Cr-Y Legierungen, um Sicherheit nach einem solchen Unfall zu gewährleisten. Es wird gezeigt wie Cr durch Diffusion eine Oxidschicht bildet, die die Freisetzung von WO_3 bei bis zu $1273\,K$ in trockener und feuchter Luft unterdrückt. Eine Unterdrückung um mehr als eine Größenordnung gegenüber W wird zum ersten Mal gemessen. Y ist essentiell zur Unterdrückung der Freisetzung von WO_3 und wird erstmals an den Oxidkorngrenzen und in Form von $YCrO_3$ Nanopartikeln nachgewiesen. Ein Verständnis der Oxidation in Abhängigkeit der Morphologie, Mikrostruktur, Zusammensetzung und Umgebungsbedingungen durch experimentelle und theoretische Untersuchungen der Wechselwirkungen der beteiligten Elemente wird entwickelt.

Schlagworte

Fusion, Erste-Wand, Wolfram, Legierung, Sublimation, Oxidation, Sicherheit

Abstract

Electricity from nuclear fusion is a promising approach. An accidental scenario of a fusion power plant assumes a loss of coolant and a damaged reactor vessel. In this case temperatures beyond $1200\,\mathrm{K}$ of the plasma-facing materials are expected. This thesis investigates W-Cr-Y alloys to provide safety after such an accident. It is shown how Cr forms an oxide layer by diffusion that suppresses the release of WO_3 at temperatures up to $1273\,\mathrm{K}$ in dry and humid air. Suppression by more than one order of magnitude as compared to W is measured for the first time. Y is essential for suppression of WO_3 release and is detected for the first time at the oxide grain boundaries and in the form of $YCrO_3$ nano-particles. An understanding of the oxidation in dependence on morphology, microstructure, composition and the environmental conditions is developed using experimental and theoretical studies of the interaction of the involved elements.

Keywords

Fusion, First-Wall, Tungsten, Alloy, Sublimation, Oxidation, Safety

Contents

Chapter 1

Introduction

1.1 Nuclear fusion and its material requirements

Climate change is one of the key challenges of our generation. Reduction of the emission of greenhouse gases such as carbon dioxide (CO_2) reduces the risk of severe consequences from climate change. Electricity generation currently attributes to around $12\,\%$ of the CO_2 emissions world wide [1]. Therefore, science should consider all available options to generate electricity emitting as little greenhouse gases as possible and draw conclusions after exploring the opportunities.

From current knowledge, there are three main primary energy sources: fossil fuels, renewable energy sources, and nuclear energy. New technologies can improve the efficiency of electricity generation from fossil fuels. However, greenhouse gas emissions will remain. Renewable energy sources such as wind, solar, and hydro-power are an important field of research. However, there are large fluctuations in availability of those sources. This creates challenges for the grid and the need for storage solutions [2]. The higher the fraction of electricity from renewable sources, the bigger is the technological challenges for the grid and the storage. Research is needed in that field.

Nuclear energy is the third option. The public acceptance of nuclear energy is poor in some countries such as Germany due to nuclear waste and accidents in Tschernobyl and Fukushima [3]. All nuclear power plants in operation are and were fission power plants. Indeed the problem of the nuclear waste from fission power plants is not solved. However, new research continuously improves the safety of fission power plants [4]. In public debates, it is often forgotten that the field of nuclear energy should be separated into fission and fusion. Fission relies on splitting a large nucleus into smaller parts, whereas fusion relies on merging/fusing two small nuclei. Thus, there is a fundamental difference between the physics of fission and fusion. One consequence is that the reaction products of a fusion reaction are not radioactive. Thus, long-term radioactive waste can be avoided in a fusion power plant, unlike in a fission power plant [5]. Another consequence is that fusion power plants are inherently safe [5].

Inherent safety is given as a fusion power plant requires a magnetically confined plasma in a vacuum vessel [6]. An uncontrolled fusion process in case of an accident is not possible, the plasma will immediately collapse in case of air ingress. In order to have an efficient fusion power plant, the required plasma-heating energy should be minimized whereas the reaction rate of the fusion process should be maximized. Therefore, a fusion power plant based on the reaction of the hydrogen isotopes deuterium (D) and tritium (T) is the most

probable option:

$$\,_1^2D + \,_1^3T \rightarrow \,_2^4He\,(3.5\,\text{MeV}) + \,_0^1n\,(14.1\,\text{MeV}) \tag{1.1}$$
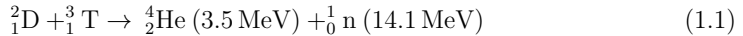
In the temperature range of $10\,\text{keV}$ to $20\,\text{keV}$ the reaction rate is above $1 \times 10^{-22}\,\text{m}^3\,\text{s}^{-1}$ [7] and the cross section for the reaction is above $1 \times 10^{-2}\,\text{b}$ [8]. The hydrogen isotopes must be magnetically confined and heated to that temperature. After ignition of the plasma the fusion power plant must run self-sustaining, i.e. the heat released from the reactions in the plasma must substitute external heating systems. This requirement is expressed using the the fusion triple product. The condition for the fusion triple product in a D-T plasma is as follows:

$$n\,\tau\,T \geq 3 \times 10^{21}\,\text{m}^{-3}\,\text{s}\,\text{keV} \tag{1.2}$$

where n is the plasma density, τ is the energy confinement time and T the temperature [9].

This work assumes a fusion power plant with a well confined and controlled plasma. In such a case there are still challenges such as the material selection for the first wall of the vacuum vessel. In a demonstration power plant (DEMO) a heat load of up to $1\,\text{MWm}^{-2}$ is foreseen on the first wall [10]. Another peculiarity of a fusion power plant are the $14.1\,\text{MeV}$ neutrons reaching the wall materials. These conditions impose multiple requirements on the material selection [11]:

- The material requires a high thermal conductivity and a high melting point to handle the heat load.

- The material requires a low erosion yield from the incoming plasma particles to ensure a long lifetime and to minimize the contamination of the plasma by impurities from the wall.

- The material requires a low hydrogen retention. Otherwise, radioactive tritium trapped inside the wall causes a radiological hazard. Further, the tritium in the wall is lost for the fusion process.

- The material requires resistance towards neutron irradiation. Neutron irradiation causes the displacement of atoms in the material and transmutations by nuclear reactions. Transmutations lead to a change in the chemical composition and activation of materials. The resistance implies that the properties of the material do not change significantly with neutron irradiation and that the material can be recycled within 100 years after shut-down of the power plant.

- The material requires to be stable in any abnormal event. A potential necessity for an evacuation of people living in the surrounding of the power plant must be excluded. Failure of all active cooling systems and cracking of the vacuum vessel is one possible abnormal event.

1.2 Tungsten alloys

The main candidate for the plasma-facing material in future fusion power plants is currently tungsten (W). It fulfills already multiple requirements listed in section 1.1: the thermal conductivity at room temperature of $1.75\,\mathrm{W\,cm^{-1}\,K^{-1}}$ [12] and the melting point of $3663\,\mathrm{K}$ [13] are sufficiently high. W is a heavy element resulting in a low erosion yield. A sufficiently low tritium retention was measured - the retained hydrogen in the wall is reduced by a factor of 100 to 1000 if a full W plasma-facing wall is used as compared to a full C plasma-facing wall [14]. The neutron-induced activity of W decays to the hands-on level of $10\,\mathrm{\mu Sv\,h^{-1}}$ within 100 years meeting the requirement of recycle-ability within 100 years [15]. Neutron-induced embrittlement and the intrinsic brittleness of W are an important field of research [16]. The safety of the power plant in case of an accident is another field.

The accident scenario involves a total loss of active cooling and simultaneous air ingress into the vacuum vessel (LOCA). The air influx will cause the plasma to switch off, no chain reaction is possible. However, the activated wall heats up due to the nuclear decay heat of the wall itself. In the absence of active cooling a temperature above $1200\,\mathrm{K}$ will be reached after three days and held for several weeks [17]. W will form WO_3. WO_3 is volatile under these conditions and radioactive W can be released to the environment.

At $1473\,\mathrm{K}$ in humid air a WO_3 sublimation rate of $3.68 \times 10^{-2}\,\mathrm{mg\,cm^{-2}\,s^{-1}}$ is reported [18]. A first wall armor with a surface area of $1000\,\mathrm{m^2}$, a thickness of $2\,\mathrm{mm}$ and a mass of $4 \times 10^4\,\mathrm{kg}$ is mobilized in less than $2\,\mathrm{days}$. Potentially a fraction of that material deposits onto cooler parts of the reactor before being released to the environment. However, this fraction depends on the details of the accident and a reliable safety concept should not be based on deposition of already mobilized W. The expected activity of W at the first wall after $5\,\mathrm{full\,power\,years}$ (fpy) is $8.74 \times 10^{14}\,\mathrm{Bq\,kg^{-1}}$ [19]. In comparison, the total release in the nuclear accident from Fukushima is estimated at $5.2 \times 10^{17}\,\mathrm{Bq}$ excluding noble gases [20]. In summary, a LOCA would be a major nuclear accident and solutions must be found to passively mitigate the consequences.

Smart alloys as armor material could improve safety in case of a LOCA. The concept is schematically illustrated in Fig. 1.1. For normal operation of the fusion power plant, the alloy shall possess the beneficial properties of W as mentioned above. During plasma

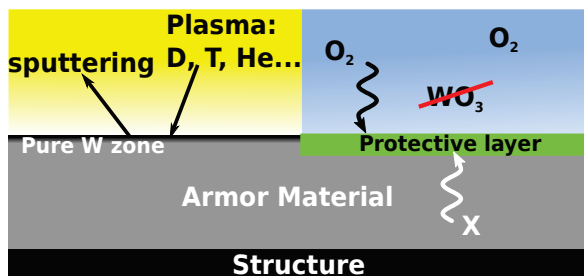Figure 1.1: Schematic working principle of smart alloys. On the left, during operation of the power plant the material shall behave as normal W which is achieved by formation of a pure W zone due to preferential sputtering of the lighter alloying elements X. On the right, after a LOCA, the alloying elements X shall diffuse to the surface to passively form a protective oxide layer suppressing the sublimation of WO_3.

exposure the lighter alloying elements are preferentially sputtered at the surface [21]. Consequently, there is an almost pure W layer at the surface and a concentration gradient in the alloying elements. The concentration gradient causes diffusion of the alloying elements to the surface where they are sputtered again. Equilibrium is reached with a depletion zone of a few tens of nanometers [21].

In case of a LOCA the plasma switches off and sputtering stops but diffusion of the alloying elements to the surface continues. The higher temperature compared to the normal operation of the power plant allows a higher mobility of the alloying elements [22]. The diffusion of alloying elements to the surface yields a protective oxide layer stopping the sublimation of WO_3.

First research on the oxidation behavior of W was published in 1929. Parabolic oxidation kinetics were found in the temperature range of 973 K to 1273 K in air [23]. Different oxidation kinetics, including parabolic oxidation, are introduced in section 1.3. Overall, [23] found an increase of the parabolic oxidation rate with temperature. However, abnormal behavior was observed in the temperature range of 1120 K to 1170 K where the permeability of oxygen in tungsten oxide changes due to modification of the tungsten oxide.

First attempts to improve the oxidation resistance by alloying with chromium (Cr) were made in 1949 at temperatures of 1323 K and 1523 K. Research concluded that the material is not suitable for industrial application due to the formation of volatile oxides [24]. Still, W fibre reinforced metals [25] and superalloys [26] remained a topic of research. The surrounding material protects the W fibres from oxidation while they improve the mechanical stability. Advantages of W fibres are the high melting point of W, the high thermal conductivity, and the low chemical reactivity with surrounding metals.

Different phase diagrams were published: in 1980 the ternary phase diagram W-Cr-O at 1273 K as shown in Fig. 1.2 a was acquired by detecting the phases present after equilibration in evacuated silica capsules using metallographic and X-ray identification [27]. At high chemical potentials of oxygen $\Delta\mu_{O_2}$ Cr_2WO_6 is formed. Depending on the elemental concentration, the remaining material forms WO_3 or Cr_2O_3. At intermediate chemical potentials of oxygen $CrWO_4$ and under-stoichiometric W oxides or Cr_2O_3 form. At low chemical potentials of oxygen around $-100\,\mathrm{kcal\,mol^{-1}}$ only Cr_2O_3 is formed. The remaining Cr goes into solid solution into a W-rich phase α''. Below a chemical potential of oxygen of $\Delta\mu_{O_2} = -127\,\mathrm{kcal\,mol^{-1}}$, corresponding to a partial oxygen pressure $p_{O_2} = 10^{-22}\,\mathrm{mbar}$, no more oxides form.

In 1984 the binary phase diagram W-Cr as shown in Fig. 1.2 b was published [28]. X-ray measurements for a solid solution in dependence of temperature and atomic composition were collected from various studies (as indicated in Fig. 1.2 b). A solid solution of W and Cr is energetically favorable in the $(\alpha Cr, W)$ region, while two phases form in the $(\alpha' + \alpha'')$ region. The melting temperature decreases with increasing Cr content as shown in Fig. 1.2 b.

A new boost for research on W alloys was the potential application in nuclear fusion. A first publication appeared in 2007. Koch and Bolt studied the oxidation behavior of W-Si thin films [22]. However, W and Si form brittle intermetallic phases [29]. Therefore, research shifted to Si free alloys. Alternatives to Si as alloying element were searched and multiple different alloying elements were tested. The most promising composition turned out to be W alloyed with 14 weight (wt.) % Cr and 2 wt. % Ti - in the following written as W-14Cr-2Ti [29]. Alternatively, it is possible to give the concentration in atomic (at.) % where the ratio is not determined by the weight of each element but by the number of
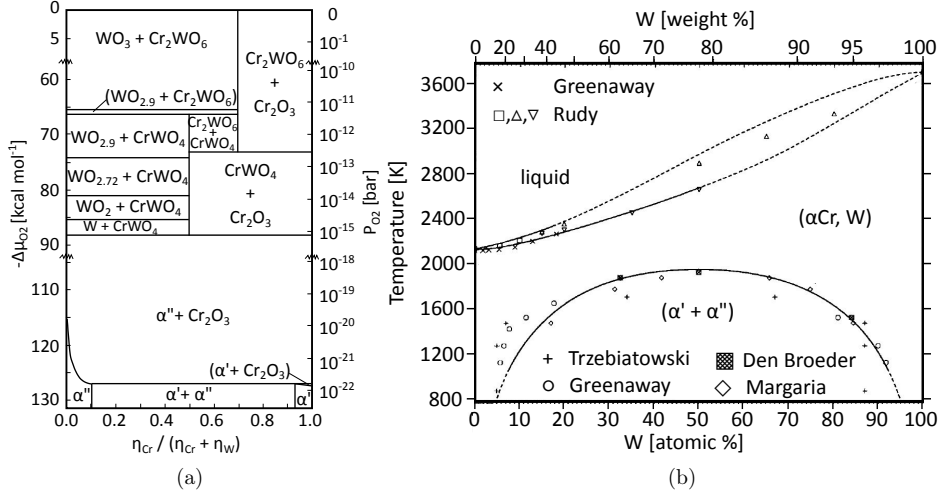
Figure 1.2: (**a**) Ternary phase diagram of W, Cr, and O at $1273\,\mathrm{K}$ where $\Delta\mu_{O_2}$ is the chemical potential of oxygen, α' the Cr-rich solid solution phase, α'' the W-rich solid solution phase, and η_{Cr}, η_W are the atomic concentration of Cr and W, respectively. p_{O_2} is the partial oxygen pressure in bar. Figure adapted from Jacob [27] (**b**) Binary phase diagram of W and Cr. Figure adapted from Naidu [28], data taken from Greenaway [31], Rudy [32], Trzebiatowski [33], Den Broeder [34], and Margaria [35].

atoms of each element.

A later study found a significant improvement of the oxidation resistance by substituting Ti by Y. Systematic variation of the elemental content yielded the optimum composition of W-11.4Cr-0.6Y [30]. All these studies were based on thin films deposited by magnetron sputtering.

Neutron irradiation in a fusion power plant causes transmutation and activation of the wall materials which must be considered when selecting the alloying elements. Assuming 5 fpy of operation of a fusion power plant such as DEMO, the activity of different elements 100 years after shut-down is given in table 1.1. All considered elements fall below the remote recycling limit expected for fusion reactor components of $10\,\mathrm{mSv\,h^{-1}}$ [36] within 100 years. W, Cr, and Y fall even below the hands-on recycling limit of $1 \times 10^{-2}\,\mathrm{mSv\,h^{-1}}$ [36]. Thus, W, Cr, Y, and Ti are suitable for application in a fusion power plant.

Table 1.1: Activity of selected elements 100 years after being exposed to the neutron flux in a DEMO-like fusion power plant for 5 fpy. Data taken from Gilbert et al. [19].

	W	Cr	Y	Ti
Activity [mSv h^{-1}]	2.05×10^{-2}	6.72×10^{-8}	2.82×10^{-7}	1.79×10^{-1}

Consequently, sintering of bulk alloys with the most promising compositions W-15Cr, W-10Cr-2Ti, and W-12Cr-0.5Y was conducted. Powder mechanical alloying followed by Hot Isostatic Pressing (HIP) was used [37]. It was found that both Ti and Y inhibit grain growth during the HIP process. The W-10Cr-2Ti alloy was able to withstand a power density of $2\,\mathrm{MW\,m^{-2}}$. First oxidation tests at $1073\,\mathrm{K}$ showed the most promising

oxidation resistance for W-12Cr-0.5Y, a linear oxidation rate of $3.1 \times 10^{-6}\,\mathrm{mg\,cm^{-2}\,s^{-1}}$ was measured for $40\,\mathrm{h}$ [37]. Y-rich oxide nano-particles were observed at the grain boundaries. However, the effect of Y and the details of the oxidation mechanisms were poorly understood. Testing of the material was performed in dry air below $1100\,\mathrm{K}$ for less than 2 days. This thesis will improve the understanding of the oxidation process and include testing in humid air and at temperatures above $1200\,\mathrm{K}$ for more than a week.

The benefits of Y on the oxidation resistance are already known from other alloys/steels [38, 39, 40] and summarized in the following. The reaction of Y and O_2 to Y_2O_3 at $1273\,\mathrm{K}$ has a Gibbs free energy $\Delta G_{Y_2O_3}(T = 1273\,\mathrm{K}) = -1 \times 10^3\,\mathrm{kJ/(mol\,O_2)}$ [41], which is much lower than for example iron (Fe) with a Gibbs free energy of $\Delta G_{Fe_2O_3}(T = 1273\,\mathrm{K}) = -3 \times 10^2\,\mathrm{kJ/(mol\,O_2)}$ for the reaction of Fe and O_2 to Fe_2O_3 [41]. Thus, the affinity of Y to oxygen O is higher as compared to Fe. As a result Y binds free O and is found as yttria particle at the grain boundaries. This can help to stabilize a desired grain structure [42]. Further, the most stable sulfur (S) containing compound in the presence of Y and O is Y_2O_2S [43]. Thus, S which is reported to destabilize protective oxide layers [44] is also bound by Y.

In case of chromia-forming alloys Y is found to alter the diffusion constants, the diffusion rate of both O and Cr in the chromia scale are reduced [45]. Further, Y is reported to improve the adherence of the oxide scale by mainly two mechanisms: first, Y can cause the formation of oxide pegs [40, 44, 46]. Oxide pegs are finger-shaped oxides growing from the metal-oxide interface into the alloy. These finger-shaped oxides mechanically clamp oxide and alloy together. Second, Y can provide nucleation sites. Nucleation sites are yttrium oxide nano-particles where diffusion of oxygen is several orders of magnitude faster as compared to Cr_2O_3. Thus, the nucleation sites can provide a short cut to free Cr ions and thus promote selective oxidation of Cr which yields a faster formation of a closed chromia layer [40, 47, 48]. A closed chromia layer suppresses the formation of other oxides. However, none of these effects were investigated for W-based alloys.

1.3 On oxidation mechanisms

Ellingham-Richardson diagrams show the Gibbs free energy change ΔG for a reaction in dependence of the temperature. Here, the reactants are a metal and oxygen. ΔG is given per $1\,mol$ O_2 and can be expressed as

$$\Delta G = \Delta H - T\,\Delta S \tag{1.3}$$

where T is the temperature, ΔH is the enthalpy change, and ΔS is the entropy change. Using ΔG the equilibrium oxygen pressure can be calculated by

$$p_{O_2} = \exp\frac{\Delta G}{RT} \times 1\,bar \tag{1.4}$$

where R is the gas constant and T the temperature [40]. Fig. 1.3 shows the elements of relevance for this work.

The more negative ΔG the less likely an element is found in its elemental form. For example, if WO_3 and Y are mixed and brought into equilibrium by heating in inert atmosphere, the WO_3 is reduced and yttrium oxides form as the ΔG for the reaction of Y and O_2 to Y_2O_3 is much more negative than ΔG for the reaction of W and O_2 to WO_3 (see Fig. 1.3).

Generally, oxidation refers to the reaction between two chemical elements in which electrons are transfered from one element to the other. The reaction of a metal and oxygen from the atmosphere to an oxide is the oxidation process relevant for the work in this thesis. In this case, the mass of the material increases by the mass of oxygen which is added to the material. Thus, the oxidation rate can be quantified by measuring the mass change of the sample as a function of time at a specified temperature and atmosphere.
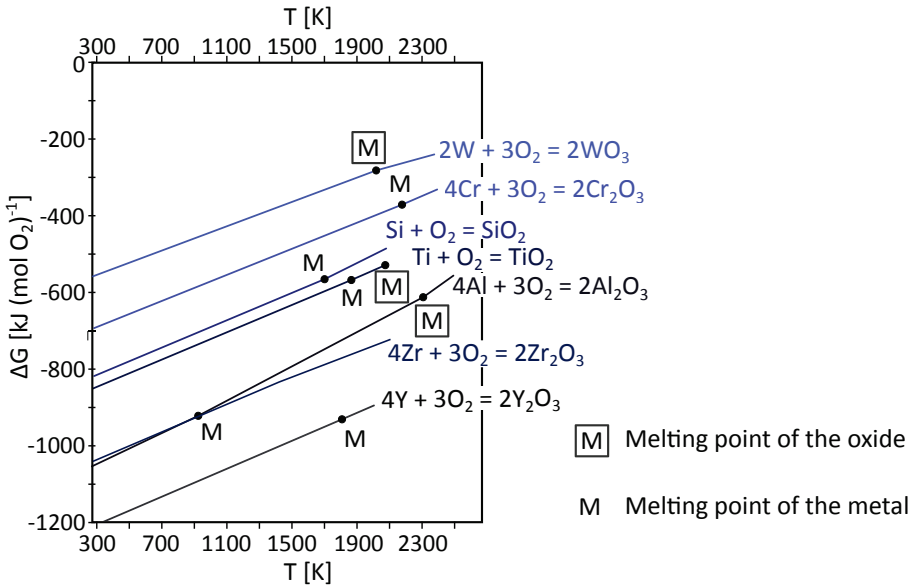

Figure 1.3: Ellingham-Richardson diagrams showing the Gibbs free energy of oxidation reactions as a function of the temperature for different metals. Data taken from [49, 50, 51].

15

The Gibbs free energy is important for understanding which metal in an alloy oxidizes first. However, the total mass gain due to oxidation is determined by the oxidation kinetics. Typically, oxidation starts at the interface between the oxygen containing gas and the metal. Typically, an oxide layer forms on the surface of the metal. This can change the oxidation kinetics due to limited access of the oxygen to the metal. Either, there is open porosity in the oxide layer allowing further oxidation, or diffusion of oxygen ions or metal ions through the oxide is required. Therefore, different mass gain characteristics are found depending on the experimental conditions - in particular on material and temperature. The most common mass gain characteristics are explained in the following [40]:

- Logarithmic oxidation is an empirical law often found for metals at temperatures below $800\,\mathrm{K}$. The oxidation rate decreases with time as more and more oxide protects the metal on the surface.

- Catastrophic oxidation refers to mass loss due to oxidation. Mass loss can be caused due to the formation of liquid or volatile oxides. The mass gain due to incorporation of O and mass loss compete. Mass loss can also be caused by delamination of the oxide layer.

- Linear oxidation indicates that O has continuously access to the metal, independent of the oxidation time and the amount of oxides already formed.

- Parabolic oxidation means that the mass gain decreases with time due to the formation of a protective oxide layer. The rate is controlled by diffusion of metal and oxygen ions through the protective oxide layer. The thicker the oxide layer, the more effective is the protective function.

    The parabolic rate law can be derived as follows: the flux of ions J through the oxide layer with a thickness s is proportional to the change of oxide layer thickness with respect to time ds/dt and proportional to the concentration gradient ΔC of ions. Here, "ions" refers to the faster diffusing ions, depending on the material either O ions or metallic ions. These assumptions yield

$$\frac{ds}{dt} \propto J = -D\frac{\Delta C}{s} \tag{1.5}$$

$$\Rightarrow \int s\,ds = -D\,\Delta C \int dt \tag{1.6}$$

$$\Rightarrow s^2 = -2\,D\,\Delta C\,t + c \tag{1.7}$$

where D is the diffusion constant, t is the time, and c is an integration constant. Using the boundary condition that there is no oxide layer when oxidation starts $s(t = 0) = 0$ yields $c = 0$. The oxide layer thickness is proportional the mass increase Δm normalized to the surface area A and the parabolic oxidation rate follows:

$$\frac{\Delta m}{A} = \sqrt{k_p \times t} \tag{1.8}$$

where Δm is the mass change, A the surface area of the sample, t the time, and k_p the parabolic oxidation constant.

Ideally a material with good oxidation resistance should form a protective oxide layer and follow the parabolic oxidation rate [40]. The oxide of a non-ideal material may crack,

locally providing immediate access to the metal and yielding to faster oxidation. Further, different oxides can form. Different oxides have different diffusion and oxidation kinetics, some oxides can even be volatile. Therefore, full understanding of the oxidation process requires an understanding of all contributions to the total mass gain [40, 44].

1.4 Open questions and outline of the thesis

Research in recent years has brought significant progress in the development of smart alloys, as explained in section 1.2. However, more work and a deeper understanding of the interaction processes between the elements W, Cr, Y, O, and H is required before employing them as first wall armor material in future fusion power plants. This thesis contributes towards that goal by addressing the following questions:

- Which mechanisms are relevant for the transition from thin films to bulk samples? Previous studies used thin films with a thickness $< 10\,\mu m$ [30, 29]. Thin films are deposited by magentron sputtering which is a fast and reliable way to obtain multiple samples. Upscaling of the samples is required for a fusion power plant. Therefore, a detailed understanding on how the material oxidation resistance is influenced is required. The peculiarities of thin films are explained and the details of compacting bulk samples are discussed. An understanding on how and why different sintering parameters influence the microstructure of a sample is developed.

- Which properties are important for a good oxidation resistance of smart alloys? The production of bulk samples has various free parameters - the sintering options, the surface preparation, and the atomic composition. All these parameters must be optimized and understood in order to study the mechanisms of oxidation resistance in detail.

- How much material sublimates under DEMO relevant conditions? Smart alloys should suppress sublimation of radioactive tungsten in case of a LOCA. In order to assess the success it is crucial to measure the absolute sublimation rate. A new setup is developed and calibrated in this thesis to measure the sublimation.

- What are the contributions to the mass change of the sample during oxidation and how to quantify them? Mass gain and sublimation of the samples are measured in separate experiments. The microstructure before and after oxidation is analyzed using electron microscopy after different oxidation times. This allows an understanding of the oxidation dynamics and which oxides form under which conditions.

- How do the mechanisms of oxidation and sublimation change as a function of temperature and atmosphere? Neither the exact temperature nor the specific atmospheric conditions in the power plant after a LOCA are well known. Therefore, it is crucial to understand the influence of different conditions. It is discussed how the presence of water influences the chemical reactions during oxidation and how temperature alters the oxidation process.

- Which diffusion processes occur in the sample during oxidation? The oxidation resistance requires a protective chromium oxide layer which requires the diffusion of Cr and O. An understanding on which elements are diffusing is obtained using ^{18}O isotopes as tracer. Further, the phase formation and how it changes the diffusion and oxidation resistance is studied in a dedicated experiment where the oxidation behavior of samples containing a Cr rich phase is compared to the oxidation resistance of homogeneous samples.

- Which mechanisms cause increased oxidation resistance if Y is added to the material? In this thesis the effect of Y in W-Cr alloys is studied for the first time in detail. Crucial experiments for making a hypothesis are to spatially locate the Y in the alloy using atom probe tomography and scanning transmission electron microscopy.

- Are there other elements with similar effects as Y? Such studies contribute to the understanding of the role of Y in the oxidation process and may yield to further improvement by finding additional alloying elements which enhance the oxidation resistance. The effects of Zr on the oxidation resistance are investigated in this thesis.

- Which elements attract each other? How stable is the microstructure and what is the role of the different alloying elements? In DEMO the material is exposed to elevated temperatures for years. Thus, an understanding of these mechanisms is crucial to assess the usability of the material. Results on the interaction of ab-initio calculations are shown and compared to experimental results. Differences and similarities are outlined, possible improvements of the calculations are discussed.

The present first chapter introduces fusion and its material requirements combined with an overview of previous work on tungsten alloys and an introduction to oxidation. The second chapter introduces the experimental methods used within this thesis. The third chapter focuses on the oxidation and sublimation of pure tungsten, the main element contained in smart alloys. The forth chapter investigates the volatilization of pure chromium oxide, which is the protecting oxide of smart alloys. The fifth chapter shows oxidation studies on W-Cr-Y thin films, the films are characterized, the oxidation kinetics are discussed, and the importance of Y is demonstrated. The sixth chapter addresses a detailed analysis of the compacting of W-Cr-Y bulk samples by Field-Assisted Sintering Technology, an important technological route for sintering smart alloys. The seventh chapter investigates the influence of different production parameters on the oxidation resistance of smart alloys. The chapter concludes with a recommendation for production. The eight chapter presents long-term studies of optimized bulk alloys. Oxidation resistance and sublimation rates are measured and discussed in dry and humid air. The ninth chapter presents dedicated experiments generating an enhanced understanding of the mechanisms yielding to the oxidation resistance of smart alloys. The tenth chapter shows first modeling efforts. Knowledge from the field of high entropy alloys contributes to the understanding of smart alloys. In the eleventh chapter zirconium is investigated as an alternative alloying element to yttrium. The twelfth and last chapter presents conclusions on the work in this thesis and an outlook for future developments of smart alloys.

Chapter 2

Experimental methods

2.1 Magnetron deposition

A magnetron is used to deposit films on a substrate. Magnetron sputtering is a fast and reliable way to make multiple samples for testing and understanding the performance of a material. A multi-electrode magnetron sputter-device manufactured by PREVAC, 44362 Rogow, Poland, is used in this work. The produced films have a thickness below 10 µm and can contain up to four different elements as four different electrodes with an individual power supply are available. The purity of all used targets with a diameter of 7.6 cm is better than 99.9 %.

The schematic working principle is illustrated in the photograph shown in Fig. 2.1. In a typical deposition process the pressure in the magnetron chamber is reduced below 1×10^{-5} mbar. Then argon (Ar) is introduced into the chamber causing the pressure to increase to 6×10^{-3} mbar. At the same time a negative voltage is applied to the metal targets. Further, there is a magnetic field near the target. Ar ions are accelerated towards the target and electrons spiral along the magnetic flux lines ionizing Ar atoms. A stable plasma is generated and the the accelerated Ar ions continuously sputter material of the target. This material deposits onto the substrates placed on a grounded, rotating table below the electrodes with the targets. Typically the voltage applied to each electrode is in the range of 100 V to 500 V corresponding to $2\,\mathrm{V\,cm^{-2}}$ to $11\,\mathrm{V\,cm^{-2}}$, a higher voltage
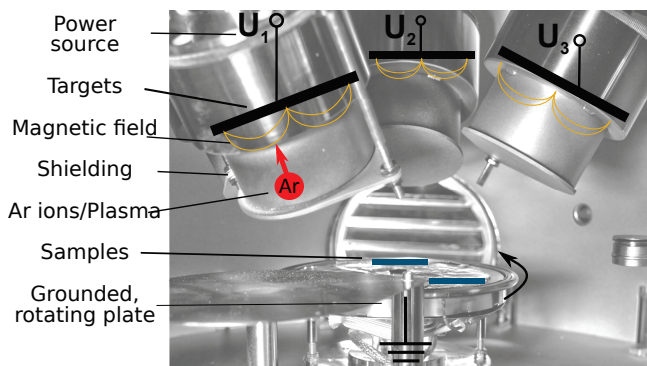

Figure 2.1: Photograph of the multi-electrode magnetron sputtering device including a schematic illustration of the working principle.

yields a higher sputtering rate and thus a higher concentration of that target element in the deposited sample.

The power to the target is supplied either by a direct-current (DC) power supply or an radio-frequency (RF) power supply. Using a DC power supply causes positive charge to build up on the surface of the target. An electrically conductive sample allows the charge to be compensated. However, in case of an insulating target the charge repels the incoming ions and sputter deposition is not possible. Using a RF power supply allows to compensate the charge. For metallic targets the sputtering efficiency drops using a RF instead of a DC power supply as less ions are attracted. Therefore, the main elements W and Cr of smart alloys are sputtered using a DC power supply while the active element Y is sputtered using a RF power supply. This allows accurate control of the required low concentrations of around $1 \, \text{wt.} \%$.

2.2 Powder mechanical alloying

Powder mechanical alloying is the first step for the production of bulk samples. The planetary ball mill PM400 manufactured by Retsch, 42781 Haan, Germany, is used in this work. In general the mill can be used for pulverizing, mixing, homogenizing, colloidal milling, and mechanical alloying.

A grinding jar is filled with milling balls and the sample powders. The jar is then placed eccentrically on the circular plate of the planetary mill. The circular plate is rotated and the jars themselves are rotated in the opposite direction. As a result of the rotation the balls are subjected to Coriolis forces [52]. The upper boundary for the kinetic energy E_{kin} of an individual ball is given by its mass m and the velocity v of the jar. In this work $m = 89 \, \text{g}$ and $v = 5 \, \text{m} \, \text{s}^{-1}$ are used as recommended by [53]. The calculation yields

$$E_{\text{kin}} = \frac{1}{2} m v^2 = 0.1 \, \text{J} \approx 10^{18} \, \text{eV}. \tag{2.1}$$

In comparison, the cohesive energy of a W atom in the crystal lattice is $8.9 \, \text{eV}$ [54]. The kinetic energy from the balls is transferred to the powder particles resulting in size reduction of the initial particles, agglomeration of fine particles, and mechanical alloying.

The specific milling parameters are adapted according to the recommendations of [53, 55]: the grinding jars are filled with milling balls and different powders in Ar atmosphere to avoid oxidation during mechanical alloying. The jar with a volume of $250 \, \text{ml}$ and balls with a diameter of $10 \, \text{mm}$ are made from tungsten carbide (WC) to avoid contamination of the powder with other metals. The powder particle diameter is below $75 \, \mu\text{m}$, the ball-to-powder-ratio is 5:1, and $110 \, \text{g}$ of powder are filled into a jar. The circular plate with the jars is rotated with $250 \, \text{rpm}$ (rotations per minute). The jars themselves are rotated in the opposite direction at $500 \, \text{rpm}$, as illustrated in Fig. 2.2 a. The rotation is performed for $60 \, \text{h}$.

2.3 Field assisted sintering technology (FAST)

Field assisted sintering technology (FAST) is used to compact the mechanically alloyed powder. Sintering is achieved in a short time using heat and pressure. Bulk samples of a DEMO-relevant size can be sintered. The method is also known as 'Spark plasma sintering' - however, a spark or a plasma could not yet be detected during the sintering

process [56]. The device FCT HPD5 manufactured by FCT Systeme GmbH, 96528 Effelder-Rauenstein, Germany is used.

The basic principle of FAST is ohmic heating and pressure to achieve sintering, as illustrated in Fig. 2.2 b. An electric current flows through the graphite die and the powder. Typically, the electrical resistance of the powder is high as compared to the sintered sample [56]. Therefore, the current through the sample increases with progressing in the sintering process. The current through the sample is inhomogeneous and a network of current paths forms depending on the initial packing structure. Locations with a higher current density can locally reach temperatures above the average temperature of the sample. Depending on the material and on the sintering parameters these temperature inhomogeneities are visible in the resulting microstructure of the sample [56]. Further, the electrical resistance at the contacts between the particles is higher as compared to inside the particles. Thus, more heat is generated at the contacts and the temperature at the contacts is higher [57].

The full sintering process takes only a few minutes. Therefore, the time is not sufficient for the system to reach thermodynamic equilibrium - grain growth and phase formation are reduced as compared to other sintering methods such as Hot Isostatic Pressing (HIP) [57]. More details on FAST are found in [56].

The FAST process follows the following steps: first, a graphite die with an inner diameter of 2 cm is prepared by cladding it with graphite foil. Second, the mechanically alloyed powder is poured into that die. Good electrical, thermal, and mechanical contact between the die and the powder must be ensured. Third, the die is placed in the FAST device and the chamber is pumped to around 1 mbar. Fourth, uniaxial pressure is applied onto the powder. Typically the pressure is chosen to be 50 MPa, alloys which are prepared using a different pressure are marked explicitly. Fifth, a current is applied to heat the sample at a rate of $100\,\mathrm{K\,min^{-1}}$ to $300\,\mathrm{K\,min^{-1}}$. This requires a heating power of 1 kW to 10 kW, the heating power depends on the heating rate and the temperature - the device dynamically adjusts the input power on the temperature measured by a pyrometer. Sixth, the target temperature of 1700 K to 1850 K is reached and held for a certain time, this time will be specified for each experiment individually. Seventh, the pressure is released and the heating is stopped, the sample cools down at around $300\,\mathrm{K\,min^{-1}}$. The chosen target temperature, holding time, and heating rate are given specifically for each sample.
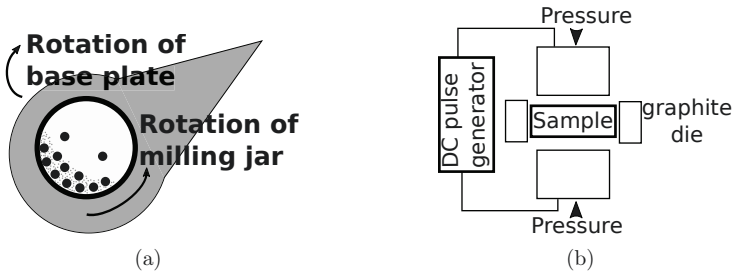

Figure 2.2: (**a**) Schematic top view on the planetary ball mill showing the milling balls and the powder inside a WC jar and the directions of rotation. (**b**) Schematic of the Field Assisted Sintering Technology (FAST).

2.4 Cutting and grinding

Mechanical cutting and grinding are the last steps after sintering to obtain a bulk sample for investigations. All grinding steps are performed on a grinder with a planar rotating disc and silicon carbide (SiC) abrasive paper on the disc.

After sintering around 0.5 mm of material is removed from all sides of the sintered ingot. The removal ensures that the carbon contaminated material is removed and that a homogeneous sample remains [53]. The removal is achieved by pressing the sample with up to 0.3 MPa onto a SiC paper while rotating with 150 rpm. A constant flow of water is maintained for cooling. The SiC paper has a grid size of 80 corresponding to SiC particles with a size of 188 μm. The material removal of the sample is checked in intervals of 10 min.

Afterwards the ingot is cut into nine cubes with a size of about 4 mm each. In order to allow mechanical cutting without cracking of the samples, the ingot is fixed into a drilled aluminum block. The cut is performed using a boron-carbid-bound diamond cutting wheel rotating at 3200 rpm while cooling with water.

The resulting samples are manually ground using a planar grinder. In the following the optimized grinding routine is described. It will be specifically remarked, if any sample is ground differently; the influence of the grinding on the oxidation resistance is described in section 7.2. In the optimized routine, three samples are glued using wax to a metallic disc ensuring a full contact to the abrasive paper during grinding. The three samples are pressed onto the rotating disc with a force of ∼0.02 kN in total, thus there is a pressure of ∼0.4 MPa on each sample. The rotation speed is 50 rotations per minute. A reproducible surface finish is achieved by successive grinding with finer SiC paper: P400, P800, P1000, and twice P1200 grid size is used for 2 min each. The P1200 grid size has particles of 8 μm. The sample is cleaned at room temperature for 15 min in an ultrasonic bath with first acetone (C_3H_6O) and then isopropanol (C_3H_8O) before further analysis.

In some cases it is interesting to look at the surface microstructure using microscopy techniques. In that case the sample needs to be polished. The aforementioned grinding process is continued on the planar grinder by polishing with SiC paper of the grid size P2500 and P4000. Afterwards the SiC paper is exchanged to a cloth on which a diamond paste with a particle diameter of 1 μm is applied. In a final polishing step an Active Oxide Polishing Suspension (OPS) with 0.04 μm SiO_2 particles is used for 10 min to 20 min.

2.5 Carbon determination

The carbon (C) content of a sample is quantified using the carbon determinator CS600 manufactured by LECO corporation, 49085 St. Joseph, USA. In a first step a sample of around 0.1 g is combusted in a stream of purified oxygen. During this process all the carbon in the sample is oxidized to carbon dioxide (CO_2) and carbon monoxide (CO). In a second step the gases are swept though a dust filter, a drying reagent, and a heated catalyst converting CO to CO_2. In a third step the CO_2 is measured in an infrared absorption cell. CO_2 absorbs infrared light at a wavelength of 2.7 μm, 4.3 μm, and 15 μm. The detectors measure the changes in intensity at this wavelength as the gas passes through the infrared absorption cell. The detection limit is at around 10 ppm. Calibration is performed by measuring the C content of a reference material provided by LECO.

2.6 Oxygen and nitrogen determination

The oxygen (O) and nitrogen (N) content of a bulk sample is quantified using the Nitogen/Oxygen determinator TCH600 manufactured by LECO corporation, 49085 St. Joseph, USA. The detection limit of O and N is around $0.5\,\mu g\,g^{-1}$.

A weighted sample is placed in a graphite crucible and heated by an electric current in a flowing helium gas stream. O and N are released from the material. The O reacts with the carbon (C) from the crucible to CO. The CO is quantified by infrared absorption. Then, the gas passes through heated copper oxide which converts any CO and hydrogen to water which is removed by a Lecosorb/Anhydrone trap. Following this, the thermal conductivity is measured allowing to determine the N_2 content. Calibration is performed by measuring the O and N content of a reference material provided by LECO.

2.7 Inductively coupled plasma optical emission spectrometry (ICP-OES)

The elemental composition of samples can be determined using Inductively Coupled Plasma Optical Emission Spectroscopy (ICP-OES). The devices iCAP7600 and iCAP6500 ICP-OES analyzer manufactured by Thermo Fisher Scientific (Waltham, MA USA 02451) are used in this work. In preparation for the measurement the sample is dissolved: the sample is placed in $1\,ml$ to $3\,ml$ $HClO_4$ and $1\,ml$ to $3\,ml$ H_2PO_4. For both acids the same amount is used, the exact amount depends on the size of the sample. The sample is fully dissolved using Berghof pressure digestion in a quartz beaker at a temperature of $520\,K$ to $580\,K$ for $3\,days$. The resulting solution is diluted with water to a volume of $100\,ml$. The diluted solution is sprayed into a plasma using a nebulizer. The plasma excites the sprayed atoms. When returning to the ground state, the atoms emit a characteristic radiation. The detection of the emitted radiation allows quantitative determination of the contained elements. The detection limit is around $1\,\mu g\,g^{-1}$. Calibration is performed using standardized reference solutions.

2.8 Weighting

The mass and the density of the samples is measured using the analytical balance MSA225S from Sartorius, 37079 Göttingen, Germany. A mass of up to $220\,g$ can be measured with a precision of $10\,\mu g$. The mass of the measured sample generates a torque via a lever due to its weight. This torque is compensated by an electric coil in a constant magnetic field. The mass of the sample is determined based on the current required in the coil.

The density is measured using the same device, doing two measurements. In a first measurement the weight of the sample in air is measured. In a second measurement the buoyancy force of the sample immersed in ethanol is determined. Based on Archimedes' principle this is directly proportional to the volume of the displaced fluid. Volume and density can be calculated from the results of the two measurements.

2.9 Profilometry

The surface roughness of the samples is measured using the profilometer Dektak 6M from Bruker. A diamond-tipped stylus with a diameter of $2\,\mu m$ is electromechanically moved across the sample. The surface profile of the sample causes vertical movement of the tip. By coupling the tip to a linear variable differential transformer the vertical movement generates an electrical signal which can be converted in a digital format. A line scan is performed and the surface roughness r_a is calculated using the equation

$$r_a = \frac{1}{n} \sum_{i=1}^{n} |x_i| \tag{2.2}$$

where n is the number of data points and x_i the distance of data point i from the surface plane. The surface plane is defined as the average measured height over a length of $1\,mm$. The maximum scan length is $3\,cm$, the vertical resolution is $\sim 10\,nm$.

2.10 X-ray diffraction (XRD)

The crystal lattice structure of the samples is measured using the X-ray diffraction (XRD) device D8 Discover from Bruker, AXS GmbH, 76187 Karsruhe, Germany. The source is a copper X-ray tube emitting at a wavelength of $0.154\,18\,nm$. The detector is the one-dimensional silicon strip detector Lynxeye XE. X-ray source and detector are continuously rotated during the measurement in order to measure the intensity in dependence of the diffraction angle 2θ from $20°$ to $100°$.

The incident X-rays are reflected at the sample. Constructive interference occurs when Bragg's law applies:

$$n\lambda = 2d_{hkl} \sin\theta_i \tag{2.3}$$

where n is a natural number, d_{hkl} is the lattice spacing of the set of lattice planes (h,k,l), and θ_i the diffraction angle. The intensity of the reflected X-rays is depicted as a function of the diffraction angle θ_i in a diffractogram. Each maximum in the diffractrogram belongs to a specific set of lattice planes. A crystal structure has multiple sets of lattice planes which give rise to different maxima. A material containing different phases results in a diffractogram with maxima for each phase. The position of the peak relates to the lattice constant, the width of the peaks relates to the variation in lattice constant, and the relative intensities relate to the crystal orientation and the amount of a certain phase. More details are provided in [58] and when analyzing a specific diffractogram.

2.11 Secondary ion mass spectroscopy (SIMS)

Changes in the elemental composition as a function of depth in the samples are measured by Secondary Ion Mass Spectroscopy (SIMS). The machine ToF-SIMS IV manufactured by ION-TOF GmbH, 48149 Münster, Germany is used in this work.

The machine is operated in dual beam mode: one beam sputters a crater, the other beam progressively analyzes the crater bottom. For sputtering typically a ceasium beam with an energy of $2\,keV$ and a current around $0.2\,mA$ is used to make a crater of $0.3\,mm \times 0.3\,mm$. The sputter time is recorded and the crater depth is measured using the Dektak 6M (see section 2.9). On W alloys a sputter-rate of $\sim 3\,\mu m\,h^{-1}$ is measured

using the aforementioned parameters. An area of around $0.1\,\text{mm} \times 0.1\,\text{mm}$ is bombarded with a bismuth beam with an energy of $25\,\text{keV}$ and a current of $1\,\text{nA}$. This bombardment generates secondary particles from the sample. The secondary ions are analyzed in a time-of-flight (ToF) mass spectrometer and the intensity of ions in dependence of their mass is obtained. The mass resolution allows to separate different isotopes of an element. Combined with the depth information this allows to determine changes in the elemental composition of the sample as a function of depth.

The analyzed secondary ions constitute only $0.1\,\%$ to $10\,\%$ of the secondary particles, the ionization rate depends on the element and the surrounding material [59, 60]. Therefore, the determination of absolute concentrations is difficult using SIMS. When an oxygen beam instead of the caesium beam is used for sputtering, electrons are transferred from the metal surface to the oxygen ions resulting in an increased ionization rate of the sputtered metal. The higher ionization rate yields a higher sensitivity for metals. However, the oxygen composition change can not be measured when an oxygen beam is used. Further, it must be considered that surface roughness and porosity in the sample propagates to the bottom of the sputtered crater which is analyzed. This roughness results in an uncertainty in the depth resolution. Therefore, it is important to start with a flat surface and a sample without porosity.

2.12   X-ray photoelectron spectroscopy (XPS)

X-ray photoelectron spectroscopy (XPS) is used to measure the oxygen content in thin films deposited by magnetron sputtering. The used device was set up in collaboration with PREVAC, 44362 Rogow, Poland. In XPS the sample is irradiated with photons at the energy $E_p = 1486.6\,\text{eV}$. The photoelectric effect occurs: electrons in the sample are excited and may leave the electronic core. The binding energy E_b of the emitted photoelectron can be calculated from

$$E_b = E_p - E_{kin} - \Phi_A \tag{2.4}$$

where E_{kin} is the measured kinetic energy of the emitted electrons, and Φ_A is the work function of the analyzer. Conclusions about the chemical composition within the first nanometers are drawn. Before a measurement it is possible to sputter the surface with argon ions. Sputtering allows cleaning of the surface and measurements below the initial surface. The base pressure in the device is $1 \times 10^{-10}\,\text{mbar}$.

2.13   Preparation using a focused ion beam (FIB)

Preparation of samples using a focused ion beam (FIB) is important for the following applications in this thesis:

- To prepare a cross section which is imaged using electron microscopy (see section 2.14).

- To prepare a lamella for analysis using scanning transmission electron microscopy (see section 2.14.3)

- To prepare a tip which is analyzed using atom probe tomography (see section 2.15).

In this work FIB milling is performed mostly in the Crossbeam 540 manufactured by Carl Zeiss, 73447 Oberkochen, Germany. Gallium ions at an energy of $30\,\text{kV}$ are used for milling. The milling rate depends on the material and the ion current - the higher the current the higher the milling rate. The current can be selected in the range of $1\,\text{pA}$ to $100\,\text{nA}$.

Typically the surface is protected with a layer of platinum (Pt) before starting a milling process. The Pt coating is achieved by ion-beam assisted deposition: the precursor methylcyclopentadienyl(trimthyl)platinum(IV) ($C_9H_{16}Pt$) is vaporized and liberated by a gas-injection system near the desired coating region. In parallel the gallium ion beam scans the surface with $300\,\text{pA}$ causing deposition of Pt particles on the surface. The first rough milling process typically starts with $30\,\text{nA}$. The spot size of the ion beam at this current is $4.2\,\mu\text{m}$. A lower current is used for higher precision and cleaning - the spot size of the ion beam at $700\,\text{pA}$ decreases to $1.3\,\mu\text{m}$. A cross section on a sample is usually cleaned with a current down to $700\,\text{pA}$ whereas a thin lamella is exposed to currents down to $10\,\text{pA}$ with a spot size of $0.2\,\mu\text{m}$.

2.14 Microscopy

2.14.1 Scanning electron microscopy (SEM)

The microstructure and surface morphology is imaged using scanning electron microscopy (SEM). The Crossbeam 540 electron microscope manufactured by Carl Zeiss, 73447 Oberkochen, Germany, is used. The device allows the preparation of cross sections and lamellas by FIB (see section 2.13) and image them by SEM and Energy dispersive X-ray spectroscopy (EDX) without breaking the vacuum. The geometry of imaging on a cross section is illustrated in Fig. 2.3 a. The base pressure in the chamber is below $1 \times 10^{-6}\,\text{mbar}$.

For imaging a focused electron beam scans a surface. The electron energy typically is between $1\,\text{keV}$ and $5\,\text{keV}$, the current is around $0.1\,\text{nA}$ to $0.2\,\text{nA}$ for a resolution below $10\,\text{nm}$. Faster imaging at reduced resolution can be performed at up to $300\,\text{nA}$. The incident electrons interact with the material as schematically illustrated in Fig. 2.3 b. Some electrons are backscattered and secondary electrons (SE) are generated. Electrons after material interaction are detected while scanning. The intensity, as a function of the position on the sample is recorded. Different detectors are used in this work:

- the conventional Everhart-Thornley type SE detector [61] is placed next to the pole piece of the incident beam, has a collector bias voltage of $300\,\text{V}$, and detects SE. This detector is particularly sensitive to the surface topography.

- the in-lens SE detector is placed inside the pole piece of the electron microscope and detects SE. Due to its position it is more sensitive to differences in the work function, the electronic configuration in the sample and less sensitive to topography as compared to the conventional SE detector. Consequently, the image shows a stronger elemental contrast. [62].

- a Energy Selective Backscatter (ESB) detector for backscattered electrons is placed inside the pole piece of the microscope behind a repelling grid at a voltage of $1\,\text{kV}$. SE are repelled by this grid as they have a lower energy compared to the backscattered electrons. Backscattered electrons originate from a larger depth in

the sample than SE electrons as illustrated in Fig. 2.3 a. Therefore, an image based on backscattered electrons is particularly sensitive on elemental contrast whereas topography is hardly visible.
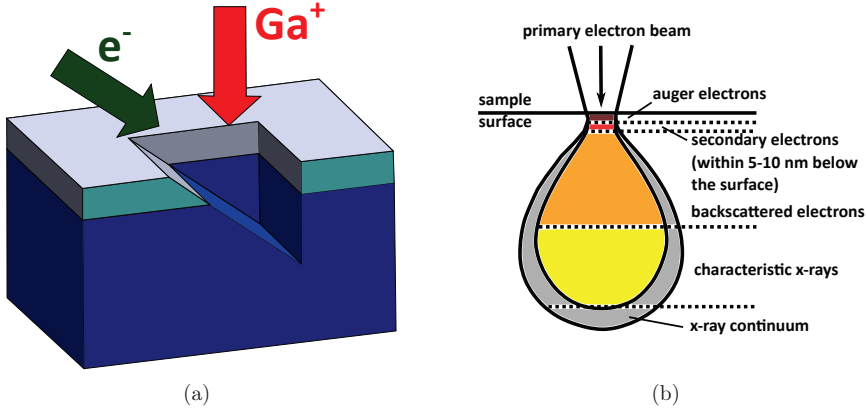

Figure 2.3: (**a**) Illustration of the geometry when imaging with secondary electrons on a cross section prepared by focused ion beam milling. (**b**) Schematic of the electron-matter interaction.

2.14.2 Energy dispersive X-ray (EDX) spectroscopy

Energy Dispersive X-ray spectroscopy allows an identification of chemical elements on a surface with a spatial resolution in the sub-µm range. The EDX detector is integrated in the Crossbeam 540 electron microscope mentioned in sections 2.13 and 2.14.1. There is a monochromatic incident electron beam with an energy between 1 keV and 30 keV. The electrons excite atoms. Once the excited atoms relax, they emit their characteristic X-rays. The X-rays are detected and the intensity as a function of energy is measured. The information on the elemental composition at the position where the electron beam hits the sample is obtained. It is possible to scan the surface while detecting the X-rays showing the spatial distribution of elements on the sample surface.

The higher the electron energy the higher energy levels of the atoms can be excited. Excitation to high energy levels is important in order to have unambiguous peaks for different elements. However, the higher the electron energy the larger the penetration volume and the poorer the spatial information on the location of the excited atoms. In a first approximation, the measurement is based on the X-rays from a hemispheric volume around the penetration spot of the electron beam: the depth of the volume is $x[\text{µm}] = 0.1E_0^{1.5} \times \rho^{-1}$ and the width is $y[\text{µm}] = 0.077E_0^{1.5} \times \rho^{-1}$ where E_0 is the electron energy in keV and ρ the material density in g cm^{-3} [63].

2.14.3 Scanning transmission electron microscopy (STEM)

Imaging on a nano-scale is achieved by Scanning Transmission Electron Microscopy (STEM) using the FEI Titan 80-300 STEM at the Ernst Ruska-Centre [64]. A resolution down to 50 pm can be reached. STEM requires the preparation of a lamella before imaging. A lamella with the size of about 10 µm × 10 µm and a thickness below 100 nm is cut using

FIB (see section 2.13). This lamella is scanned in the microscope with a monochromatic electron beam at an energy of 200 keV. The electrons interact with the material when passing the lamella. An annular dark-filed detector and an electron spectrometer detect the scattered, transmitted electrons to reconstruct an image. Further, the EDX spectrum (see section 2.14.2) can be analyzed for elemental assignment.

2.15   Atom probe tomography (APT)

Atom probe tomography (APT) provides three dimensional information on the distribution of individual atoms in a sample. The device LEAP 4000X HR manufactured by Cameca Scientific Instruments (Madison, WI, 53711, USA) is used. The spatial resolution is ≤ 1 nm. The mass resolution $m/\Delta m$ is below 1000, where m is a mass and Δm a mass difference. The elemental sensitivity is down to 10 ppm.

APT requires the preparation of a needle-shaped sample by FIB. The diameter of the needle is several tens of nm, the length is 100 nm to 200 nm. The needle is placed at a temperature of 50 K and a pressure of $\sim 10^{-10}$ mbar in an electric field of 10 V nm^{-1} to 20 V nm^{-1} causing the atoms at the top of the needle to be at the threshold to field-activated ionization. Laser flashes at a frequency of 200 kHz ionize and vaporize the atoms at the surface successively. The ion is accelerated to a position-sensitive detector for spatial resolution. The detector efficiency achieved in experiments presented in this work is 36 %. The charge-to-mass ratio, in other words the element, is resolved by the time of flight of the ion. More details on the development of APT are found in [65].

2.16   Thermogravimetric analysis (TGA)

The weight change of a sample in a controlled atmosphere at a controlled temperature is measured in a thermogravimetric analyzer (TGA). A measurement of the weight change allows quantification of the oxidation resistance and of the sublimation. Oxidation causes mass increase of a sample as oxygen is incorporated into the material. Sublimation causes mass loss of a sample as material leaves the sample.

The device "TAG 16/18" manufactured by Setaram, 69300 Caluire, France is used, characterized and partially improved. The operation temperature can be chosen in the range from 300 K to 2000 K. A graphite resistor is used for heating. The device can be evacuated down to 3×10^{-3} mbar and filled with a variety of gases to ambient pressure: argon (Ar), nitrogen (N$_2$), helium (He), oxygen (O$_2$), and isotope pure oxygen-18 (^{18}O$_2$) are used in this work. One gas can be introduced with a relative humidity level of 0 % to 100 % at a temperature of 340 K. The maximum working volume is a cylinder with a diameter of 14 mm and a height of 20 mm. The maximum sample weight is 32 g, a weight change up to 400 mg can be measured with a precision of 0.1 µg. Stable operation for a month or more is possible, a drift as low as 0.1 µg h^{-1} is possible under isothermal conditions. The temperature variation within the homogeneous zone can be up to 4 K as a reference measurement with an external thermocouple shows, see Fig. 2.4 a. The homogeneous zone, in which the sample must be placed, is marked in green. Cooler regions are marked blue in Fig. 2.4 a.

Inside the furnace the samples lie in an inert quartz glass or inert alumina holder allowing full exposure to the surrounding gas flow. The laminar gas flow is 10 ml min^{-1} in a tube with a diameter of 2.2 cm. In the case of a humid gas, the flow is increased to

$20 \, \text{ml} \, \text{min}^{-1}$ allowing more accurate control of the humidity level. The holders hang on a platinum wire connected to the micro-balance located approximately $0.4 \, \text{m}$ above the sample, protected from perturbations due to the heating. The weight change is measured by determining the electrical current through an electromagnetic coil required to keep a flap in position. The position of the flap is controlled using a laser beam and photo-resistors.

The TGA has a symmetrical, dual furnace design. One side of the dual furnace contains the sample, which may change its mass during the experiment. The other side of the furnace contains an inert product. The inert product has the same volume as the sample and compensates for buoyancy effects [66]. The buoyancy effects are critical during temperature ramps, while isothermal experiments are less sensitive - experiments show that a deviation of $20\,\%$ in volume is acceptable. The standard setup is illustrated in Fig. 2.4 b: the mass change of the sample in an inert holder is measured. A customized setup is developed in the framework of this thesis to measure sublimation as illustrated in Fig. 2.4 c: an inert catcher is connected to the balance. The sample is hung inside the catcher, there is no direct mechanical contact between the catcher and the sample, the sample is not connected to the balance. Materials sublimating from the sample can deposit onto the catcher whose mass change is recorded. As only a fraction of the sublimated material deposits onto the catcher, this measurement requires a calibration for a specific temperature, material, and gas flow. The calibration measurements will be shown before each sublimation measurement.

A typical oxidation experiment uses the following routine:

1. The furnace is closed and evacuated at room temperature. After $45 \, \text{min}$ a pressure around $3 \times 10^{-2} \, \text{mbar}$ is reached.

2. The furnace is flooded with Ar 6.0 (i.e. Ar with a purity of $99.9999\,\%$) to atmospheric pressure.

3. Steps 1 and 2 are repeated up to six times. The temperature during evacuation is increased up to $520 \, \text{K}$ and the pumping time up to $1.5 \, \text{h}$. A pressure as low as $3 \times 10^{-3} \, \text{mbar}$ can be achieved. Each pumping cycle decreases the amount of residual gases in the furnace. Residual oxygen in the furnace during the heating process starts the oxidation process at lower temperatures before reaching the isothermal oxidation zone.

4. The furnace is heated to the target temperature under Ar or N_2 flow. The heating rate is $10 \, \text{K} \, \text{min}^{-1}$ to $20 \, \text{K} \, \text{min}^{-1}$. A heating rate of $10 \, \text{K} \, \text{min}^{-1}$ is recommended for a longer lifetime of the graphite heating elements. The heating rate is gradually decreased starting from $20 \, \text{K}$ below the target temperature. At around $4 \, \text{K}$ below the target temperature the heating rate is reduced to $2 \, \text{K} \, \text{min}^{-1}$ reducing temperature oscillations due to overheating below $1 \, \text{K}$.

5. The furnace is kept isothermally at the desired temperature while the reactive gas (oxygen and/or humidity) is fed into the furnace at a constant flow, as required for the specific experiment.

6. The furnace cools down at a rate of $30 \, \text{K} \, \text{min}^{-1}$ while being flushed with Ar at a flow rate of $100 \, \text{ml} \, \text{min}^{-1}$.

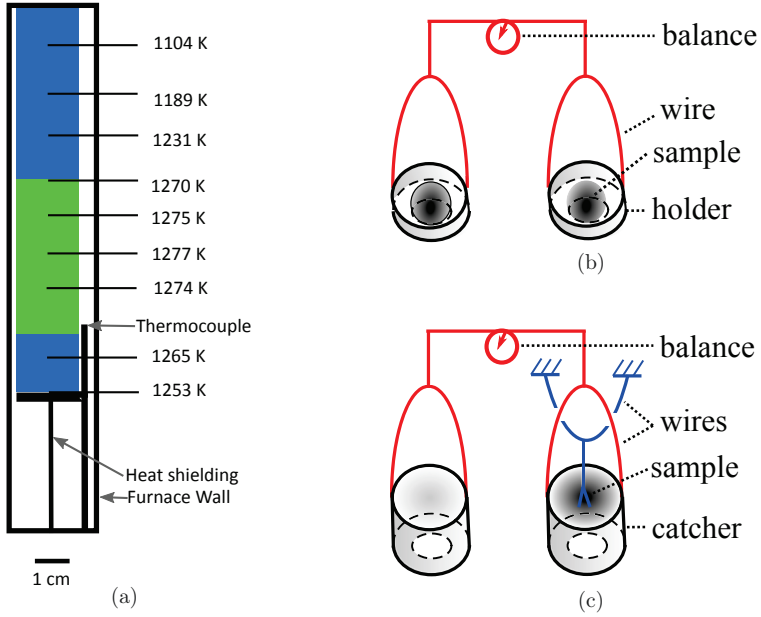7. The furnace is opened and the sample is removed for further analysis.

Figure 2.4: (**a**) Temperature distribution inside the furnace measured using an external thermocouple. (**b**) Schematic of the measurement of the mass change of a sample. The sample lies in the holder and its mass change is recorded. (**c**) Schematic of the measurement of sublimating material depositing onto a catcher. The sample is hung into a catcher. There is no direct contact between the sample and the catcher, only the mass change of the catcher is recorded.

Chapter 3

On oxidation and sublimation of tungsten (W)

3.1 Oxidation

3.1.1 General understanding of the oxidation behavior of W

The oxidation characteristics of pure W are well studied. This chapter summarizes the key characteristics. Further, pure W samples are used to verify that different devices are working correctly and reproduce previous results. When W is exposed to air, the main reactants are O_2 and water. Nitrogen (N_2) does not react with W at a temperature below 1770 K at atmospheric pressure [67]. Carbon dioxide (CO_2) forms W oxides starting from 1470 K [67].

The adsorption of O_2 is the first step of the oxidation process. Molecular adsorption is only found at low temperatures. Starting from room temperature, the molecular adsorption is only a precursor state to the atomic adsorption. Thus, oxidation of W starts at room temperature [68]. WO_3 is the most common tungsten oxide. The volume expansion due to oxidation is given by the Pilling-Bedworth ratio (PBR)

$$\text{PBR} = \frac{V_{\text{oxide}}}{V_{\text{metal}}} = 3.4 \tag{3.1}$$

where V_{oxide} and V_{metal} is the molar volume of the oxide and the metal, respectively. That means the volume of the oxide is 3.4 time larger than the volume of the metal it formed from. This property can cause cracking of the material during oxidation [69, 67].

Various stable tungsten oxides form depending on the temperature and on the oxygen content, as shown in the phase equilibrium diagram in Fig. 3.1. The oxidation mechanisms of a W sample in air works as follows [69, 67]: in the beginning there is a large amount of W on the surface and WO_2 starts to form. A thin oxide layer forms. Oxygen ions diffuse through the oxide scale to the metal-oxide interface. As long as there is a growing WO_2 (or $WO_{2.79}$) scale, the diffusion process is the rate-determining step and the oxidation kinetics follow a parabolic rate law. As there is an infinite O_2 supply, eventually WO_3 forms as an outer oxide as indicated by the phase equilibrium diagram in Fig. 3.1. WO_3 has a PBR of 3.4 as given above. In comparison, the PBR of WO_2 is only 2.1. WO_3 forms, in contrast to WO_2, a physically porous structure and no longer acts as a diffusion barrier for oxygen. Therefore, the oxidation kinetics change to a linear rate once WO_3 is the main oxide.
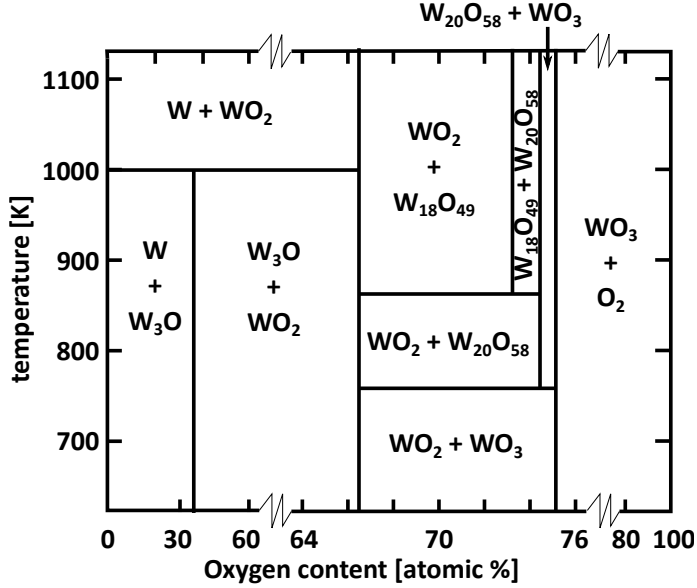
Figure 3.1: Tungsten-oxygen phase equilibria at atmospheric pressure. Diagram adapted from R. Speiser [69].

Experimental measurements confirm this behavior as shown in Fig. 3.2: at 900 K a parabolic oxidation kinetics is observed throughout the measurement period of 2 h. The blue/purple color of the sample indicates that $WO_{2.79}$ oxides are present on the surface. The kinetic at 1273 K is shown in Fig. 3.2 b: a parabolic oxidation rate of $0.4\,\mathrm{mg^2\,cm^{-4}\,s^{-1}}$ is observed for 1 h to 2 h in dry air. After around 2 h the oxidation kinetics changes from parabolic to linear with a rate of $0.4\,\mathrm{mg\,cm^{-2}\,s^{-1}}$, as seen in Fig. 3.2 b. Yellow WO_3 is evident on the surface after oxidation.

In the presence of water (H_2O) there is the additional reaction [68]

$$W + 3\,H_2O \longrightarrow WO_3 + 3\,H_2 \tag{3.2}$$
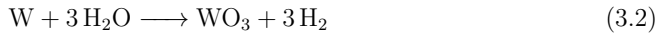
The hydrogen (H_2) partial pressure is assumed to be low as it is an reaction product which the gas flow transports out of the furnace. Reduction of WO_3 must be considered only when the H_2 partial pressure is similar to the the H_2O partial pressure [68]. When water reacts with W, the H_2O molecules are adsorbed at the W surface and dissociate. The O causes oxidation just as in the case of the reaction with O_2 while the H_2 escapes [68]. Therefore, the basic oxidation mechanism of W in the presence of H_2O remains as described above. In humid air the parabolic oxidation rate during the first 2 h of $0.3\,\mathrm{mg^2\,cm^{-4}\,s^{-1}}$ is measured at 1273 K, i.e. the effect on the oxidation kinetics is minor. The effect on sublimation is discussed in section 3.2.

An activation energy E_a needs to be overcome for the oxidation reaction. Therefore, the oxidation rate increases exponentially with temperature. Fig. 3.3 compares linear (Fig. 3.3 a) and parabolic (Fig. 3.3 b) oxidation rates from literature (blue) with the data measured in this work (red stars) in dry air. The data points are based on the fits shown in Fig. 3.2. The literature data is collected from various references: [67, 23, 70, 71]. There is a scatter due to different samples and different experimental setups. However, the conclusion is that the results in this work match with literature data.
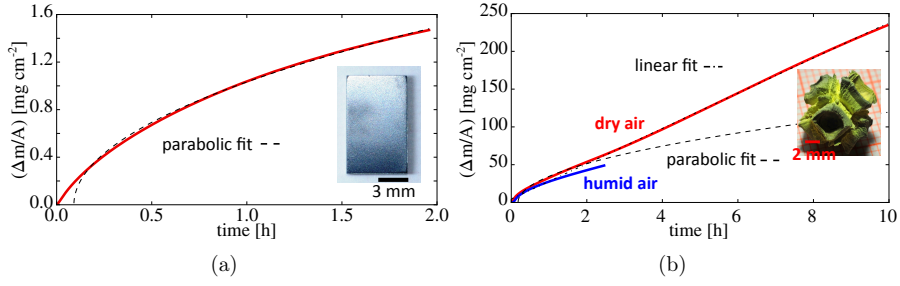
Figure 3.2: (**a**) Mass gain of pure W as a function of time during isothermal oxidation at 900 K in 80 vol. % Ar and 20 vol. % O_2 atmosphere. The dotted line indicates a parabolic fit. The photograph shows the sample after oxidation. (**b**) Mass gain of pure W as a function of time during isothermal oxidation at 1273 K in dry (red) and humid (blue) air. The humidity level of the humid air is 5 vol. % corresponding to 70 % relative humidity at 313 K. A parabolic fit of the first 2 h in dry air and a linear fit for the remaining time in dry air are shown with dashed lines. The photograph shows the sample after 10 h oxidation in dry air.
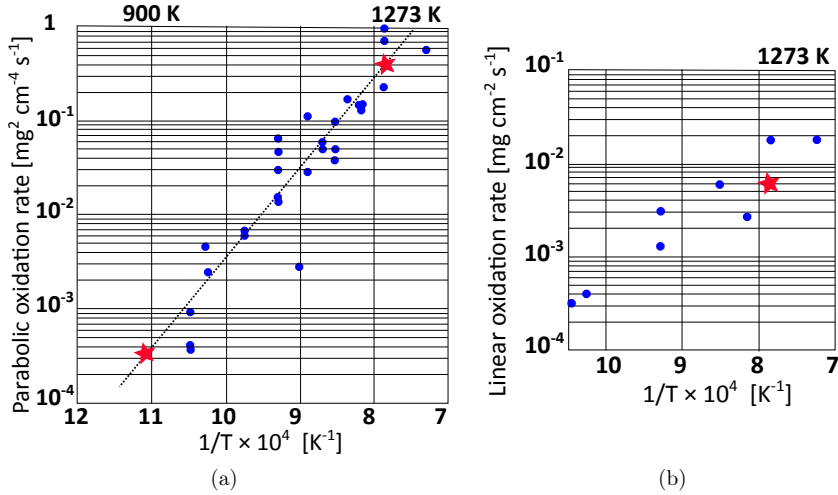
Figure 3.3: Parabolic (**a**) and linear (**b**) oxidation rates of pure W as a function of temperature T. The red stars are measured in this work and connected by a dotted line to guide the eye. The blue points are collected from literature [67, 23, 70, 71].

34

3.1.2 Oxidation of W in different TGAs

For the work on oxidation resistant W alloys, there exists a collaboration with IPP Garching. The TGA in Garching is manufactured by Retsch and operated at a different flow rate and a different geometry. Still, the aim is that results from oxidation experiments in the thermogravimetric analyzers in FZ Jülich and IPP Garching yield comparable results. Calibration with literature data is difficult due to the large scatter in literature data as discussed above, see Fig. 3.3. Therefore, it was decided to conduct experiments with identical samples for comparison.

For that purpose the following conditions are chosen:

- Pure W samples are provided by IPP Garching. Grinding was performed by IPP Garching with a surface finish of P2000 SiC paper.

- Heating is conducted in pure Ar atmosphere.

- Isothermal oxidation at 900 K for 2 h is performed.

- Isothermal oxidation is conducted at ambient pressure in 80 vol. % Ar and 20 vol. % O_2 atmosphere.

Heating and oxidation atmosphere are chosen according to the conditions typical for experiments carried out in both facilities. The temperature of 900 K is chosen for two reasons: first, at this temperature the sublimation of WO_3 is negligible. Thus, the measurement of pure oxidation can be directly compared and potential changes in sublimation due to a different holder geometry are excluded. Second, at this temperature the mass gain is reasonably small. This requires a high precision of the thermogravimetric analyzers. The measurement is repeated three times in both thermogravimetric analyzers.

The results of the oxidation experiments of pure W at 900 K are shown in Fig. 3.4 a. In total there are six oxidation lines shown in Fig. 3.4 a. All of them are almost identical. The only difference is that the three curves measured in Garching start slightly steeper compared to the three curves measured in Jülich. This can be understood looking at the temperature profile shown in Fig. 3.4 b. The thermogravimetric analyzer in Garching heats about 9 K above the target temperature before approaching the target temperature. This behavior is not found in the device in Jülich. The higher temperature in the beginning of the experiment in the device in Garching yields a slightly higher mass gain.

The difference after the inital oxidation phase levels out after longer oxidation times and after 2 h both devices show almost the same mass gain. The mass gain after two hours is given in table 3.1.
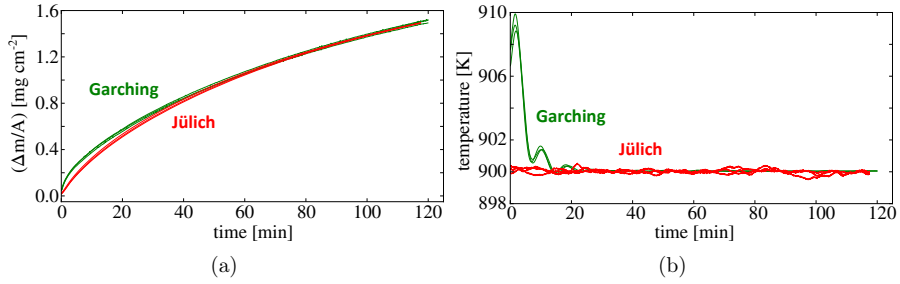
Figure 3.4: (**a**) Mass gain of pure W as a function of time during isothermal oxidation at 900 K in 80 vol. % Ar and 20 vol. % O_2 atmosphere. Three measurements conducted in Garching are plotted in green. Three measurements conducted in Jülich are plotted in red. (**b**) Temperature profile recorded by the thermobalances during the oxidation experiments shown in (a).

Table 3.1: Mass gain after 117.5 min oxidation, as shown in Fig. 3.4 a. $\bar{x}$ is the average value and σ the standard deviation on the average.

Measurement no.	Jülich [mg/cm^2]	Garching [mg/cm^2]
1	1.4936	1.4973
2	1.4937	1.4792
3	1.4911	1.5045
$\bar{x}$	1.493	1.49
σ	0.001	0.01

In conclusion, the two thermogravimetric analyzers in Jülich and Garching produce nearly identical results. The results of different samples oxidized in one or the other device can be compared with each other quantitatively.

3.2 Sublimation of W

Sublimation of tungsten oxide from a fusion power plant is a radiological hazard for the environment, as discussed in section 1.2. The sublimation rate mainly depends on the temperature, the atmosphere and humidity level, the gas flow rate, and the chemical state of the tungsten oxide. At a steam velocity of $48.5\,\mathrm{cm\,s^{-1}}$ at a temperature of $1263\,\mathrm{K}$ a release of $1 \times 10^{-2}\,\mathrm{mg\,cm^{-2}\,s^{-1}}$ is measured [72]. The release is due to aerosol generation, which is optically visible as white steam. The aerosol generation is triggered by the high steam velocity [72]. In this thesis flow velocities below $0.2\,\mathrm{cm\,s^{-1}}$ are investigated where aerosol generation is negligible. Table 3.2 provides an overview on the sublimation rates for different parameters.

Table 3.2: Summary of the sublimation rates of different tungsten oxides in Ar and water vapor in different experimental conditions. Data taken from [18].

Oxide	Temperature [K]	$p_{\mathrm{H_2O}}$ [vol. %]	flow rate [$\mathrm{cm^3 s^{-1}}$]	sublimation [$\mathrm{mg\,cm^{-2}\,s^{-1}}$]
WO_3	1323	33	22.6	7.9×10^{-3}
WO_3	1473	33	21.6	36.8×10^{-3}
WO_3	1473	0	16.1	1.7×10^{-3}
WO_2	1473	33	25.9	8.6×10^{-3}
WO_2	1398	27	13.3	2.4×10^{-3}
WO_2	1398	27	24.2	2.8×10^{-3}

In the present work the focus is on the sublimation rate dependence on temperature and on atmosphere. The temperature is altered in the range of $1050\,\mathrm{K}$ to $1500\,\mathrm{K}$. Three different atmospheres are chosen: $80\,\mathrm{kPa}$ Ar with $20\,\mathrm{kPa}$ O_2, $80\,\mathrm{kPa}$ N_2 with $20\,\mathrm{kPa}$ O_2, and $80\,\mathrm{kPa}$ N_2 with $20\,\mathrm{kPa}$ O_2 and $5\,\mathrm{vol.\,\%}$ water. The humidity level is chosen to resemble the air penetrating the vacuum vessel in case of a LOCA in a tropical climate - $70\,\%$ relative humidity at $313\,\mathrm{K}$.

In order to measure sublimation of tungsten oxide, tungsten must be oxidized first. As long as there is still metallic tungsten in the sample, oxidation and sublimation occur in parallel, both contributing to the mass change. Therefore, it is not possible to directly extract the sublimation rate from the mass change. Fundamentally, there are three options to measure sublimation:

1. The mass change of the sample is measured in an oxygen free environment. This option is not followed further because the yellow WO_3 on the surface changes the color to purple/black after heating for $3\,\mathrm{h}$ in Ar at $1273\,\mathrm{K}$, as shown in Fig 3.5. This color change indicates a reduction of the WO_3 and the sublimation of an oxide not forming in the presence of O_2 is measured.

2. The mass change of a fully oxidized sample is measured in the same atmosphere as during oxidation. This method requires small tungsten samples in order to ensure complete oxidation within a reasonable time. Thin films with a thickness below $5\,\mathrm{\mu m}$ deposited by magnetron sputtering are an ideal candidate.

3. The mass change of a catcher collecting the sublimated material is measured. However, this method requires calibration of the efficiency of the catcher which is carried out using the method described above. Therefore, the catcher is not used to draw conclusions on the sublimation of pure W samples.
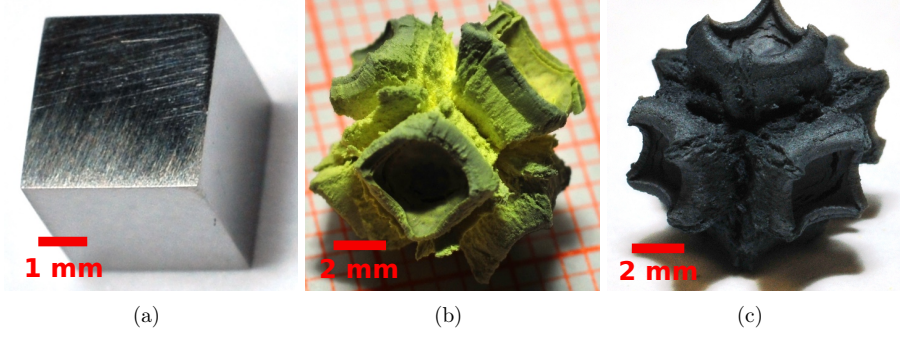
Figure 3.5: Photographs of tungsten/tungsten oxide samples. (**a**) Tungsten sample before oxidation. (**b**) Tungsten sample after 10 h oxidation at 1273 K. (**c**) Tungsten sample after 10 h oxidation at 1273 K followed by annealing in Ar atmosphere for 3 h at 1273 K.

The sublimation rates in dependence of temperature based on the mass loss of fully oxidized thin films are plotted in Fig. 3.6. In Ar with 20 % O_2 an exponential dependence of the sublimation rate s on temperature T is found:

$$s = c_1 \times \exp -\frac{Q}{kT} \tag{3.3}$$

where $c_1 \approx 3.8 \times 10^{10} \, \mathrm{mg \, cm^{-2} \, s^{-1}}$ is a constant, $Q \approx 4.0 \, \mathrm{eV}$ is a constant, and k is the Boltzmann constant.

Based on 7 measurements at 1273 K in Ar with 20 % O_2 an average sublimation rate of $(5.4 \pm 0.9) \times 10^{-6} \, \mathrm{mg \, cm^{-2} \, s^{-1}}$ is found. In comparison, a sublimation rate of $6.7 \times 10^{-6} \, \mathrm{mg \, cm^{-2} \, s^{-1}}$ is measured in N_2 with 20 % O_2 at 1273 K. The standard deviation in $N_2 + O_2$ cannot be calculated as it relies on a single measurement. Thus, the lower boundary for the error bar on the sublimation rate in $N_2 + O_2$ is the one in Ar + O_2. In conclusion the effect of N_2 vs. Ar at 1273 K is small.

The dominating reaction in sublimation of WO_3 in dry air is

$$3 \, WO_3 \, (s) \longrightarrow W_3 O_9 \, (g). \tag{3.4}$$

The heat of sublimation for that reaction is given by $\Delta H = 0.5 \, \mathrm{MJ/mol}$ of $W_3 O_9$ [73].

Humidity has a strong effect on the sublimation rate as seen in in Fig. 3.6: at 1273 K in humid air a sublimation rate of $1.4 \times 10^{-4} \, \mathrm{mg \, cm^{-2} \, s^{-1}}$ is measured, an increase of a factor of 26 as compared to the measurements without humidity. The coefficients from equation 3.3 change to $c_1 \approx 7.0 \times 10^3 \, \mathrm{mg \, cm^{-2} \, s^{-1}}$ and $Q \approx 1.9 \, \mathrm{eV}$. In the presence of water the following reaction is possible:

$$WO_3 \, (s) + H_2 O \, (g) \rightleftharpoons WO_2(OH)_2 \, (g) \tag{3.5}$$

with the measured equilibrium constant k_{eq}

$$\log k_{eq} = \frac{-5840 \, \mathrm{K}}{T} + 1.216 \tag{3.6}$$

where T is the temperature [74]. At equilibrium ($k_{eq} = 1$) the free energy change for a reaction is zero. At a temperature below $0.75 T_{melt}^{WO_3}$ sublimation is dominated by

the aforementioned hydroxide formation [74]. The melting temperature $T_{melt}^{WO_3}$ of WO_3 is 1745 K [12].

Sublimation is continuous as the gas flow continuously transports the gas phase out of the reaction chamber. At temperatures above $0.75 T_{melt}^{WO_3}$ formation of W_3O_9 increasingly contributes to the sublimation. Thus, the difference between the sublimation rates in humid and dry atmosphere decreases as shown in Fig. 3.6 and given by equation 3.3 using the aforementioned parameters c_1 and Q for humid and dry air.

If a future fusion power plant such as DEMO had a W first wall armor, the radioactive hazard in case of a LOCA can be estimated based on the data shown in Fig. 3.6. A surface area of $1000 \, m^2$ of the first wall and a radioactivity of $8.74 \times 10^{14} \, Bq \, kg^{-1}$ is assumed [19]. This yields a potential release of up to $1 \times 10^{17} \, Bq/day$ at a temperature of 1273 K in humid air. A higher temperature, a higher humidity level, or a high flow gas flow rate along the surface can significantly increase this rate as discussed above. Such a release is a severe radioactive hazard for the environment. The need for smart alloys, as motivated and introduced in section 1.2, is confirmed under DEMO-relevant conditions in the laboratory.
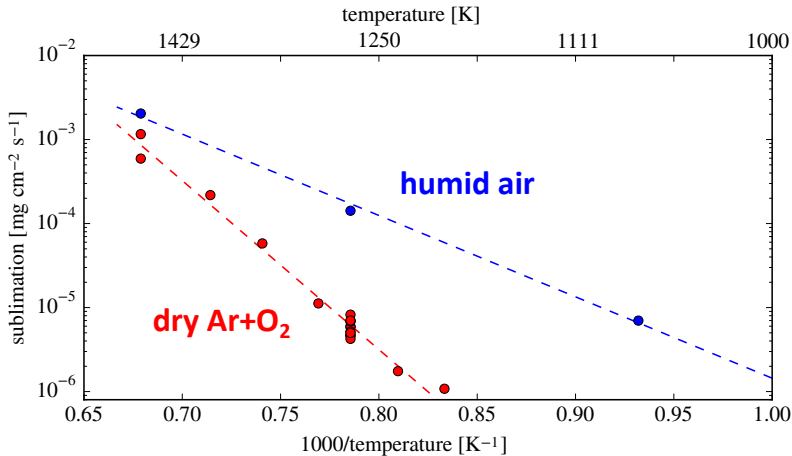
Figure 3.6: Sublimation rates of tungsten oxide as a function of time at atmospheric pressure. Two different atmospheres are selected: humid air with a relative humidity of 70 % at 313 K and in dry Ar with 20 % O_2.

Chapter 4

On volatilization of chromium oxide

Chromium (Cr) is a well known passivating element in alloys [40]. Other typical passivating elements are silicon (Si) and aluminum (Al) [40]. Si forms intermetallic phases with W and is therefore not suitable in combination with W [11]. Al forms radioactive isotopes with a half-life of 7.2×10^5 years under neutron irradiation [19]. Therefore Al is not suitable for application in a fusion power plant and Cr is the main candidate as a passivating element for smart alloys.

Passivation with Cr requires the formation of a protective Cr_2O_3 layer via the reaction

$$4\,Cr + 3\,O_2 \longrightarrow 2\,Cr_2O_3. \tag{4.1}$$

This reaction is energetically favorable as it has a Gibbs free energy $\Delta G = -5.3 \times 10^2\,kJ/(mol\,O_2)$ at 1273 K [51]. Cr_2O_3 has a melting temperature of 2708 K [40] and a Pilling-Bedworth ratio (PBR) of 2.05 [40]. Cr at the surface reacts with adsorbed O. Once there is a thin layer of Cr_2O_3, Cr ions diffuse to the surface of the Cr_2O_3 to react with O and increase the thickness of the oxide layer [75]. Oxidation resistance requires a protective oxide layer. Therefore, the protective Cr_2O_3 layer must be stable. Stability includes good adherence to the metal which will be studied on the alloy starting from chapter 5 and the absence of recession due to volatilization.

The stability with respect to volatilization of Cr oxide is measured for selected conditions: humid and dry air at 1273 K at a flow velocity of $\sim 0.1\,cm\,s^{-1}$. Higher temperatures and higher flow velocities of the surrounding gas increase the volatilization rate [40]. In this thesis, fully oxidized thin films deposited by magnetron sputtering are measured. The reason for the chosen method is similar to the explanations for W in section 3.2. The results are shown in Fig. 4.1. The measured mass loss of Cr_2O_3 in dry air at 1273 K is $0.4 \times 10^{-6}\,mg\,cm^{-2}\,s^{-1}$. This rate is close to the detection limit of the TGA. The mass change of a fully oxidized W-32Y film is measured under the same conditions as seen in Fig. 4.1. There is no significant change compared to pure Cr_2O_3 as yttria is stable. In contrast, the measured mass loss of Cr_2O_3 in humid air at 1273 K is $1.7 \times 10^{-6}\,mg\,cm^{-2}\,s^{-1}$. In this thesis the term 'humid air' refers to air with 5 vol.% humidity which equals a relative humidity of 70 % at 313 K. In comparison, a sublimation rate of $7 \times 10^{-6}\,mg\,cm^{-2}\,s^{-1}$ is measured for WO_3 in dry air at 1273 K as discussed in section 3.2 and included in Fig. 4.1.
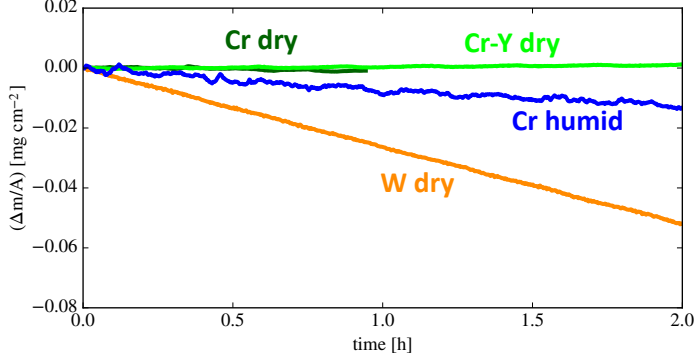
Figure 4.1: Mass change of fully oxidized thin films as a function of time. The samples are exposed at a temperature of 1273 K to dry or humid air at atmospheric pressure as indicated by the labels.

The volatilization of Cr_2O_3 in dry air happens via the reaction

$$Cr_2O_3 (s) + \frac{3}{2} O_2 (g) \longrightarrow 2 CrO_3 (g). \tag{4.2}$$
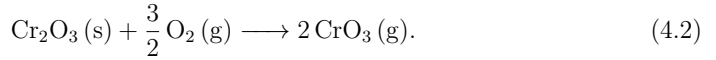
(s) indicates a solid phase whereas (g) indicates a gas phase. The equilibrium constant k of the reaction is measured as

$$\log_{10} k = \log_{10} \left(\frac{N_{CrO_3}^2}{N_{O_2}^{3/2}} \right) \approx -\frac{2.47 \times 10^4 \, \text{K}}{T} + 6.20 \tag{4.3}$$

where N_i are the number of particles i in the gas phase and T is the temperature [76]. Thus, the Gibbs free energy ΔG of the reaction is positive:

$$\Delta G \approx (4.7 \times 10^5 - 1.2 \times 10^2 \, \text{K}^{-1} \times T) \, \text{J} \tag{4.4}$$

Therefore, the reaction rate is slow, increases with temperature, and occurs only due to a continuous transport of the gas phase out of the furnace: in [77] a rate of $0.6 \times 10^{-6} \, \text{mg cm}^{-2} \, \text{s}^{-1}$ is measured at 1373 K which increases to $4 \times 10^{-6} \, \text{mg cm}^{-2} \, \text{s}^{-1}$ at 1473 K at the same gas flow, or to $2 \times 10^{-6} \, \text{mg cm}^{-2} \, \text{s}^{-1}$ at 1373 K with a 20 times higher gas flow.

In humid air there is also the reaction

$$Cr_2O_3 (s) + O_2 (g) + H_2O (g) \longrightarrow 2 CrO_2(OH) (g). \tag{4.5}$$
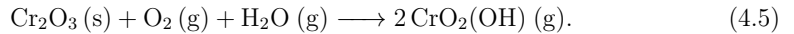
The equilibrium constant k' of the reaction is measured as

$$\log_{10} k' = \log_{10} \left(\frac{N_{CrO_2(OH)}^2}{N_{O_2} N_{H_2O}} \right) \approx -\frac{2.24 \times 10^4 \, \text{K}}{T} + 6.24 \tag{4.6}$$

where N_i is the number of particles i in the gas phase and T is the temperature [76]. Thus, the Gibbs free energy $\Delta G'$ of the reaction is positive:

$$\Delta G' \approx (4.3 \times 10^5 - 1.2 \times 10^2 \, \text{K}^{-1} \times T) \, \text{J} \tag{4.7}$$

Therefore, the reaction rate is low, increases with temperature, and occurs only due to a continuous transport of the gas phase out of the furnace. Nevertheless, the Gibbs free energy is lower as compared to the Gibbs free energy in equation 4.4, thus the volatilization rate of Cr_2O_3 is higher in humid air than in dry air.

In summary, Cr_2O_3 is more stable in dry air as compared to humid air. However, in all cases Cr_2O_3 is more stable than WO_3 and the formation of a protecting Cr_2O_3 layer on tungsten can mitigate consequences of a LOCA: the release of radioactive material should be suppressed by suppressing the formation of WO_3 due to a protecting layer.

Chapter 5

Oxidation of W-Cr-Y thin films

5.1 Pre-characterization of the thin films

After discussing the main alloying elements of smart alloys individually, the focus shifts to the interaction of the different elements in the alloyed material. The samples investigated are thin films produced by magnetron sputter deposition on sapphire substrates with a diameter of 1.1 cm. Details on the magnetron device and the sputtering process are given in [53] and section 2.1. Up to 15 substrates on a rotating plate under the plasma are coated with an alloy in parallel. No further treatments, such as annealing, polishing, or chemical reagents are applied after deposition before further investigations. This excludes the uncertainty on the reproducibility of these treatments.

The deposited films weigh 6 mg to 12 mg with a fluctuation below 2% for samples of the same deposition batch. The weight depends on the chosen sputtering time, typically around $1\,\mu g\,s^{-1}$ are deposited on a substrate. The thickness of a film is measured on a cross section after a FIB cut: it is found to be 3 μm to 8 μm. The surface area of the substrate, the film thickness, and the film mass yield the density of the films. A density of $(15.3 \pm 0.5)\,g\,cm^{-3}$ is achieved for W-11.6Cr-0.4Y films.

The microstructure of the films is shown in Fig. 5.1. The inset shows an electron microscopy image on the surface, whereas the main image shows a cross section. The grain diameter is around 0.2 μm. The image indicates a homogeneous film: no phase separation, no segregation of specific elements, and no oxide segregation are detected. As the films are sputter-deposited, an atomically dispersed distribution is expected. The experimental results do not contradict this expectation. The intensities of W, Cr, and YO in the SIMS measurement are constant with the depth in the sample, as shown in Fig. 5.2. Only O has a slightly increased intensity within the first 0.2 μm. The detection sensitivity is different for different elements. Therefore, the counts are not proportional to the relative composition. The measurements of the microstructure and the SIMS profile indicate a homogeneous film.
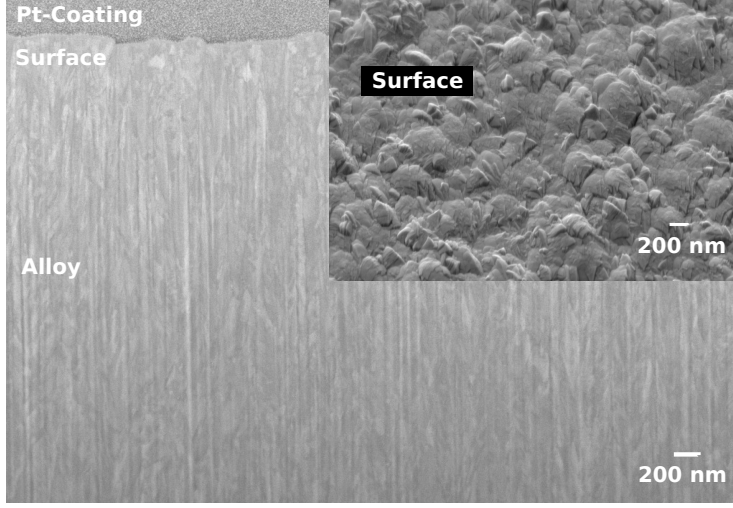
Figure 5.1: Electron microscopy images of a thin film alloy as deposited. The composition of the film is W-13Cr-1Y as measured by ICP-OES (see section 2.7). The cross section depicts the protective platinum (Pt) coating and the alloy; the surface is shown in the inset. Figure adapted from F. Klein et al. [78].
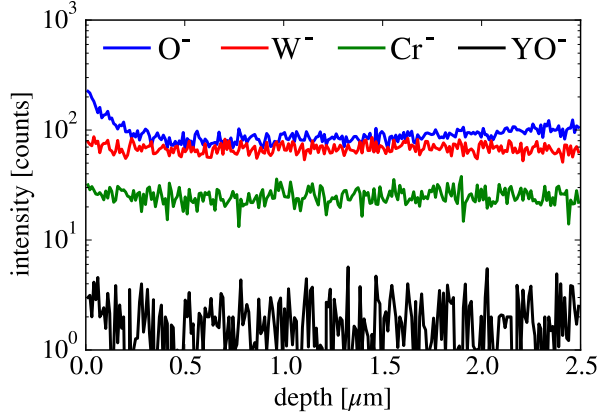
Figure 5.2: Exemplary SIMS results for thin films as deposited by magnetron sputtering. The composition of the film is W-12Cr-0.5Y alloy. Figure adapted from F. Klein et al. [78].

The homogeneity of the film allows to calculate the theoretical density ρ_t of the film in first approximation using the rule of mixture:

$$\rho_t = 100 / \sum_i \frac{c_i}{\rho_i} \tag{5.1}$$

where c_i is the concentration of element i in weight % and ρ_i the density of the pure element i. The calculation yields a density of 96 % relative to the theoretical density for

the W-11.6Cr-0.4Y film mentioned above. This calculation assumes all elements in the metallic form. Oxides typically have lower densities as compared to the metal they are formed from - thus the relative density of the film would increase if oxides were considered. In fact, an O content of ~ 8 at. % is measured using XPS. The standard free energy of the reaction $4\,Y + 3\,O_2 \longrightarrow 2\,Y_2O_3$ is $-1.2\,MJ\,mol^{-1}$ [79], Y oxidizes at room temperature. The O content and the free energy yield the assumption that all yttrium in the alloy is in the form of yttria. The oxygen content is higher than in a W-10Cr-2Ti alloy compacted by pressureless sintering and subsequent HIPing as described in [55] where an O content of ~ 2 at. % was reached. Pumping the magnetron chamber to a better vacuum level before sputtering is one approach to reduce the oxygen content of the films. In the present study a pressure threshold of $1 \times 10^{-6}\,mbar$ is selected before the sputtering process is started. The detailed influence of the O content on the properties of the alloy is a subject to future investigations.

The lattice structure of the films is analyzed using XRD. The result is shown in Fig. 5.3. All main W peaks are visible, no peaks at positions characteristic for pure Cr are found. This finding indicates a W-like lattice structure. Relative intensity, peak width, and peak position are the three main characteristics of the peaks in an XRD:

- The relative intensity is proportional to the probability that the X-ray is reflected on the corresponding lattice plane. Literature data assumes an isotropic crystal orientation. However, the magnetron films in this study have elongated sub-micron grains (as seen in Fig. 5.1) due to a defined growth direction. The elongation is in agreement with literature expectations for the selected process parameters [80]. Thus, the crystal is anisotropic. Relative intensities are changed compared to isotropic crystal orientations and little information on the crystal structure can be obtained based on the relative intensities.

- The peak width indicates the variation in the lattice constant. Broader peaks have a larger variation in lattice constant typically due to defects and strain in the material. For example, the peak at $2\Theta = 73.1°$ has a full-width-half maximum (FWHM) of $1.8°$ in Fig. 5.3. This is broader as compared to the FWHM of that peak measured on a pure W sample prepared by magnetron sputtering where a FWHM of $0.3°$ is measured. The increased variation in the lattice constant is induced by alloying.

- The peak position allows to calculate the lattice constant via Bragg's law given in equation 2.3. The peak positions of the four main peaks in Fig. 5.3 are given in table 5.1. The positions yield a lattice constant of

$$a = (1.002 \pm 0.004) \times a_{\mathrm{W}} \tag{5.2}$$

with the lattice constant of pure W $a_{\mathrm{W}} = 3.1648\,Å$ [81]. In other words, the lattice constant of the alloy differs by less than $1\,\%$ compared to that of pure W.

In a perfect substitutional solid the lattice constant a_{Vegard} can be calculated using Vegard's approximation:

$$a_{\mathrm{Vegard}} = x_A \times a_{\mathrm{Cr}} + (1 - x_A) \times a_{\mathrm{W}} = 0.97 \times a_{\mathrm{W}} \tag{5.3}$$

where $x_A = 12\,wt.\,\% = 32\,at.\,\%$ is the Cr concentration and $a_{\mathrm{Cr}} = 2.91\,Å$ the Cr lattice constant [82]. Equations 5.2 and 5.3 contradict each other. Therefore, the assumption of a perfect substitutional solid is not valid and Vegard's approximation cannot be used for the magnetron deposited films.
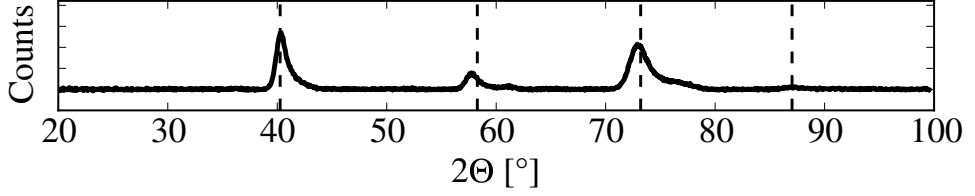
Figure 5.3: XRD measurement of an deposited W-12Cr-0.5Y film. The black, dashed lines indicate the expected peak-positions for W [81]. Figure adapted from F. Klein et al. [78].

Table 5.1: Measured positions of peaks in the XRD shown in Fig. 5.3 compared to literature data for peaks in pure W.

	(110)-Plane	(200)-Plane	(211)-Plane	(220)-Plane
pure W [81]	40.265°	58.276°	73.198°	87.024°
W-12Cr-0.5Y	40.4°	57.8°	73.1°	87.1°

In summary, the magnetron deposition provides multiple dense films with a homogeneous distribution of alloying elements, and a W-like lattice structure. These films are used to study fundamental properties of the W-Cr-Y alloy at elevated temperatures: the films were used to optimize the elemental composition [30, 53], obtain a first understanding on how humidity influences the oxidation process [83, 53], and to study the effects of annealing onto the material [53]. The following section presents an overview of the oxidation kinetics of W-Cr-Y thin films, complementary discussions of the data is found in T. Wegener [53] and F. Klein et al. [78]. In this thesis the results are shown as motivation and benchmark for the studies on bulk samples in the following chapters.

5.2 Kinetics of the oxidation process of W-Cr-Y films

5.2.1 Mass change due to oxidation

In this section the kinetic of the oxidation process is determined using the mass change. The mass change of the films deposited by magnetron sputtering is measured at a temperature of 1273 K at atmospheric pressure, with 20 kPa O_2 and 80 kPa Ar partial pressure. The results for W, W-Cr, and W-Cr-Y are shown in Fig. 5.4.

The binary W-Cr alloy shows parabolic oxidation kinetics with a rate of $6 \times 10^{-3}\,\mathrm{mg^2\,cm^{-4}\,s^{-1}}$. The minimum gradient of the mass gain with respect to time is $4 \times 10^{-5}\,\mathrm{mg\,cm^{-2}\,s^{-1}}$. The film detaches from the substrate after 15 min, indicating a complete failure of the protective function. The mass change of pure W oxidized at the same conditions is also shown in Fig. 5.4 for comparison. The linear mass gain rate is $6 \times 10^{-3}\,\mathrm{mg\,cm^{-2}\,s^{-1}}$, details are discussed in section 3.1.1.

W-Cr-Y films show oxidation kinetics with three distinct stages as published by F. Klein et al. [78]:

1. In stage I the 7.6 μm thick sample shows a parabolic oxidation rate of $2 \times 10^{-5}\,\mathrm{mg^2\,cm^{-4}\,s^{-1}}$. The parabolic oxidation rate of the 3.6 μm thick sample with the optimized composition is four times lower. Stage I lasts 0.5 h for both samples.

2. In stage II the parabolic oxidation rate of the 7.6 μm thick sample is reduced to $5 \times 10^{-6}\,\mathrm{mg^2\,cm^{-4}\,s^{-1}}$. The minimum gradient is $4 \times 10^{-6}\,\mathrm{mg\,cm^{-2}\,s^{-1}}$. Stage II lasts for 8.5 h; the sample of 3.6 μm thickness with the optimized composition shows a lower parabolic oxidation rate of $2 \times 10^{-6}\,\mathrm{mg^2\,cm^{-4}\,s^{-1}}$. However, stage II only lasts for 1.8 h.

3. In stage three the oxidation kinetics changes to a linear mass gain at a higher rate. Rates of $5 \times 10^{-5}\,\mathrm{mg\,cm^{-2}\,s^{-1}}$ and $2 \times 10^{-5}\,\mathrm{mg\,cm^{-2}\,s^{-1}}$ are measured for the 3.6 μm and 7.6 μm thick samples, respectively.
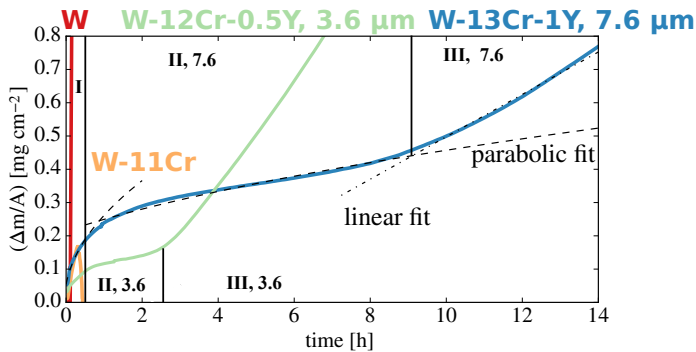
Figure 5.4: Mass change of thin films as a function of time measured at a temperature of 1273 K at a pressure of 20 kPa O_2 plus 80 kPa Ar. Oxidation stages I-III are labeled, the numbers 3.6 and 7.6 refer to the sample thickness of 3.6 μm and 7.6 μm, respectively. Figure adapted from F. Klein et al. [78].

5.2.2 Microstructure of the formed oxide scale

The discussion of the oxidation stages presented in the previous section 5.2.1 requires information on the microstructure. Therefore, the microstructure at each stage of the oxidation process is shown on samples where the oxidation process is interrupted. The discussion using information on the mass change (section 5.2.1) and the microstructure follows in the next section 5.2.3. W-12Cr-0.5Y samples from the same batch with a thickness of 3.6 µm are oxidized at 1273 K in 20 kPa O_2 and 80 kPa Ar atmosphere. The microstructure images acquired using electron microscopy are correlated with SIMS and EDX measurements, as shown in Fig. 5.5. The Pt coating visible in the cross sections is deposited just before cutting in order to avoid damage of the surface, as explained in section 2.13.

The electron microscopy on the cross sections cannot resolve Y. The fine distribution of Y is addressed in more detail using STEM measurements presented in section 9.2.

Oxidation stage I

The microstructure after 10 min of oxidation is shown in Fig. 5.5 a. The mass of the sample increased by 0.08 mg during these 10 min. The grain size of the surface oxide layer is below 0.1 µm, as seen in the surface image in the inset of Fig. 5.5 a. The cross section in Fig. 5.5 a in combination with the overlaid EDX line scan show a layered structure: the surface chromium oxide layer, where the W signal vanishes, is (0.15 ± 0.04) µm thick; the alloy beneath is (3.30 ± 0.03) µm thick. The line scan is conducted within the box where it is plotted using an electron energy of 5 keV. Therefore, there is only a combined signal for the main peaks of Cr at 0.57 keV and O at 0.52 keV. EDX at 10 keV, exciting also the Cr peak at 5.4 keV, identifies the darker spots within the alloy to be chromium oxide. These darker spots are referred as internal oxides in the following. Based on graphical analysis (counting the dark and the bright pixels on a cross section) the internal oxides constitute approximately 2 % of the imaged area in Fig. 5.5 a.

Oxidation stage II

The microstructure after 75 min of oxidation is shown in Fig. 5.5 b. The mass of the sample increased by 0.18 mg during these 75 min. The grain size of the surface oxide layer is around 0.1 µm, as seen in the surface image in the inset of Fig. 5.5 b. The cross section in Fig. 5.5 b in combination with the overlaid SIMS spectrum shows a layered structure: the surface chromium oxide layer, where the W signal vanishes, is (0.23 ± 0.04) µm thick; the alloy beneath is (3.31 ± 0.03) µm thick. The SIMS measurement is not attributed to a specific region in the cross section as it is based on a crater much larger than the cross section (see section 2.11). Based on graphical analysis of the cross section the internal oxides constitute approximately 8 % of the imaged area in Fig. 5.5 b. In comparison to the sample in oxidation stage I the thickness of the oxide layer and the amount of internal oxides increase, whereas the thickness of the alloy remains constant. Further, EDX analysis at 10 keV indicates a reduction of the Cr concentration in the alloy from initially 12 wt. % down to 8 wt. %. The SIMS measurement shows a constant W signal throughout the alloy. The Cr and O signals gradually decrease from a depth of 0.5 µm to 2 µm and remain constant afterwards.

Oxidation stage III

The microstructure after 8 h of oxidation is shown in Fig. 5.5 c. The mass of the sample increased by 1.12 mg during these 8 h. The cross section in Fig. 5.5 c in combination with the overlaid EDX line scan at 5 keV shows a layered structure with two different oxides: the top layer is (0.2 ± 0.1) µm thick tungsten oxide with grains of a few 100 nm. Below, there is a (0.4 ± 0.1) µm thick layer of Cr_2O_3. There are small white spots encapsulated in the Cr_2O_3 layer, an example is marked in Fig. 5.5. They are identified as W by EDX. Pores are observed mainly at the interface of the Cr_2O_3 layer and the alloy. The alloy has a thickness of (3.54 ± 0.05) µm. The increased thickness compared to Fig. 5.5 a,b is attributed to the volume expansion of the internal oxides. The internal oxides are found throughout the entire alloy and cover about 20 % of the imaged area. EDX analysis at 10 keV indicates a Cr concentration in the alloy of 7 wt. %.

Binary W-11Cr

The microstructure of a binary W-11Cr film after 15 min of oxidation is shown in Fig. 5.5 d. The film is already partially delaminated. SEM and SIMS results of the intact region are shown in Fig. 5.5 d. The surface image shows a hilly surface with grains of around 0.1 µm. The cross section in Fig. 5.5 d in combination with the overlaid SIMS spectrum shows a layered structure: on the surface there is a few nm thick layer of W-O. The layer is not fully closed. Below, there is a closed layer of Cr_2O_3. The thickness of the Cr_2O_3 layer is (0.19 ± 0.04) µm. Below the Cr_2O_3, there is a layer of mixed W-Cr-O. The mixed oxide has a thickness of (0.64 ± 0.09) µm including visible pores. Below the mixed oxide, there is the alloy. Some pores and little internal oxides are visible in the first ~ 0.3 µm of the alloy. The SIMS profile shows a local minimum in the Cr signal in this region. Internal oxides are visible in the central region of the film. At higher depth internal oxides are no longer visible and the pure alloy is found. The oxygen signal of the SIMS measurement has a maximum at the surface and gradually decreases with depth to the minimum at the interface of the alloy to the substrate. The consequences of the minimum are discussed in the following section 5.2.3.
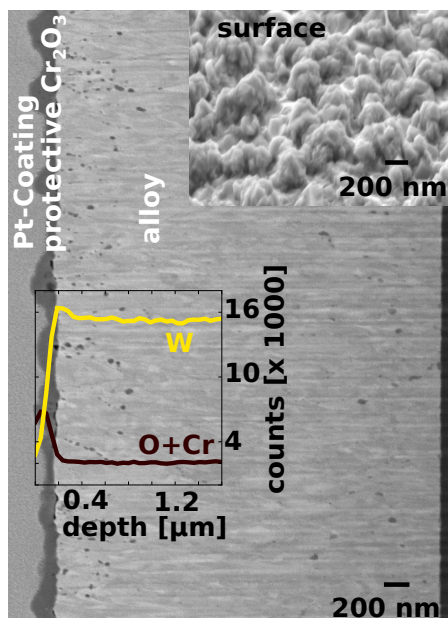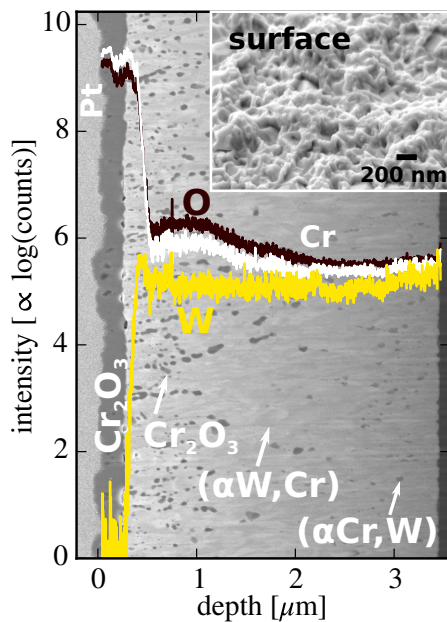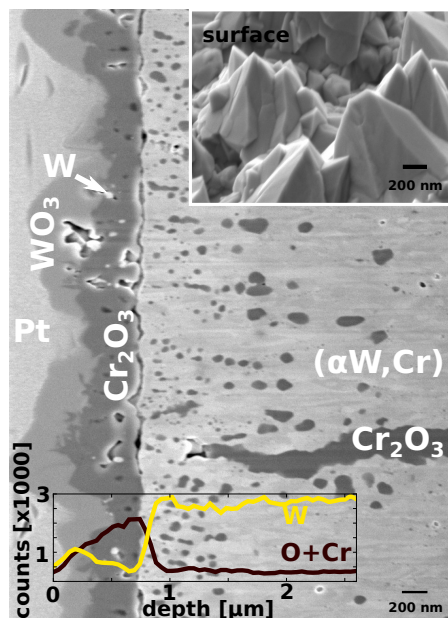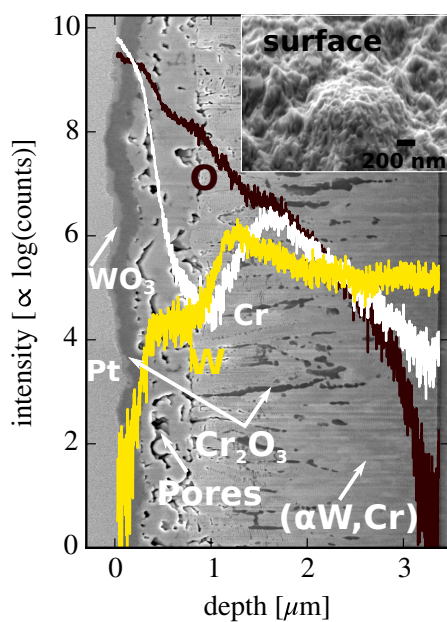
Figure 5.5: Cross sections combined with EDX line scans along the box in which they are plotted (**a**,**c**), SIMS (**b**,**d**) and surface images in the inset show the different stages of the oxidation process. (**a**–**c**) show a ternary W-12Cr-0.5Y alloy, whereas (**d**) shows the binary W-11Cr alloy. They are oxidized at $1273\,\mathrm{K}$ in $20\,\mathrm{kPa}$ O_2 and $80\,\mathrm{kPa}$ Ar atmosphere for (**a**) $10\,\mathrm{min}$; for (**b**) $75\,\mathrm{min}$; for (**c**) $8\,\mathrm{h}$; and for (**d**) $15\,\mathrm{min}$. Figure adapted from F. Klein et al. [78].

5.2.3 Understanding and evaluation of the oxidation kinetics

Oxidation stage I - why passivation works

In oxidation stage I only Cr_2O_3, no WO_x, forms as shown by SEM/EDX measurements (see Fig. 5.5 a). This observation can be understood by looking at the Gibbs free energies assuming sufficient Cr at the surface: the Gibbs free energy for the reaction

$$4\,Cr + 3\,O_2 \longrightarrow 2\,Cr_2O_3 \tag{5.4}$$

at a temperature $T = 1273\,K$ is

$$\Delta G_{Cr_2O_3}^{T=1273\,K} = -5.3 \times 10^2 \,kJ/(mol\,O_2)\,[41]. \tag{5.5}$$

In comparison, the Gibbs free energy for the reaction

$$2\,W + 3\,O_2 \longrightarrow 2\,WO_3 \tag{5.6}$$

at the same temperature is less negative:

$$\Delta G_{WO_3}^{T=1273\,K} = -3.6 \times 10^2 \,kJ/(mol\,O_2)\,[41]. \tag{5.7}$$

Based on these energies Cr is more affine to O_2 than W and any Cr oxidizes before W can oxidize. Any Y_2O_3 remains stable in the presence of W or Cr as the Gibbs free energy of the reaction of Y to Y_2O_3 is very low:

$$\Delta G_{Y_2O_3}^{T=1273\ K} = -1.4 \times 10^3 \,kJ/(mol\ O_2)\,[41] \tag{5.8}$$

Throughout oxidation stage I the oxide layer grows to a thickness of $0.2\,\mu m$ at a parabolic rate law of $k_p = 2 \times 10^{-5}\,mg^2\,cm^{-4}\,s^{-1}$, faster than a combined rate law throughout stages I and II would predict. There are three hypothesizes explaining this behavior: the first hypothesis is that the faster oxidation rate in stage I as compared to stage II is caused by the fact that the grain size of the oxide is similar to the oxide layer thickness. The edges of certain oxide grains provide a fast diffusion path for ions and cause fast oxidation. The second hypothesis is that yttria accelerates the oxidation process by offering additional nucleation sites. Nucleation sites are observed and discussed in more detail in section 9.2. The third hypothesis is connected to the atomic deposition during magnetron sputtering. A fraction of Cr atoms can be deposited into dislocations being faster available for oxidation as compared to other atoms. All the hypothesizes require further experimental and theoretical support. However, it is important that a closed, protective oxide layer forms as fast as possible in order to achieve passivation after the formation of the protective layer. This is achieved.

Oxidation stage II - Cr consumption

In oxidation stage II still only Cr_2O_3, no WO_x, forms as shown by SEM/EDX measurements (see Fig. 5.5 b). The suppression of WO_x formation is achieved by continuously replenishing Cr to the growing protective oxide layer on top of the alloy. The alloy has a constant thickness throughout stages I and II. The constant thickness of the alloy allows to exclude a continuous loss of WO_3 by sublimation at the rate of WO_3 formation. More advanced studies on sublimation are performed in chapter 8. A continuous replenishing of Cr requires a sufficiently fast diffusion of Cr within the alloy.

The protective layer keeps the partial oxygen pressure below the Cr_2O_3 layer sufficiently low to avoid W oxidation: W oxidizes at a partial oxygen pressure of 10^{-9} Pa at 1273 K whereas Cr requires only 10^{-17} Pa [79].

In comparison, there is the binary W-Cr alloy shown in Fig. 5.5 d. The observed local minimum in the Cr concentration indicates an interruption in the Cr supply and causes W oxidation to start - such a minimum is not found in the ternary W-Cr-Y alloys, see Fig. 5.5 a,b. Therefore, in the absence of Y the Cr diffusion in the alloy is too slow to continuously replenish the protective layer.

Formation of the protective oxides consumes Cr from the alloy. The mass of the Cr_2O_3 is given by

$$m_{ox} = N \times (2m_{Cr} + 3m_O)　\quad (5.9)$$

where m_i is the atomic mass of element i and N is given by the measured mass change

$$\Delta m = N \times 3m_O. \quad (5.10)$$

Thus, the mass of Cr which reacted to the oxide is given by

$$m_{ox}^{Cr} = N \times 2m_{Cr} \quad (5.11)$$

m_{ox}^{Cr} can be subtracted from the total Cr reservoir in the alloy and a new Cr concentration c_{new}^{Cr} can be calculated. This calculation yields $c_{new}^{Cr} \approx 5$ wt. % at the end of oxidation stage II in the ternary alloy. However, this calculation neglects the fact that W oxidizes at the edge of the sample due to weaker adhesion of the protective layer at the edge. The mass gain caused by oxidation of W at the edge of the sample must be subtracted from Δm before calculating N in equation 5.10. This correction yields the metallic Cr content in the alloy at the end of oxidation stage II $c_{new}^{Cr} \approx 8$ wt. %. The calculation is in agreement with the results from EDX.

Previously [30] it is presented that effective passivation requires more than 8 wt. % of Cr. Therefore, the oxidation kinetics changes and oxidation stage III starts, as seen in Fig. 5.4. The larger the Cr reservoir of a sample, the longer it takes to deplete it to around 8 wt. % of Cr and the longer it remains in oxidation stage II.

Oxidation stage III - failure of the protective function

In oxidation stage III both Cr_2O_3 and WO_x form as shown by SEM/EDX measurements (see Fig. 5.5 c). The Cr reservoir is depleted as discussed in the previous paragraph. Therefore, the Cr supply is no longer sufficient to suppress the formation of tungsten oxides. The new tungsten oxides form on top of the previously formed Cr_2O_3 layer, as seen in Fig. 5.5 c. This observation requires diffusion of W through the oxide layer. The small W spots in the Cr_2O_3 layer are an indication for the diffusion process. W^{6+} ions have a mass of 184 u and an ionic radius of 74 pm [84]. In comparison, Cr^{3+} and O^{2-} ions have a mass of 52 u and 16 u with ionic radii of 75.5 pm and 126 pm, respectively [84]. Thus, their masses are lower but their ionic radii are larger as compared to W^{6+} ions and diffusion of W ions through the oxide layer is geometrically plausible. The voids shown in Fig. 5.5 c at the interface of the Cr_2O_3 layer and the alloy form due to the outward diffusion of W. The flux of W ions through the Cr_2O_3 layer decreases with the thickness of the Cr_2O_3 layer. Therefore, the oxidation rate in stage III is lower in the 7.6 μm thick sample with a thicker oxide layer at the transition to oxidation stage III as compared to the 3.6 μm thick sample.

The protective layer is weakened by the outward diffusing W and more O can penetrate causing more internal oxidation. The WO_3 on the surface sublimates. Therefore, stage III corresponds to a failure stage of the protective function and it must not be reached in any accidental scenario of a future fusion power plant.

Interpolations to an accident in DEMO

In a LOCA in DEMO the alloy must remain in oxidation stages I and II to mitigate the radioactive hazard due to sublimation of tungsten oxide. The 3.6 µm thick films in this chapter remained for 2.3 h in stages I and II. In DEMO, the first wall armor will have a thickness of around 2 mm. The difference in thickness changes the Cr reservoir and thus also the expected lifetime.

First experimental evidences for a homogeneous Cr concentration in the W-Cr-Y alloy are presented in section 5.2.2, further evidences follow in section 9.1. The interpolation to a larger thickness of the alloy assumes that a homogeneous Cr concentration is also maintained in the thicker alloy. Such a homogeneous concentration can be maintained by sufficiently fast diffusion of Cr within the alloy yielding a gradual decrease of the Cr concentration with oxidation time. The consumed Cr is calculated using equations 5.10, 5.11, and the measured parabolic oxidation rate k_p

$$\Delta m = \sqrt{k_p t}; \; k_p = 5 \times 10^{-6} \, \text{mg}^2 \, \text{cm}^{-4} \, \text{s}^{-1} \tag{5.12}$$

The density of the alloy is $\rho \approx 15 \, \text{g} \, \text{cm}^{-3}$. With this information the time required for the Cr concentration to decrease from 12 wt. % down to 8 wt. % can be calculated as a function of the alloy thickness. This calculation yields 0.5 h and 2.2 h for the 3.6 µm and 7.6 µm thick samples, respectively. 2.3 h and 9 h are measured and the calculation underestimates the performance. This underestimation is caused by the fact that k_p also includes the faster mass gain at the edge of the sample - the k_p of an infinite sample would be even smaller. Despite the underestimation of the performance, the calculation predicts a time of 10 years until the protective function of a 2 mm thick alloy fails due to Cr depletion. However, the critical temperature would be maintained only for a few months in the accidental scenario of DEMO [17]. Erosion during operation of the power plant can reduce the thickness of the armor material. However, even if the thickness is reduced to only 0.5 mm the calculation predicts a time of 1 year until the protective function fails.

These interpolations predict that a W-Cr-Y alloy can withstand a LOCA with a temperature rise to 1273 K in dry air and suppresses the release of radioactive material. In the following chapters this prediction is verified using bulk alloys.

Summary of the oxidation studies on thin films

- Thin films deposited by magnetron sputtering are an idealistic system to study the oxidation resistance in the laboratory.

- Oxidation resistance of W-Cr-Y thin films is shown, a protective Cr_2O_3 layer forms on the surface. The addition of Y is crucial for the oxidation resistance. More details on understanding the effect of Y are presented in chapter 9.

- The small material reservoir in thin films limits the tests to a duration of only a few hours.

- The failure of the protective oxide is studied and a sufficient lifetime of bulk samples in DEMO is predicted.

Chapter 6

Towards bulk W-Cr-Y alloys from FAST

6.1 Why bulk alloy materials are needed

Chapter 5 presents how W-Cr-Y thin films successfully suppress the formation of WO_x. Thin films have a thickness of less than $10\,\mu m$, yielding a limited reservoir of material. Therefore, due to the limited material reservoir the oxidation time of thin films is limited to a few hours as discussed in section 5.2. However, a LOCA in DEMO requires good oxidation resistance for weeks. A larger material reservoir due to a thickness of a few millimeters is the key advantage of bulk alloys. Oxidation experiments over weeks, DEMO relevant time scales, are only possible using bulk samples.

The deposition of a $1\,mm$ thick film in the magnetron with the parameters as used in chapter 5 would require around $400\,h$. However, the magnetron requires cleaning after $3\,h$ to $4\,h$ of sputtering. Thus, it is not feasible to deposit bulk alloys using the magnetron. Bulk samples should be manufactured using a technology which is up-scalable for production of the first wall in a future fusion power plant. Here, a powder-mechanical route is selected [56]: first, the powder is mechanically alloyed in a planetary ball mill (see section 2.2 and [53]). Based on the results from [30], powders with the composition W-11.4Cr-0.6Y are alloyed. Second, the alloyed powder is compacted by Field Assisted Sintering Technology (FAST), details of the method are described in chapter 2 and in [56, 53]. As compared to the magnetron films a set of new free parameters arises:

- The mechanical alloying has free parameters. Most important are the duration, ball-to-powder ratio, rotation speed, and ball size. The parameters used in this work are given in section 2.2. Detailed research on mechanical alloying of W-Cr-Y powders is found in [53].

- The sintering process has free parameters. Most important are the pressure, the heating rate, the maximum sintering temperature, and the holding time at the maximum sintering temperature. The influence of the different parameters on the microstructure of the alloy and the consequences on the oxidation resistance are investigated in chapter 7.

- After sintering the alloy is cut and ground, as explained in section 2.4. Investigations on how the shape of the sample and the surface roughness influence the oxidation behavior are presented in chapter 7.

6.2 From powder to the bulk sample: processing and understanding

This section focuses on the compacting process itself. The compacting process is an essential step of the alloy production. Therefore, it is investigated here. The influence of the microstructure on the oxidation resistance is studied only in the following chapter 7. For the work in this chapter 6, the pressure during sintering is fixed at 50 MPa, the heating rate is $200 \, \mathrm{K \, min^{-1}}$, the cooling rate is $300 \, \mathrm{K \, min^{-1}}$, and the holding time at the maximum sintering temperature is $0 \, \mathrm{s}$. In other words, all parameters except the maximum sintering temperature (T_{max}) are kept constant.

Fig. 6.1 a shows the sample temperature during sintering as a function of time. Heating is stopped at 1740 K, 625 s after starting the machine. This point is marked with a vertical line in Fig. 6.1. Fig. 6.1 b shows the displacement speed of the stamp during sintering as a function of time. A high displacement speed corresponds to a high compacting rate of the sample, whereas a displacement speed of $0 \, \mathrm{mm \, min^{-1}}$ indicates that the sample cannot be compacted further. The displacement speed drops towards $0 \, \mathrm{mm \, min^{-1}}$ just before the mark of 625 s at a temperature of 1733 K. The increased displacement speed during cooling is caused by thermal shrinking of the sample and the graphite die. Thus, full compacting is achieved once the sintering temperature reaches $\sim 1730 \, \mathrm{K}$. A relative density of 99 % is measured on samples sintered at up to 1740 K using Archimedes principle, as described in section 2.8.

The C content is $2 \times 10^2 \, \mathrm{ppm}$, measured using the LECO carbon determinator CS600 (see section 2.5). A similar C content was found in different W-Cr-Y alloys [85]. The aforementioned alloys were produced by mechanical alloying followed by Hot-Isostatic Pressing (HIP), not by FAST as the alloys in this work. Thus, the main C sources seem to be the WC milling jar and the WC milling balls which were used in both studies. Studies on pure W showed an increase of the ductile to brittle transition temperature of almost 200 K due to the addition of 60 ppm of C [86]. However, the consequences of C impurities on W-Cr-Y alloys are not yet studied systematically - the interpolation from pure W to the alloys on the influence of C is doubtful. Smart alloys are not intended to be used as structural materials, thus a slight increase in embrittlement is not crucial.

Other impurities are $(0.153 \pm 0.002) \, \mathrm{wt. \%} \, O_2$ and $(8 \pm 1) \times 10^{-3} \, \mathrm{wt. \%} \, N_2$ measured using a LECO determinator (see section 2.6). In comparison, the reaction of all Y contained in the alloy to Y_2O_3 would require $0.16 \, \mathrm{wt. \%}$ of O, which is more than the total content of O in the alloy. Details on the distribution of Y and O in the alloy are

(a)   (b)
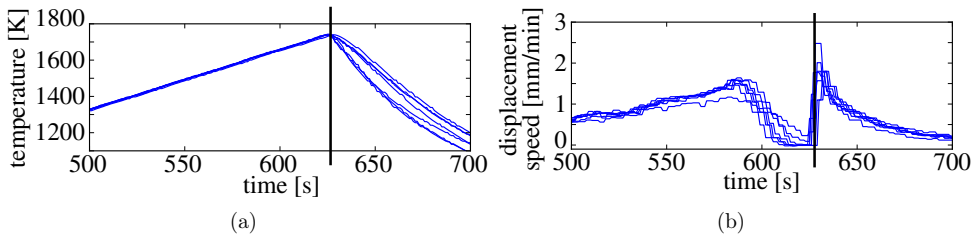
Figure 6.1:   (**a**) The sample temperature measured by the pyrometer as a function of time during FAST is plotted for multiple samples. (**b**) The displacement speed of the punch as a function of time during FAST is plotted for multiple samples.

shown in section 9.

A dedicated set of experiments on the compacting process is performed: the FAST process is interrupted at different stages from the powder after milling to a fully compact sample. The obtained material is analyzed using the electron microscope and XRD. The sintering is interrupted at T_{max} of 1279 K, 1449 K, and 1614 K. Surface images of the powder and the sintered samples are shown in Fig. 6.2. The powder is pressed onto graphite tape. The sintered samples are ground with P1200-grade SiC abrasive paper and cleaned with isopropanol.

The powder is shown in Fig. 6.2 a. Particles and agglomerates from sub-µm size to around 20 µm are found. The sample interrupted at 1279 K has a relative density of $\sim 70\,\%$. It is shown in Fig. 6.2 b and looks very similar to the powder. A flat surface or scratches from grinding are not visible as the sample disassembles in the isopropanol bath. The sample interrupted at 1449 K is shown in Fig. 6.2 c. It has a relative density of $\sim 80\,\%$, the powder particles are no longer visible on the surface, the small black spots on the surface are the remaining pores. Scratches from polishing are visible. The sample interrupted at 1614 K has a relative density of 98 %, a surface image is shown in Fig. 6.2 d and looks very similar to the fully sintered sample shown in Fig. 6.2 e.

The cross sections corresponding to the surface images in Fig. 6.2 are shown in Fig. 6.3. The powder is shown in Fig. 6.3 a: there are pores within the agglomerates and open spaces between different agglomerates. The color contrast within the agglomerates is small, indicating full alloying of W, Cr, and Y. See [53] for deeper analysis of the alloyed powder.

(a) 300 K

(b) 1279 K

(c) 1449 K

(d) 1614 K

(e) 1740 K
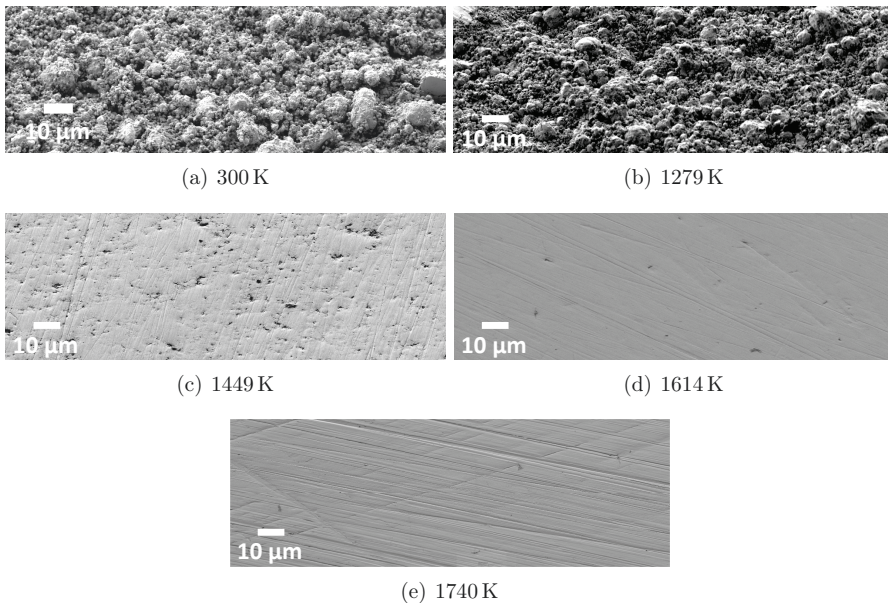
Figure 6.2: Surface images of samples in different stages of the sintering process. (**a**) powder after mechanical alloying. The sintering is interrupted at a temperature of (**b**) 1279 K, (**c**) 1449 K, and (**d**) 1614 K. (**e**) shows the fully sintered sample compacted at up to 1740 K.

After sintering to 1279 K the agglomerates and particles of the powder are pressed together, as shown in Fig. 6.3 b. However, there remain large pores between the particles and the structure of the particles remains the same as compared to the powder.

Only few pores remain after sintering to 1449 K, as shown in Fig. 6.3 c. A Cr-rich phase starts to form in the vicinity of the pores, at the edges of the original powder particles.

(a) 300 K

(b) 1279 K

(c) 1449 K

(d) 1614 K

(e) 1740 K
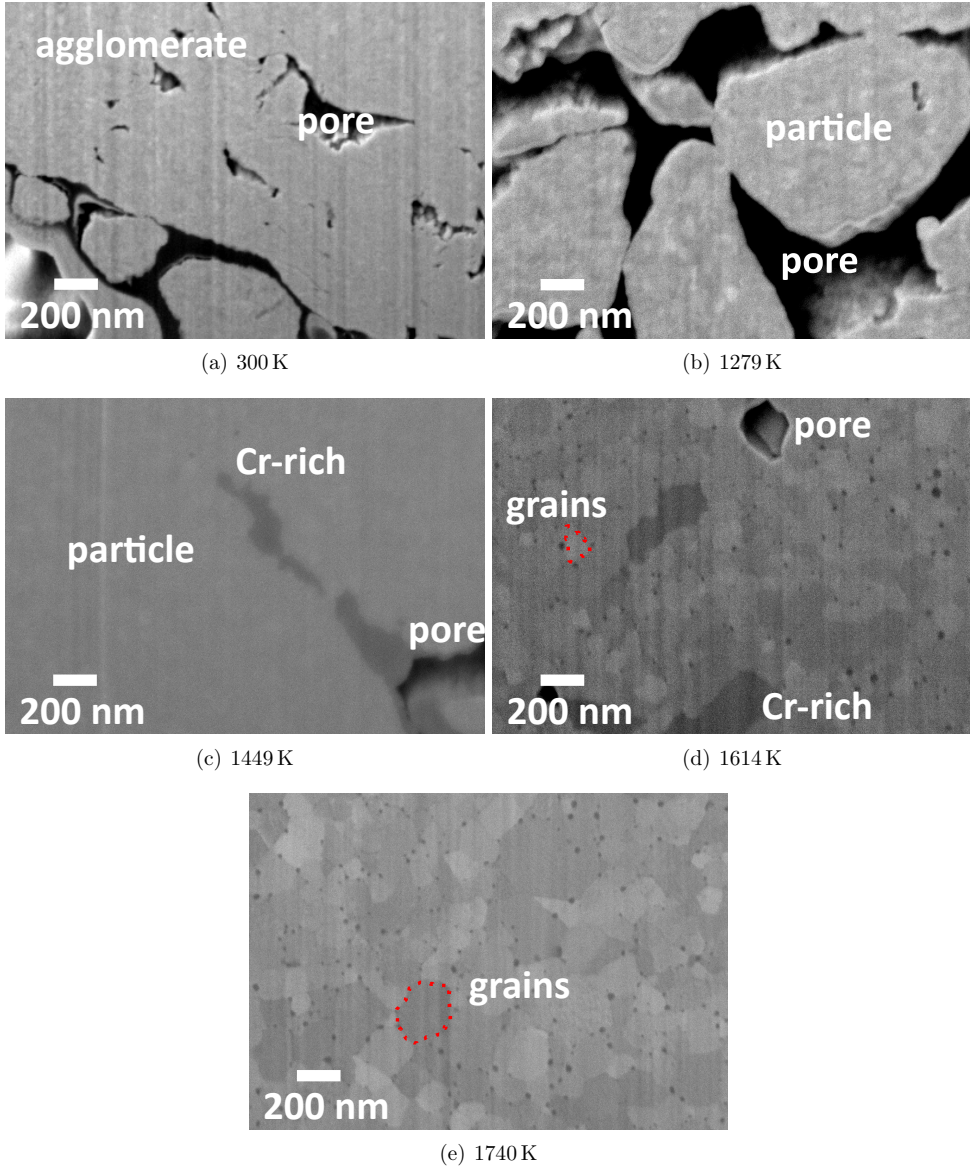
Figure 6.3:   Cross sections of samples in different stages of the sintering process. (**a**) powder after mechanical alloying. The sintering is interrupted at a temperature of (**b**) 1279 K, (**c**) 1449 K, and (**d**) 1614 K. (**e**) shows the fully sintered sample.

A cross section of the sample sintered to 1614 K is shown in Fig. 6.3 d: the original powder particles vanished. Instead, sub-micron grains with Y-Cr-O nano-particles (black points) are visible, an analysis of the nano-particles using atom-probe tomography is shown in section 9.2.2. Locally there remain a few grains with an increased Cr content and a few small pores. The small pores are in agreement with the slightly reduced density as compared to the fully sintered sample.

The fully sintered sample is shown in Fig. 6.3 e. The Cr-rich grains and the pores vanished. A single W-Cr phase with a sub-micron grain size and yttrium containing nano-particles is found.

The XRD of the aforementioned samples in different stages of the sintering process are shown in Fig. 6.4 where Fig. 6.4 a shows the full diffractograms. Fig. 6.4 b shows a zoom around the expected position of a peak from a Cr-rich phase, the counts are multiplied by a factor of 30 as compared to the full diffractograms.

All samples exhibit the main peaks of W allocated to the (110), (200), and (211) lattice planes, as given in table 6.1. Further, there is a K_β peak visible at 37°. This peak originates from the W (110) plane with K_β irradiation of the Cu-X-ray source. The K_β X-rays have a lower intensity and a different wavelength as compared to the main K_α X-rays. All peaks are shifted to higher angels as compared to peaks of pure W due to alloying with Cr. The lattice constant a can be calculated based on the peak position μ_{xyz} of each peak from lattice plane (xyz):

$$a_1 = \frac{\lambda}{\sqrt{2}\sin\left(\mu_{(110)}/2\right)};\ a_2 = \frac{\lambda}{\sin\left(\mu_{(200)}/2\right)};\ a_3 = \frac{\sqrt{6}\lambda}{2\sin\left(\mu_{(211)}/2\right)} \qquad (6.1)$$

The average a_{av} of a_1, a_2, and a_3 can be inserted into Vegard's approximation to calculate the atomic concentration c of Cr

$$c = 1 - \frac{a_{\mathrm{av}} - a_{\mathrm{Cr}}}{a_{\mathrm{W}} - a_{\mathrm{Cr}}} \qquad (6.2)$$

where a_i is the lattice constant of element i. The elemental concentration in wt. % follows from c and is plotted in Fig. 6.5. The error bars are based on the error on the average a_{av}, systematic errors from neglecting Y and from Vegard's approximation are excluded.
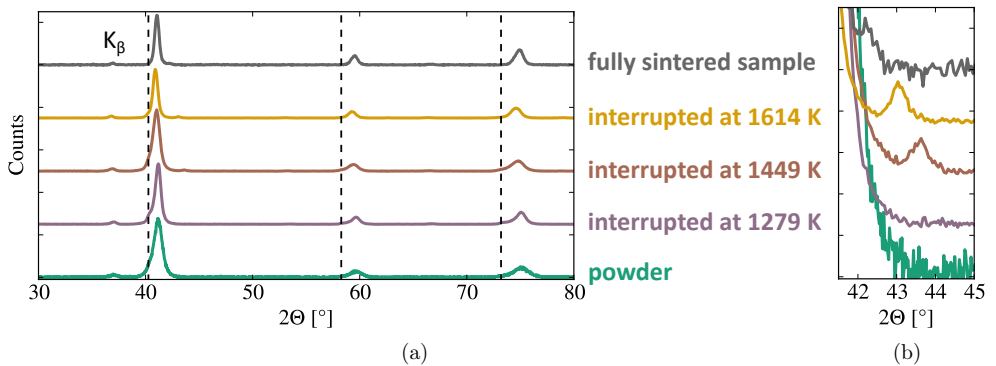
Figure 6.4: (**a**) XRD measurements of samples in different stages of the sintering process. The dashed lines indicate the expected peak-positions for W [81]. (**b**) Zoom of (a) around $2\Theta = 43°$.

An analogous calculation can be performed for the Cr-rich peaks shown in Fig. 6.4 b. In agreement with the SEM measurements shown in Fig. 6.3 no Cr-rich phase is detected in the powder and the sample interrupted at 1279 K. The samples interrupted at a sintering temperature of 1449 K, 1614 K, and the fully sintered sample have a Cr-rich peak corresponding to 53 wt. % Cr, 37 wt. % Cr, and 21 wt. % Cr, respectively. Thus, in agreement with the SEM results the Cr-rich phase forms at around 1400 K and decreases starting from around 1500 K due to the increased solubility of Cr in W. As Cr from the Cr-rich phase dissolves to the main phase, the Cr content in the main phase increases, as seen in Fig. 6.5.

Table 6.1: Results of Gaussian fits to the XRD peaks from the W lattice planes (110), (200), (211), and the Cr-rich phase shown in Fig. 6.4. μ is the mean and σ is the standard deviation of the Gaussian fit.

sample		(110)	(200)	(211)	Cr-rich
W [81]	μ [°]	40.27	58.28	73.20	-
powder	μ [°]	41.15	59.65	75.07	-
	σ [°]	0.44	0.57	0.71	
interrupted	μ [°]	41.15	59.61	75.03	-
at 1279 K	σ [°]	0.30	0.40	0.47	
interrupted	μ [°]	40.99	59.37	74.72	43.57
at 1449 K	σ [°]	0.36	0.50	0.63	0.27
interrupted	μ [°]	40.92	59.28	74.58	43.05
at 1614 K	σ [°]	0.25	0.37	0.48	0.19
fully sintered	μ [°]	41.06	59.51	74.89	42.19
sample	σ [°]	0.22	0.31	0.40	0.25
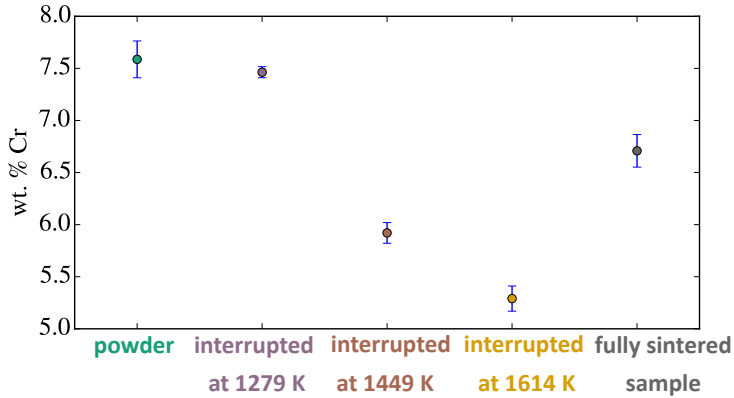
Figure 6.5: Calculated Cr content of the main phase of samples in different stages of the sintering process. The calculation is based on the fit results of the XRD peaks given in table 6.1 and Vegard's approximation.

These findings can be combined to an understanding of the sintering process:

1. The powder is mechanically alloyed at room temperature. A solid solution of all the alloying elements is achieved - no contrast in the SEM on the cross section is visible (see Fig. 6.3 a) and the XRD peak for the Cr-rich phase is absent. In the absence of Cr in any other state but the main phase, a systematic error in the calculation in Fig. 6.5 can be assumed. Most likely this systematic error is caused by Vegard's approximation and the calculated 7.6 wt. % Cr correspond to the real 11.4 wt. % Cr. A similar systematic error should be considered for all other data points in Fig. 6.5.

2. During sintering below 1300 K the powder particles are only pressed together. The width of the XRD peaks decreases as strains in the particles relax at elevated temperatures (see table 6.1).

3. During sintering at a temperature from 1300 K to 1450 K compacting continues, but phase separation occurs. The thermal energy is sufficient to drive the system towards the equilibrium state given by the phase diagram in Fig. 1.2 b. The Cr concentration in the main phase decreases as compared to the powder, see the evaluation of the XRD measurement in Fig. 6.5. The phase separation causes local variation in Cr concentration within each phase. Consequently, the XRD peaks broaden. It can be expected that the formation of the Cr-rich phase is more pronounced the longer the sample is in that temperature range during sintering.

4. During sintering at a temperature from 1450 K to 1614 K compacting continues, the agglomerates disassemble, and the grain structure forms. Y-containing nano-particles segregate. The equilibrium state in the phase diagram (see Fig. 1.2 b) is approached and the variation of the Cr content of different grains decreases causing a reduced width of the XRD peaks as compared to the previous step.

5. During sintering at a temperature above 1614 K compacting finalizes and the sample returns almost to a solid solution due to the elevated temperature. Based on the results in Fig. 6.5 and considering the systematic error discussed above, the Cr content in the main phase should be above 10 wt. % Cr. The variation in concentration of the different grains reduces as indicated by the reduced peak width in the XRD, see table 6.1. Longer holding time at around 1700 K or a higher sintering temperature is expected to cause grain growth.

Chapter 7

Influence of production parameters on the oxidation of bulk samples

7.1 Influence of the sintering parameters on oxidation

The fact, that the production of bulk alloys has multiple free parameters is already introduced in chapter 6. In this section the influence of the sintering parameters on the oxidation resistance is studied. A recommendation for the optimum sintering parameters is given at the end of the section. The pressure on the sample during sintering is fixed at 50 MPa for all experiments. A lower pressure is expected to yield less efficient compacting. A significantly higher pressure is not possible with the employed equipment - sintering at 70 MPa was attempted, but the graphite die broke during the process. The remaining parameters are the heating rate h, the maximum sintering temperature $T_{\max}$, and the holding time t_{hold} at $T_{\max}$. In the following these parameters are given in a tuple (h, $T_{\max}$, t_{hold}). Fig. 7.1 shows an overview of the investigated sintering parameters. Microstructure, density, and oxidation resistance of the W-11.4Cr-0.6Y alloys are compared.

The grain size of the samples is measured by graphical analysis based on the planimetric procedure [87]: a rectangular area containing more than 30, usually around 50 grains is selected on a SEM image. The size A of that area is measured and the number N of grains in the area is counted. Further, the number of pixels P falling onto the Y-Cr-O nano-particles (see section 9 for analysis of the nano-particles) are counted in the selected
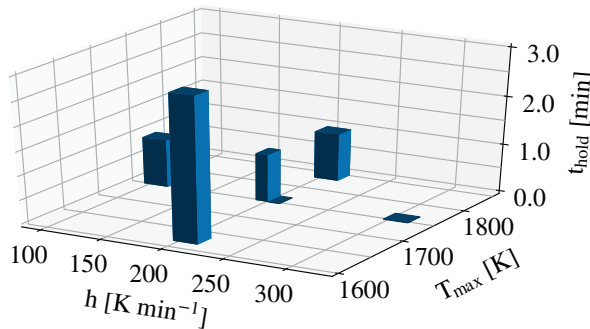
Figure 7.1:   Overview of the investigated sintering parameters: heating rate h, maximum sintering temperature T_{max}, and holding time t_{hold}.

area. The area of an individual pixel is given by A_p. Isotropy of the microstructure of the alloy is assumed. Then the average equivalent spherical diameter d [88] is calculated using the following formula:

$$d = \sqrt{\frac{6}{\pi} \times \frac{A - P \times A_p}{N}} \tag{7.1}$$

The grain size of the samples is specified by d. The error is obtained by repeating the procedure on different areas and calculating the error on the average of d.

The work for sample preparation was distributed in the following way: Tobias Wegener performed the mechanical alloying. He presented a detailed analysis of the grain size distribution in dependence of the sintering parameters by measuring a large number of grains individually [53]. Sintering was performed by Jesus Gonzales-Julian. The author of this thesis performed the grinding, the FIB cuts, the SEM imaging, the oxidation experiments, and the presented data evaluation.

Characterization of the samples with the sintering parameters as illustrated in Fig. 7.1 yields the following results:

- A cross section of the sample sintered at $(200 \, \text{K} \, \text{min}^{-1}, \, 1608 \, \text{K}, \, 3 \, \text{min})$ is shown in Fig. 7.2 a. A longer holding time at around $1600 \, \text{K}$ does not cause dissolution of the Cr-rich phase, as expected from the phase diagram shown in Fig. 1.2. Further, pores are visible and the relative density of the sample reaches only $(91.8 \pm 0.1) \, \%$, as measured using Archimedes principle. A higher sintering temperature yielding higher ductility of the sample seems to be required for full densification. Neither the Cr-rich phase nor the poor density are desired properties. Thus, the sample is not investigated further.

- A cross section of the sample sintered at $(200 \, \text{K} \, \text{min}^{-1}, \, 1740 \, \text{K}, \, 0 \, \text{min})$ is shown in Fig. 7.2 b. In chapter 6 it is already shown that these sintering parameters provide a fully dense sample. Graphical analysis of the image yields a small grain size of $(0.23 \pm 0.03) \, \mu\text{m}$. The Y-Cr-O nano-particles have a diameter of around $23 \, \text{nm}$. A measurement based on Archimedes principle (see section 2.8) yields a relative density of $99 \, \%$.

- A cross section of the sample sintered at $(200 \, \text{K} \, \text{min}^{-1}, \, 1740 \, \text{K}, \, 1 \, \text{min})$ is shown in Fig. 7.2 c. Graphical analysis of the image yields a medium grain size of $(0.33 \pm 0.03) \, \mu\text{m}$. The Y-Cr-O nano-particles at the grain boundaries have a diameter of around $26 \, \text{nm}$. Thus, a holding time of $1 \, \text{min}$ causes slow grain growth but no other significant changes to the microstructure. A measurement based on Archimedes principle yields a relative density of $99 \, \%$, no further compacting is achieved during the additional holding time as compared to the sample with the sintering parameters $(200 \, \text{K} \, \text{min}^{-1}, \, 1740 \, \text{K}, \, 0 \, \text{min})$.

- A cross section of the sample sintered at $(300 \, \text{K} \, \text{min}^{-1}, \, 1740 \, \text{K}, \, 0 \, \text{min})$ is shown in Fig. 7.2 d. Graphical analysis of the image yields a medium grain size of $(0.28 \pm 0.03) \, \mu\text{m}$. Y-Cr-O nano-particles with a diameter of around $34 \, \text{nm}$ are found at the grain boundaries. A measurement based on Archimedes principle yields a relative density of $99 \, \%$. Operation at $300 \, \text{K}$ is the upper limit of the machine, there is no significant impact on the grain size. Within the error bars the grain size is equal or slightly larger as compared to a heating rate of $200 \, \text{K} \, \text{min}^{-1}$. Such a high heating rate can cause local temperature variations and thus locally enhanced grain

growth. In the absence of benefits, the high heating rate of $300\,\mathrm{K\,min^{-1}}$ is discarded for sample production in favor of a higher stability of the process.

- A cross section of the sample sintered at $(100\,\mathrm{K\,min^{-1}},\ 1740\,\mathrm{K},\ 1\,\mathrm{min})$ is shown in Fig. 7.2 e. Graphical analysis of the full cross section yields a large grain size of $(1.0 \pm 0.1)\,\mathrm{\mu m}$. Y-containg particles with a diameter of around $0.1\,\mathrm{\mu m}$ are found. In chapter 6 it is shown that the grain structure forms during sintering between $1450\,\mathrm{K}$ and $1614\,\mathrm{K}$. Reducing the heating rate from $200\,\mathrm{K\,min^{-1}}$ to $100\,\mathrm{K\,min^{-1}}$ doubles the time in this temperature region. Longer time allows more time for ordering to form larger grains. A measurement based on Archimedes principle yields a relative density of $99\,\%$.

- A cross section of the sample sintered at $(200\,\mathrm{K\,min^{-1}},\ 1823\,\mathrm{K},\ 1\,\mathrm{min})$ is shown in Fig. 7.2 f. The horizontal lines are markings made using the FIB which are required for a different experiment. Graphical analysis of the full cross section yields a large grain size of $(1.0 \pm 0.1)\,\mathrm{\mu m}$. Y-containing particles with a diameter of around $0.1\,\mathrm{\mu m}$ are found at the grain boundaries. A measurement based on Archimedes principle yields a relative density of $99\,\%$. Grain formation and compacting is completed at the sintering temperature of $1740\,\mathrm{K}$, as discussed above. After that point only grain growth accelerated by an increased sintering temperature occurs. Thus, the grains are larger as compared to the sample with the sintering parameters $(200\,\mathrm{K\,min^{-1}},\ 1740\,\mathrm{K},\ 1\,\mathrm{min})$.

Based on the analysis of the cross sections, the oxidation behavior of the samples with the following sintering parameters is investigated: $(200\,\mathrm{K\,min^{-1}},\ 1740\,\mathrm{K},\ 0\,\mathrm{min})$, $(200\,\mathrm{K\,min^{-1}},\ 1740\,\mathrm{K},\ 1\,\mathrm{min})$, $(100\,\mathrm{K\,min^{-1}},\ 1740\,\mathrm{K},\ 1\,\mathrm{min})$, and $(200\,\mathrm{K\,min^{-1}},\ 1823\,\mathrm{K},\ 1\,\mathrm{min})$.

The oxide microstructure after oxidation for $44\,\mathrm{h}$ at a temperature of $1273\,\mathrm{K}$ in $20\,\mathrm{kPa}$ O_2 and $80\,\mathrm{kPa}$ Ar atmosphere is shown in Fig. 7.3 and 7.4. The sample with large grains $(100\,\mathrm{K\,min^{-1}},\ 1740\,\mathrm{K},\ 1\,\mathrm{min})$ is shown after oxidation in Fig. 7.3: there is a $0.5\,\mathrm{\mu m}$ thick layer of W-Y-O on the surface. Below there is a $0.3\,\mathrm{\mu m}$ thick layer of Cr_2O_3. Deeper inside, there is a $\sim 7\,\mathrm{\mu m}$ thick layer of porous W-Cr-O.

The sample with small grains $(200\,\mathrm{K\,min^{-1}},\ 1740\,\mathrm{K},\ 0\,\mathrm{min})$ is shown after oxidation in Fig. 7.4: there is a closed, protective Cr_2O_3 layer with a thickness of $(1.3 \pm 0.3)\,\mathrm{\mu m}$ on the surface. The variation in thickness of the oxide layer corresponds to the surface roughness R_a of $0.3\,\mathrm{\mu m}$ measured using the Dektak profiler. Further, there is internal oxidation, but no other oxide layers are detected. On the surface there are a few brighter spots visible. These are oxides containing W-17Y-18O and potentially also a few $\mathrm{wt.\,\%}$ of Cr as measured by EDX. An example is labeled in Fig. 7.4. An accurate determination of the Cr content in the W-Y oxide particles is not possible using EDX as the particles are small and embedded in Cr_2O_3.

Within the Cr_2O_3 layer there are small white particles with a diameter of around $20\,\mathrm{nm}$. They are identified as mainly W by EDX. The hypothesis of the author is that these particles diffuse outwards to form the aforementioned W-Y oxides on the surface. The surface coverage of the W-containing oxide is determined using EDX and ESB surface imaging. A surface coverage of around $4\,\%$ is found in the center of the sample, a more detailed analysis and discussion of the W-containing oxides follows in chapter 8.

(a) $(200\,\mathrm{K\,min^{-1}},\ 1608\,\mathrm{K},\ 3\,\mathrm{min})$ (b) $(200\,\mathrm{K\,min^{-1}},\ 1740\,\mathrm{K},\ 0\,\mathrm{min})$

(c) $(200\,\mathrm{K\,min^{-1}},\ 1740\,\mathrm{K},\ 1\,\mathrm{min})$ (d) $(300\,\mathrm{K\,min^{-1}},\ 1740\,\mathrm{K},\ 0\,\mathrm{min})$

(e) $(100\,\mathrm{K\,min^{-1}},\ 1740\,\mathrm{K},\ 1\,\mathrm{min})$ (f) $(200\,\mathrm{K\,min^{-1}},\ 1823\,\mathrm{K},\ 1\,\mathrm{min})$
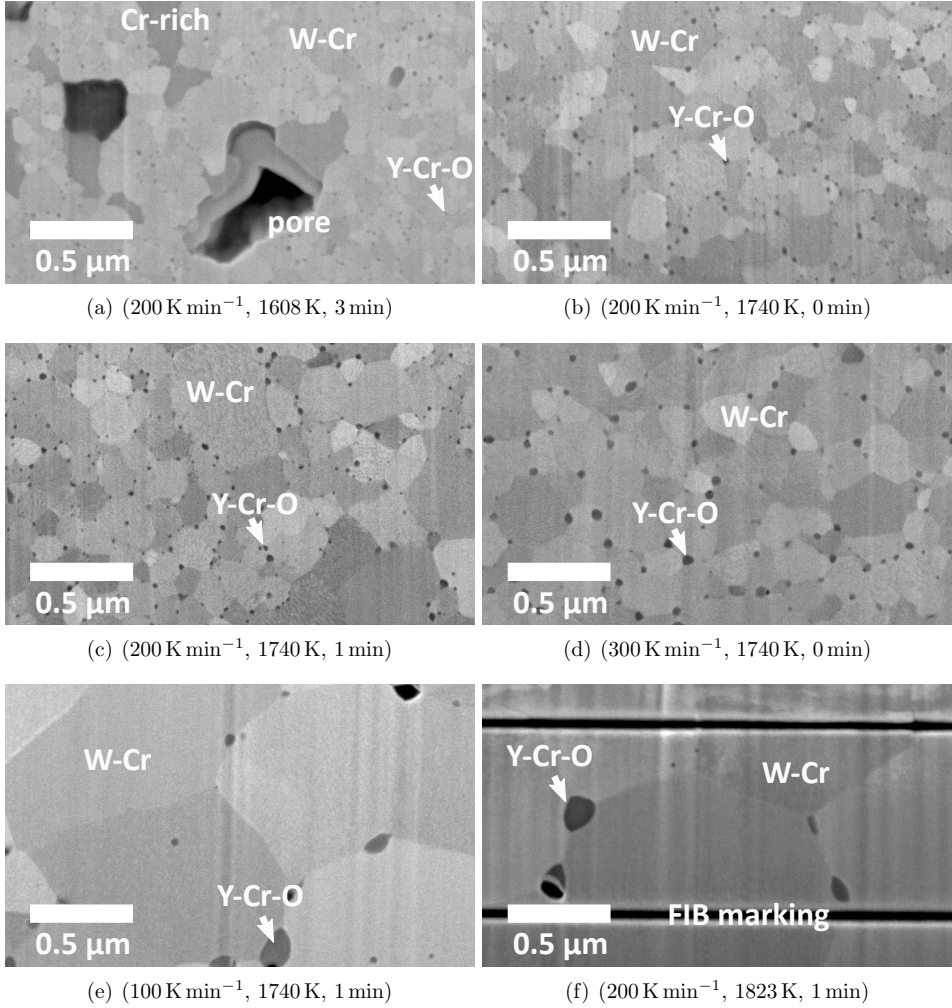
Figure 7.2: Electron microscopy images of cross sections on W-Cr-Y alloys showing the microstructure before oxidation for different the sintering parameters (heating rate, maximum sintering temperature, holding time).

The inset of Fig. 7.4 shows that the homogeneity of the protective oxide is not given at the edge of the sample. The adhesion of the oxide layer within $\sim 0.1\,\mathrm{mm}$ from the edge of the sample is weaker as compared to the center of the sample allowing the formation of W-containing oxides.

Analyzing the microstructure after oxidation and measuring the mass gain due to oxidation as a function of time are complementary methods to characterize the oxidation resistance of a material. The results of the mass gain due to oxidation at $1273\,\mathrm{K}$ in $20\,\mathrm{kPa}$ O_2 and $80\,\mathrm{kPa}$ Ar atmosphere are shown in Fig. 7.5. The sample with the smallest grains exhibits the lowest mass gain as expected due to the thinner oxide layers as shown in Fig. 7.3 and 7.4. The mass gain of samples with medium and large grains is higher.

In fact, the mass gain of the small-grain-sample is even lower as compared to the
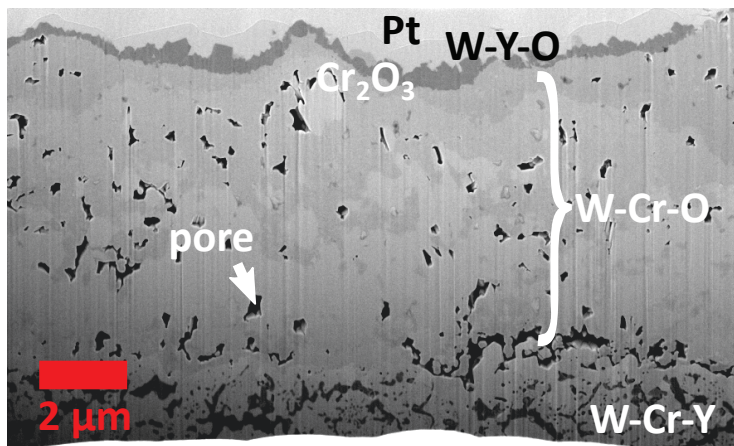
Figure 7.3: Cross section of the W-11.4Cr-0.6Y alloy ($100\,\mathrm{K\,min^{-1}}$, $1740\,\mathrm{K}$, $1\,\mathrm{min}$) after oxidation for $44\,\mathrm{h}$ at a temperature of $1273\,\mathrm{K}$ in $20\,\mathrm{kPa}$ O_2 and $80\,\mathrm{kPa}$ Ar atmosphere.
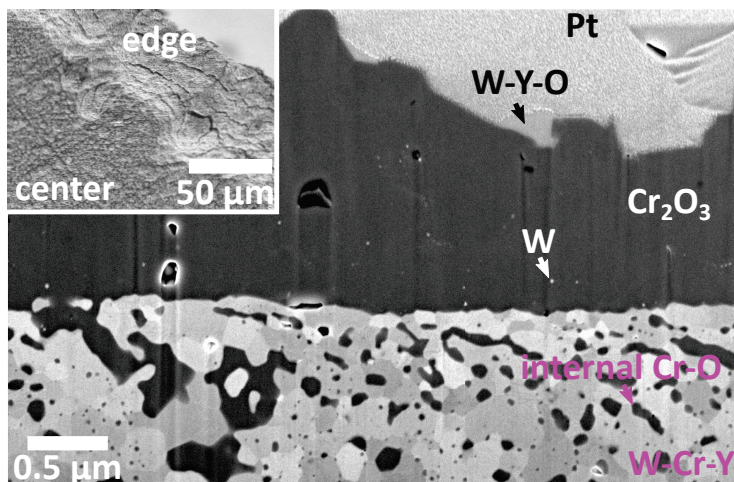
Figure 7.4: Cross section of the W-11.4Cr-0.6Y alloy ($200\,\mathrm{K\,min^{-1}}$, $1740\,\mathrm{K}$, $0\,\mathrm{min}$) after oxidation for $44\,\mathrm{h}$ at a temperature of $1273\,\mathrm{K}$ in $20\,\mathrm{kPa}$ O_2 and $80\,\mathrm{kPa}$ Ar atmosphere. A surface image is shown in the inset.

thin film sample discussed in chapter 5 and included as reference in Fig. 7.5. The main reason for the lower mass gain is the absence of the oxidation stage I discussed in section 5.2. This supports the hypothesis that oxidation stage I is a characteristic property of magnetron deposited thin films, see section 5.2.3.

The results in this section show that small grains increase the oxidation resistance. A W-11.4Cr-0.6Y alloy with a grain size of around $0.2\,\mu\mathrm{m}$ forms a protective Cr_2O_3 layer which is maintained for at least $44\,\mathrm{h}$ at $1273\,\mathrm{K}$. As estimated in section 9.1.2 and reported in literature, Cr diffuses mainly along the grain boundaries where the vacancy concentration is highest [34]. The number of grain boundaries per unit area decreases with increasing grain size, a quantitative estimation of this situation is provided in the

following paragraph. Thus, the Cr flux to the surface decreases with increasing grain size of the sample. If, at some point the Cr flux cannot replenish the protective oxide layer, Cr depletion below the protective oxide layer occurs, and W-containing oxides form below the protective oxide layer. The consequences of this behavior are observed in Fig. 7.3. WO_3 has a Pilling-Bedworth ratio of 3.4 [89] yielding a large volumetric expansion. The volumetric expansion of the oxides causes stresses, rupturing the thin protective Cr_2O_3 layer locally. The consequence is breakaway oxidation, as observed in Fig. 7.5. The porosity forms as cracks allow faster O_2 supply, causing locally faster oxidation [90]. As soon as a large amount of W oxides have formed, the continuous, protective Cr_2O_3 layer can no longer be maintained and the W oxides sublimate - the aim of full passive safety in case of a LOCA cannot be accomplished.

In conclusion, the optimum sintering parameters are ($200\,\mathrm{K\,min^{-1}}$, 1740 K, 0 min). These parameters minimize the time at elevated temperatures during sintering and thus creates a sample with small grains of around $0.2\,\mu$m. The small grains allow a sufficiently high Cr flux to replenish the protective Cr_2O_3 layer and provide full passive safety for at least 2 days. Longer oxidation times are tested in chapter 8.
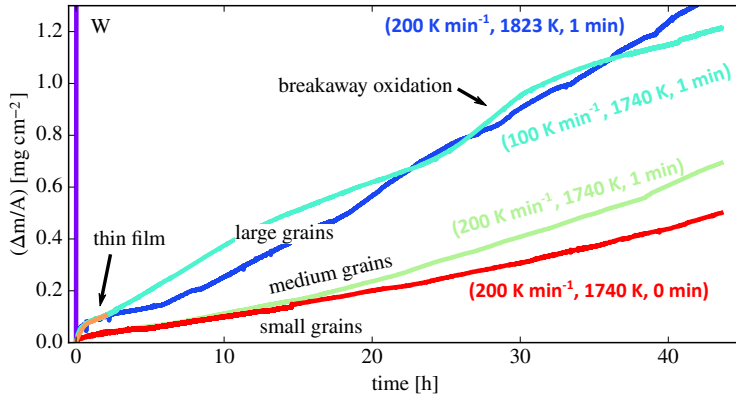
Figure 7.5:   Mass change of W-11.4Cr-0.6Y alloys and pure W as a function of time measured at a temperature of 1273 K in 20 kPa O_2 and 80 kPa Ar atmosphere. The thin film is produced by magnetron sputtering. Figure adapted from F. Klein et al. [91].

On grain boundary diffusion

In the previous section it is shown that small grains are crucial for the oxidation resistance. Here, a quantitative estimation of grain boundary and volume diffusion is provided. There is no data for a W-Cr-Y alloy available. However, there is data for Co in W at a temperature of 1100 K [92] which is used for this estimation: the volume diffusion coefficient is $D_V = 6.1 \times 10^{-24}\,\mathrm{m^2\,s^{-1}}$ and the grain boundary diffusion parameter is $P = 1.9 \times 10^{-25}\,\mathrm{m^3\,s^{-1}}$ [92]. A typical grain boundary thickness is 5 Å, thus the the grain boundary diffusion coefficient $D_{gb} = P/\delta = 3.8 \times 10^{-14}\,\mathrm{m^2\,s^{-1}}$.

The total area of grain boundaries A_{gb} in a sample with cubic grains normalized to a surface area $A_s = 1\,\mathrm{cm^2}$ is calculated as a function of the grain size: a grain size of 200 nm as found in this study yields $A_{gb}^{200\,\mathrm{nm}} = 5 \times 10^{-7}\,\mathrm{m^2}$; a grain size of 4 µm as found for W in [93] yields a smaller $A_{gb}^{4\,\mu\mathrm{m}} = 0.3 \times 10^{-7}\,\mathrm{m^2}$. The total flux Φ_{gb} through the

grain boundaries is proportional to $D_{gb} \times A_{gb}$, thus the flux through the grain boundaries increases with decreasing grain size.

The contribution of volume diffusion to the diffusion is estimated by

$$\frac{D_V \, A_s}{D_{gb} \, A_{gb}^{200\,\text{nm}}} \approx 10^{-8}. \tag{7.2}$$

Thus, the contribution of volume diffusion is negligible under the chosen conditions and smaller grains increase in the total diffusion flux of particles proportional to A_{gb}. However, the binary W-Cr alloy shown in Fig. 5.5 proves that a microstructure with small grains is not sufficient for the material to form a protective Cr_2O_3 layer. It is crucial to add Y. A detailed discussion on the effects of Y is presented in section 9.2.

7.2 Influence of the surface roughness on oxidation

The surface preparation of the bulk alloys after sintering is another free parameter for the oxidation resistance of bulk alloys. In this section the optimum sintering parameters ($200 \, \text{K} \, \text{min}^{-1}$, $1740 \, \text{K}$, $0 \, \text{min}$) discussed in the previous section are used for all W-11.4Cr-0.6Y alloys. Around 0.5 mm of material is removed from the surface in order to minimize the C contamination from sintering and to have a homogeneous microstructure [53]. Three samples are ground:

1. Grinding with P180-grade SiC abrasive paper yields a sample with a surface roughness $R_a = (0.6 \pm 0.1) \, \mu\text{m}$. In the following this sample is referred as 'rough sample'.

2. Grinding to a surface finish with P1200-grade SiC abrasive paper as described in section 2.4 yields a cubic samples with a surface roughness $R_a = (0.04 \pm 0.01) \, \mu\text{m}$. In the following this sample is referred as 'standard sample'. The W reference sample is also ground using this method.

3. Grinding of a standard sample is continued manually. Sharp edges are removed by holding the sample by hand onto P1200-grade SiC abrasive paper on a rotating disc of a planar grinding machine while slowly rotating the sample. However, a perfectly round shape is not achieved as seen in the photograph in table 7.1. In the following this sample is referred as 'round sample'.

The mass gain due to oxidation at $1273 \, \text{K}$ in $20 \, \text{kPa} \, \text{O}_2$ and $80 \, \text{kPa}$ Ar atmosphere as a function of time is shown in Fig. 7.6. The rough sample oxidizes almost twice as fast as the round sample which oxidizes almost four times faster than the standard sample. A summary of the results, including photographs of the samples before and after oxidation are given in table 7.1.

The total mass gain of a sample constitutes of four contributions: mass gain due to formation of the Cr_2O_3 layer, mass gain due to internal oxidation, mass gain due to
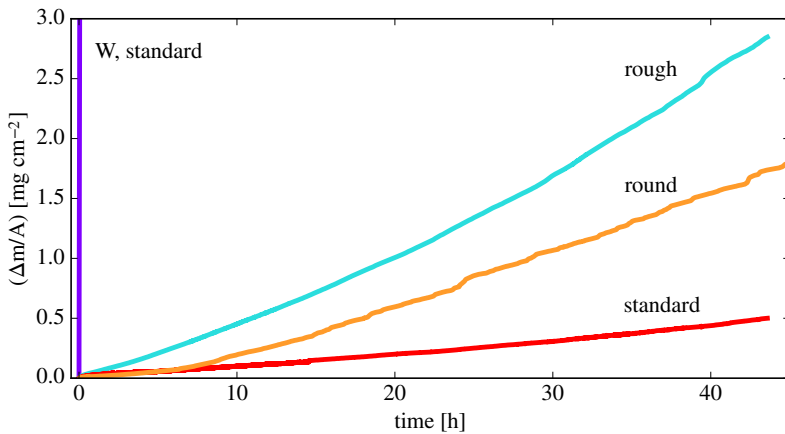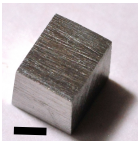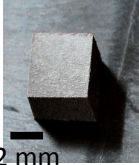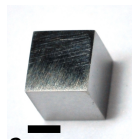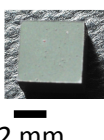
Figure 7.6: Mass change of W-11.4Cr-0.6Y alloys and pure W as a function of time at a temperature of $1273 \, \text{K}$ in $20 \, \text{kPa} \, \text{O}_2$ and $80 \, \text{kPa}$ Ar atmosphere. The surface finish of the alloys is different, else they are identical. Figure adapted from F. Klein et al. [91].

formation of W-containing oxides, and mass loss due to sublimation. The contributions are quantified in section 8.1 where also the reasons for a linear oxidation rate are discussed. As seen in Fig. 7.4, a protective Cr_2O_3 layer suppresses the formation of W-containing oxides. W-containing oxides form where the Cr_2O_3 layer fails - typically at damaged spots, discontinuities, or at the edge of the sample where the adhesion of the protective oxide layer is reduced.

The rough sample has many scratches from grinding on the surface. Each scratch is a damage of the surface, increasing the risk of failure of the protective Cr_2O_3 layer. Consequently more W-containing oxides form. The mass gain increases as compared to the standard sample, as seen in Fig. 7.6.

The round sample is ground hand-held. This yields many small discontinuities along the rounded corners instead of one discontinuity at each rectangular corner of the sample. The failure probability of the Cr_2O_3 increases at each discontinuity along the rounded corner as compared to the flat surface. The increased failure probability results in the higher mass gain seen in Fig. 7.6. A perfectly round sample is expected to have a reduced oxidation rate as compared to the standard, cubic sample as there is no edge at all. The hypothesis cannot be verified with the existing grinding methods. An alternative approach is to oxidize a larger sample reducing the fraction of the surface in the vicinity of the edge to the remaining surface. The standard, cubic sample has a side length of $\sim 4\,\mathrm{mm}$.

Table 7.1: Results of the oxidation experiments of W-11.4Cr-0.6Y alloys at $1273\,\mathrm{K}$ in $20\,\mathrm{kPa}$ O_2 and $80\,\mathrm{kPa}$ Ar atmosphere for different surface finish of the samples.

sample	roughness [µm]	shape	before oxidation	oxidation rate [mg cm^{-2} s^{-1}]	after oxidation
1. rough	0.6 ± 0.1	cubic	2 mm	1.8×10^{-5}	2 mm
2. standard	0.04 ± 0.01	cubic	2 mm	3.0×10^{-6}	2 mm
3. round	–	round	2 mm	1.2×10^{-5}	2 mm

7.3 Influence of the Y content on oxidation

The elemental optimization of smart alloys yielding to the composition W-11.4Cr-0.6Y was based on thin films [30]. This section addresses the question whether small changes in the Y content have beneficial effects on the oxidation resistance of bulk materials. For that purpose samples are sintered with the optimized sintering parameters ($200\,\mathrm{K\,min^{-1}}$, $1740\,\mathrm{K}$, $0\,\mathrm{min}$), as discussed in section 7.1, followed by grinding to a standard, cubic sample, as described in section 7.2. The elemental composition is W-11.4Cr-xY where the Y content x is varied. Four compositions containing $x = (0.3, 0.6, 1.0, 1.5)\,\mathrm{wt.\,\%}$ Y are oxidized at a temperature of $1273\,\mathrm{K}$ in $20\,\mathrm{kPa}$ O_2 and $80\,\mathrm{kPa}$ Ar atmosphere for $44\,\mathrm{h}$. The results are shown in Fig. 7.7 and 7.8.

Fig. 7.7 shows the mass change as a function of time at a temperature of $1273\,\mathrm{K}$ in $20\,\mathrm{kPa}$ O_2 and $80\,\mathrm{kPa}$ Ar atmosphere. The lowest mass gain, i.e. the best oxidation resistance is achieved by the W-11.4Cr-0.6Y alloys, which is the elemental composition already recommended in the studies based on thin films [30]. The measurement is repeated three times using samples which followed the same production route. The results confirm that an alloy with this composition has the best oxidation resistance. An average linear oxidation rate of $4 \times 10^{-6}\,\mathrm{mg\,cm^{-2}\,s^{-1}}$ is measured.

All other alloys show breakaway oxidation. As compared to the W-11.4Cr-0.6Y alloy, the average linear oxidation rate increased by a factor of 13, 6, and 8 for $0.3\,\mathrm{wt.\,\%}$ Y, $1.0\,\mathrm{wt.\,\%}$ Y, and $1.5\,\mathrm{wt.\,\%}$ Y, respectively. The linear oxidation rate of pure W is increased by a factor of 1600, as compared to W-11.4Cr-0.6Y. It is important to remark that these factors are based on linear oxidation rates, in literature often parabolic oxidation rates are approximated yielding to different factors of oxidation reduction. However, the measurements shown in Fig. 7.7 do not allow a parabolic approximation. The reasons why the total mass gain follows a linear rate law, not a parabolic rate law, are discussed in the following chapter 8.1.
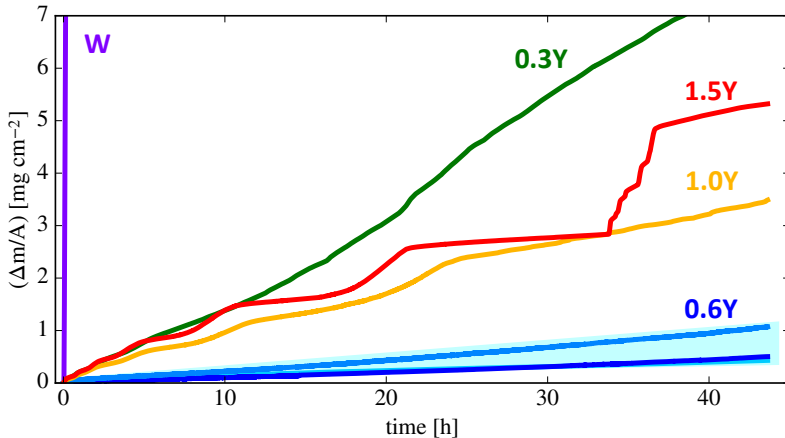
Figure 7.7: Mass change of W-11.4Cr-xY alloys and pure W as a function of time at a temperature of $1273\,\mathrm{K}$ in $20\,\mathrm{kPa}$ O_2 and $80\,\mathrm{kPa}$ Ar atmosphere. The yttrium content x is given in the labels.

Fig. 7.8 shows X-ray diffractograms after oxidation at a temperature of 1273 K in 20 kPa O_2 and 80 kPa Ar atmosphere for 44 h. The W-11.4Cr-0.6Y alloy is the only one where the metallic W alloy peaks remain visible. Thus, it has the thinnest oxide layer as expected due to the lowest mass gain shown in Fig. 7.7. Further, the XRD in Fig. 7.8 shows that the W-11.4Cr-0.6Y alloy is the only composition where clear Cr_2O_3 peaks are detected, while all peaks indicating W-containing oxides are missing. The sample has the desired properties: a protective Cr_2O_3 layer suppresses the formation of W-containing oxides, as shown in the cross section in Fig. 7.4.

All other compositions shown in Fig. 7.8 have peaks corresponding to W-containing oxides, mainly present in the form of Cr_2WO_6. These oxides offer less protection and cause the higher mass gain shown in Fig. 7.7. In conclusion, the fine adjustment to around 0.6 wt. % Y is crucial for the formation of a protective Cr_2O_3 layer with a good diffusion barrier for incoming oxygen and good adhesion to the alloy. The mechanisms how Y improves the oxidation resistance are addressed in section 9.2.
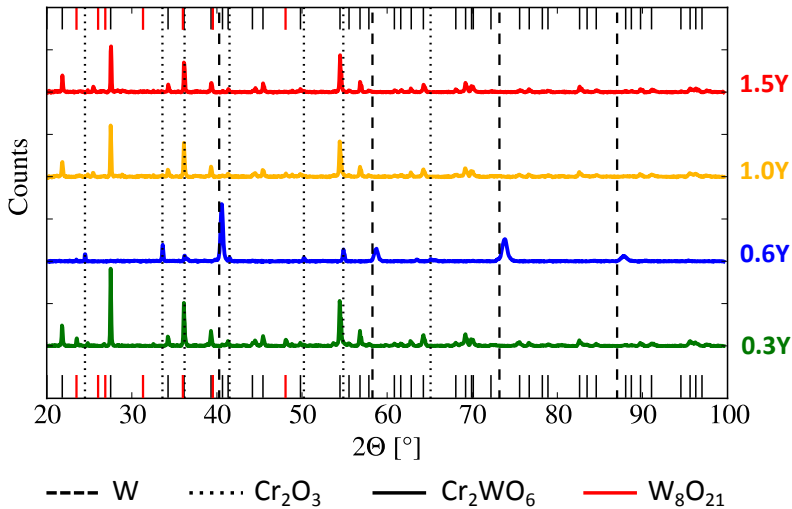
Figure 7.8: XRD measurements of W-11.4Cr-xY alloys after oxidation at 1273 K in 20 kPa O_2 and 80 kPa Ar atmosphere for 44 h. The yttrium content x is given in the labels. Peak positions for different compounds are marked. W, Cr_2O_3, Cr_2WO_6 and W_8O_{21} are based on [81, 94, 95, 96], respectively.

7.4 Summary of the analyzed influences on oxidation

The presented studies on different parameters influencing the oxidation of bulk W-Cr-Y alloys yields a recommendation for manufacturing oxidation resistant smart alloys:

1. Mix powder with the elemental composition W-11.4Cr-0.6Y. See section 7.3 for the optimization of the atomic composition.

2. Mechanically alloy the powder using a planetary ball mill for 60 h. The full parameters are listed in section 2.2. Detailed research on mechanical alloying of W-Cr-Y powders is found in [53].

3. Sinter the alloyed powder using FAST. Use a heating rate of $200\,\mathrm{K\,min^{-1}}$ to the maximum sintering temperature of 1740 K. There is no holding time at the highest temperature and a pressure of 50 MPa is applied during the whole process. See section 7.1 for the optimization of the sintering process.

4. Cut the sample removing at least 0.5 mm from the surface. Afterwards, grind the surface down to a surface finish of P1200-grade SiC abrasive paper resulting in a surface roughness of around 0.04 µm. The number of edges of the sample should be minimized for an optimum oxidation resistance. See section 7.2 for the optimization of the surface preparation.

Chapter 8

Long-term studies in dry and humid air

8.1 Oxidation and sublimation in dry air

The alloys analyzed in this chapter are manufactured according to the recommendations given in section 7. For the first time, an experiment duration of three week is addressed. Such a long-term study allows to study how the presence of a protective oxide layer changes the interaction processes of the different elements W, Cr, Y, and O. In addition to measuring the oxidation kinetics, the sublimation rates of the alloy during oxidation are measured. Measurement of the sublimation is crucial for estimates of the radioactive hazard.

Calibration of the sublimation measurement technique

Sublimation is measured using the catcher, as illustrated in Fig. 2.4 c. Calibration for the specific experimental conditions is conducted in order to determine the efficiency of the catcher. The specific experimental conditions are a flow of $10\,\mathrm{ml\,min^{-1}}$ of synthetic air at a temperature of $1273\,\mathrm{K}$. Synthetic air contains $80\,\%$ N_2 and $20\,\%$ O_2. Calibration is performed by conducting two separate experiments in the aforementioned conditions. The results are shown in Fig. 8.1.

- The mass change of a fully oxidized WO_3 film is measured, as discussed in section 3.2. The sublimation rate is $s_W = 6.7 \times 10^{-6}\,\mathrm{mg\,cm^{-2}\,s^{-1}}$.

- A piece of W is hung into the catcher, the W must not touch the catcher and is not connected to the balance. The W oxidizes and sublimates while the mass change of the catcher is measured and normalized to the area of the W sample. A fraction of the material sublimating from the sample deposits onto the catcher - the mass gain of the catcher is $r_c = 3.5 \times 10^{-6}\,\mathrm{mg\,cm^{-2}\,s^{-1}}$. For easier comparison to the mass loss of the thin film, the mass gain of the catcher is multiplied by (-1) in Fig. 8.1.

The efficiency η_d of the catcher is given by the fraction

$$\eta_d = \frac{r_c}{s_W} = 52\,\% \qquad (8.1)$$
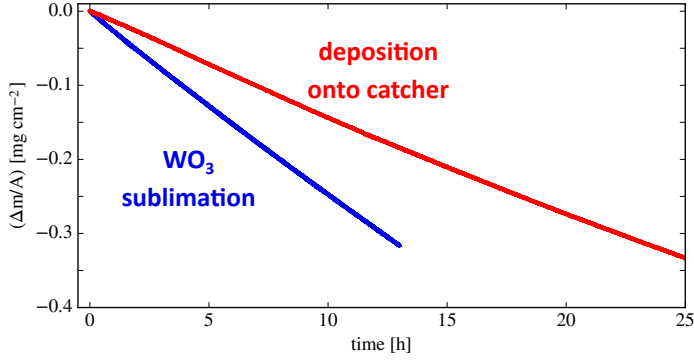
Figure 8.1: Calibration of the catcher for sublimation measurements at 1273 K in synthetic air. The mass loss of a fully oxidized thin film is plotted in blue. For the second measurement, plotted in red, W is hung into the catcher and the mass change of the catcher is measured. Mass gain of the catcher is plotted negative normalized to the surface area A of the W sample inside the catcher.

Oxidation and sublimation kinetics

The experiments are performed at the same conditions as the aforementioned calibration: dry, synthetic air at a temperature of 1273 K. Two smart alloy samples are cut from one sintering ingot: one is used to measure the oxidation kinetics, one is used to measure the sublimation kinetics. Each experiment lasts almost three weeks. The results are shown in Fig. 8.2. The upper part of the figure shows the total mass change of the sample normalized to the area of the sample. The total mass change is the sum of the contributions from sublimation and oxidation. The total mass change is split into three phases: the first phase of 180 h shows mass gain at a rate of $\sim 6 \times 10^{-6}\,\mathrm{mg\,cm^{-2}\,s^{-1}}$. The
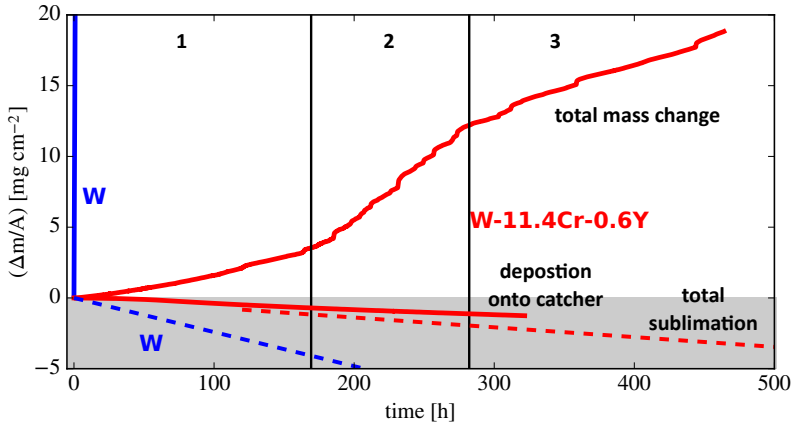
Figure 8.2: Mass change of a W-11.4Cr-0.6Y alloy and pure W as a function of time at 1273 K in synthetic air. The upper part shows the total mass change of the sample. The lower part shows the contribution of sublimation - the deposition onto the catcher and the calculated, total sublimation. Phases 1-3 are labeled.

second phase shows faster mass gain at a rate of $\sim 2.3 \times 10^{-5}\,\mathrm{mg\,cm^{-2}\,s^{-1}}$ for 100 h. In the third phase the mass gain reduces back to $\sim 1.0 \times 10^{-5}\,\mathrm{mg\,cm^{-2}\,s^{-1}}$. In comparison, pure W shows a much higher total mass gain of $\sim 6 \times 10^{-3}\,\mathrm{mg\,cm^{-2}\,s^{-1}}$.

The contribution from sublimation to the total mass change is shown in the lower part of Fig. 8.2. The solid line is the measured deposition of material onto the catcher. The sublimation is suppressed for about 50 h. After, a sublimation rate $s_{\mathrm{SA}} = 2 \times 10^{-6}\,\mathrm{mg\,cm^{-2}\,s^{-1}}$ of the smart alloy is calculated from the data and the efficiency η. The dashed line s_{W} indicates the sublimation rate of pure W extrapolated from Fig. 8.1. Next, the microstructure of the alloy after oxidation is shown. Afterwards, the knowledge on the microstructure is used to present a deeper understanding of the oxidation kinetics.

Material analysis after oxidation

Photographs of the alloys in different stages of the oxidation process are shown in Fig. 8.3. Fig. 8.3 a shows a standard, cubic sample before oxidation. The photographs of W and a smart alloy look identical before oxidation. Fig. 8.3 b shows a pure W after oxidation for 10 h. The formation of WO_3 with a Pilling-Bedworth ratio of 3.4 causes volumetric expansion and shape deformation. The W-11.4Cr-0.6Y alloys after oxidation for 44 h and 467 h are shown in Fig. 8.3 c,d, respectively. As already shown in the SEM image in Fig. 7.4, a slight buckling at the edge after 44 h is visible in the photo in Fig. 8.3 c. Overall, the cubic shape of the sample is preserved. After 467 h of oxidation the surface is porous, but the cubic shape of the sample is preserved.
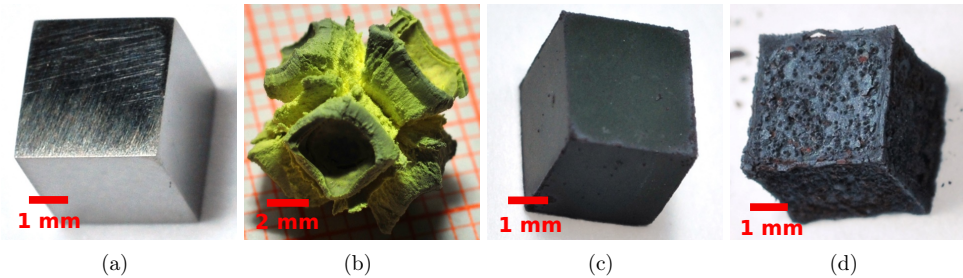
Figure 8.3: (**a**)W-11.4Cr-0.6Y alloy before oxidation after grinding. The pure W samples look the same. (**b**) Pure W sample after 10 h of oxidation in synthetic air at 1273 K. (**c**) W-11.4Cr-0.6Y alloy after 44 h of oxidation in synthetic air at 1273 K. (**d**) W-11.4Cr-0.6Y alloy after 467 h of oxidation in synthetic air at 1273 K. Figure adapted from F. Klein et al. [91].

Fig. 8.4 shows SEM images of the microstructure after 467 h of oxidation at 1273 K. The different crystals on the surface shown in Fig. 8.4 a are identified by EDX: there are $W_{26}Cr_{15}O_{59}$ crystals with a size of up to 5 µm and there are smooth shapes without sharp corners consisting of $W_{33}Y_{14}O_{54}$. The uncertainty of the elemental composition is a few % as the Y-enriched oxide particles are small and the electron-oxide interaction volume always contains the Y-enriched oxide and the surrounding Cr-enriched oxide. Further, the quantification of O relies on the K_α line at 0.525 keV. This line overlaps with the L_α line of Cr at 0.572 keV. Thus, an accurate determination of O in the presence of Cr is not possible using EDX.

Fig. 8.4 b shows a metallographic cross section imaged after embedding the sample in epoxy, removing 2 mm of material from one side, and polishing. A layered structure of different oxides is found, the composition of the oxides is measured using EDX. On the surface there is a layer containing different W-Cr-Y-O. This region is damaged during the preparation of the metallographic cross section.

Therefore, a FIB cut is performed, where the surface is protected using a Pt coating. The cross section in Fig. 8.4 c shows the oxides in the first micrometers near the surface. The oxides Cr-O, W-Y-O, and W-Cr-O are detected. The concentrations are measured using EDX and are given by the bars in the figure and in table 8.1. The uncertainty estimation is based on measurements of the cross section and the surface of a homogeneous reference material. The reason for the large uncertainty is the fact that the measurement is performed inside a cross section, where secondary scattering generates additional X-rays.

The oxides below the aforementioned W-Cr-Y-O on the surface are seen in the metallographic cross section in Fig. 8.4 b. There is a 20 µm thick layer of WO_3. Porosity is seen at the interface with the following Cr_2WO_6 layer, which has a thickness of 31 µm. The last layer before the metal is a 31 µm thick WO_3 layer. Further, Cr causes internal oxidation within the first ~ 10 µm of the metal.

Fig. 8.4 d shows a magnification of the upper WO_3 layer, which is labeled (d) in Fig. 8.4 b. W-17Y-18O and W-23O (corresponding to WO_3) grains with a size of 0.8 µm are seen.

Table 8.1: Elemental concentrations of the different oxides marked in Fig. 8.4 c.

	W [at. %]	**Cr** [at. %]	**Y** [at. %]	**O** [at. %]
1	33 ± 5	7 ± 5	14 ± 5	47 ± 5
2	26 ± 5	15 ± 5	–	59 ± 5
3	3 ± 5	22 ± 5	–	75 ± 5
4	37 ± 5	11 ± 5	–	52 ± 5
5	46 ± 5	5 ± 5	–	49 ± 5
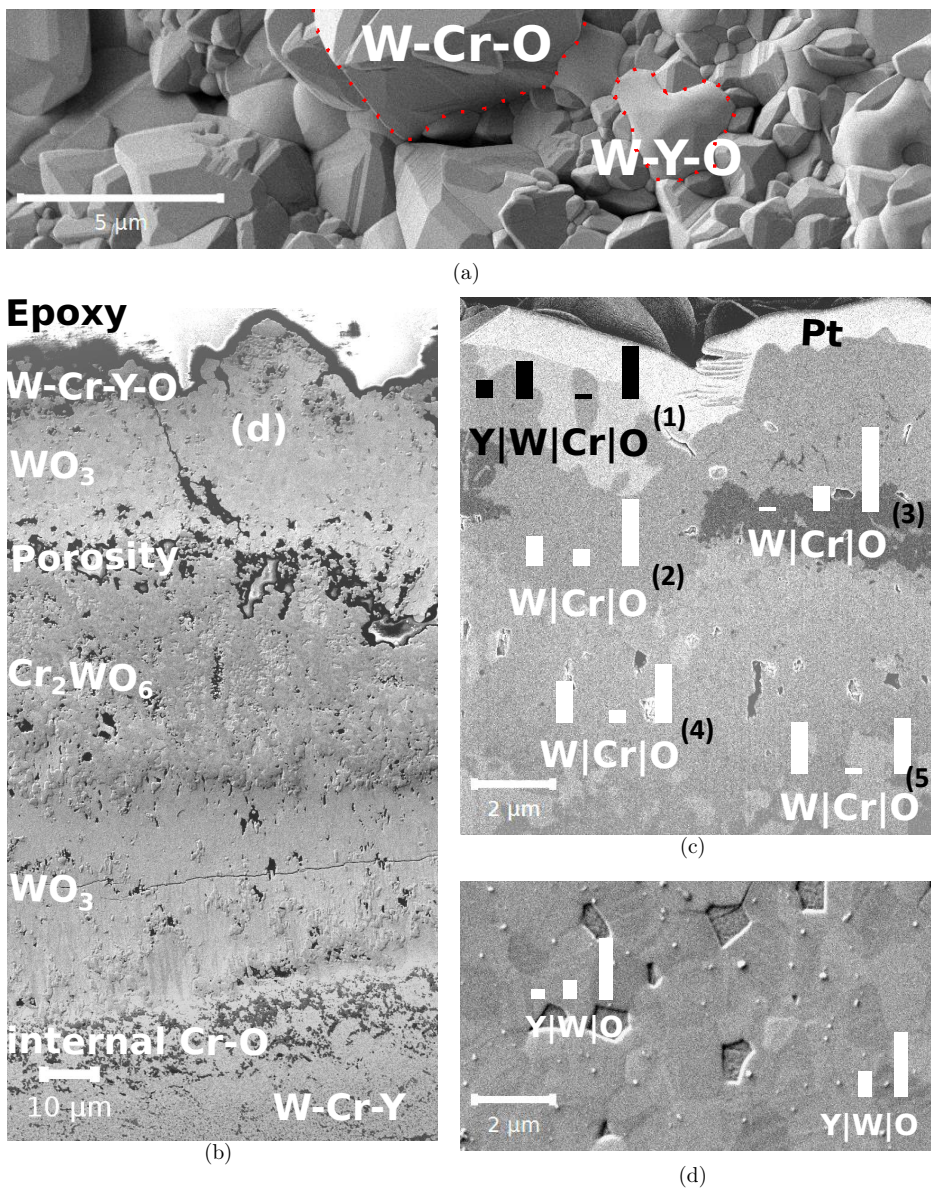
Figure 8.4: The oxide scale of an W-11.4Cr-0.6Y alloy after oxidation for 467 h at 1273 K in synthetic air is imaged by SEM. EDX results of the concentration in atomic % are given by the bars on top of the elements. (a) shows a surface image. (b) shows a cross section of the full oxide scale where the location of image (d) is marked as (d). The top 10 μm of the sample are shown in the FIB cut in (c). Figure adapted from F. Klein et al. [91].

Understanding of the oxidation behavior

The following considerations address the mechanisms of the observed degradation of the protective Cr_2O_3 layer seen in Fig. 8.4 as compared to Fig. 7.4 and 8.5. In fact the Cr_2O_3 layer after 467 h is thinner as compared to the Cr_2O_3 layer after 44 h, as seen in Fig. 8.4 c and 8.5. The Cr supply to the Cr_2O_3 layer is cut once thick layers of W oxides are formed. The oxidation time of 467 h is sufficiently long to form oxides according to the phase diagram [27]: the initially formed Cr_2O_3 reacts with W oxides to form Cr_2WO_6. Y is enriched in the phase similar to W-14Y-20.8O. According to the phase diagram [97], this phase has a melting temperature of 1427 K, the lowest melting point of any W-Y oxide. Thus, the temperature during oxidation is at around 90 % of the melting point of the W-14Y-20.8O phase and it has a molten-like shape on the surface of the sample, see Fig. 8.4 a.

The total mass gain of the alloy shown in Fig. 8.2 is divided into four contributions Δm_i, $i = 1, 2, 3, 4$:

1. Δm_1 is the mass gain due to the formation of a protective Cr_2O_3 layer. The formation of a protective Cr_2O_3 layer requires diffusion of Cr to the surface [40], a dedicated study on the diffusion of Cr is shown in chapter 9. Diffusion processes are described by Fick's first law. Thus, Δm_1 must follow a parabolic rate law:

$$\Delta m_1/A = \sqrt{c_1 \times t} \qquad (8.2)$$

   where A is the surface area of the sample, t the oxidation time, and c_1 a constant. A 1.3 μm thick Cr_2O_3 layer is detected after 44 h, see Fig. 8.5. Assuming a density of $\rho = 5.2\,\mathrm{g\,cm^{-3}}$ for Cr_2O_3, $\Delta m_1/A$ is calculated. Thus, $c_1 = 6 \times 10^{-7}\,\mathrm{mg^2\,cm^{-4}\,s^{-1}}$ in equation 8.2 is obtained.

2. Δm_2 is the mass gain due to formation of internal Cr_2O_3. This formation requires diffusion of O through the oxides into the metal. Diffusion processes are described by Fick's first law. Therefore, Δm_2 must follow a parabolic rate law:

$$\Delta m_2/A = \sqrt{c_2 \times t} \qquad (8.3)$$

   where c_2 is a constant. Internal oxides have a darker color on the cross section as compared to the W matrix, see Fig. 8.5. Counting the pixels with darker color on the the cross section yields the image coverage with internal oxidation after 44 h of oxidation. The total volume of internal Cr_2O_3 is calculated assuming isotropy of the internal oxides. The mass increase Δm_2 is calculated from the volume and yields $c_2 = 9 \times 10^{-8}\,\mathrm{mg^2\,cm^{-4}\,s^{-1}}$ in equation 8.3.

3. Δm_3 is the mass gain due to the formation of W-containing oxides. Similar to pure WO_3 as discussed in section 3.1.1, W-containing oxides are assumed to not act as a diffusion barrier for incoming oxygen. Thus, Δm_3 follows a linear rate law

$$\Delta m_3 = c_3 \times t \times A'(t) \qquad (8.4)$$

   where c_3 is a constant and A' is the area covered by W-containing oxides. W-containing oxides form where the protective oxide layer fails. The protective oxide fails with a certain probability p. Thus, A' is given by

$$A'(t) = A \times p. \qquad (8.5)$$

79

$A' \leq A$ must be valid for all times as W oxides cannot cover more than the entire surface. Failure spots during the first 180 h accumulate and yield the formation of W-containing oxides on the entire surface degrading the protective Cr_2O_3 layer due to volumetric expansion. This degradation causes the abrupt change in the oxidation rate observed in the second phase of the mass gain kinetics shown in Fig. 8.2. In other words, the boundary condition $A'(t > 180\,\text{h}) = A$ applies. In a linear approximation, the failure probability p is given with this condition:

$$\Rightarrow p = \begin{cases} \frac{1}{180\,\text{h}} \times t\,, & t < 180\,\text{h} \\ 1\,, & t > 180\,\text{h} \end{cases} \tag{8.6}$$

c_3 remains a free parameter for a fit to the data shown in Fig. 8.2.

4. Δm_4 is the mass loss due to sublimation. In chapter 4 it is shown that sublimation of Cr-oxide is negligible under the present conditions of 1273 K in dry synthetic air. Thus, the sublimation of W-containing oxides remains. The rate s_{SA} yields

$$\Delta m_4 = s_{\text{SA}} \times t \times A'(t) \tag{8.7}$$

In Fig. 8.2 a constant mass change of the catcher is measured after 180 h when $A' = A$. This result yields the sublimation rate $s_{\text{SA}} = -2 \times 10^{-6}\,\text{mg cm}^{-2}\,\text{s}^{-1}$.

The formation of the Cr-rich phase visible in Fig. 8.5 does not cause mass change. The role on the oxidation kinetics is investigated in a dedicated experiment shown in chapter 9. The understanding of this model leaves two free parameters for describing the total mass gain as shown in Fig. 8.2: the constant c_3 and an offset attributing the accelerated mass gain in the second phase of the oxidation process. Fitting according to the equation

$$\Delta m = \sum_i \Delta m_i \tag{8.8}$$

yields $c_3 = 6 \times 10^{-6}\,\text{mg cm}^{-2}\,\text{s}^{-1}$ and an offset of $4\,\text{mg cm}^{-2}$. Fig. 8.6 shows a comparison of the calculated results and the experimental data, agreement in found.
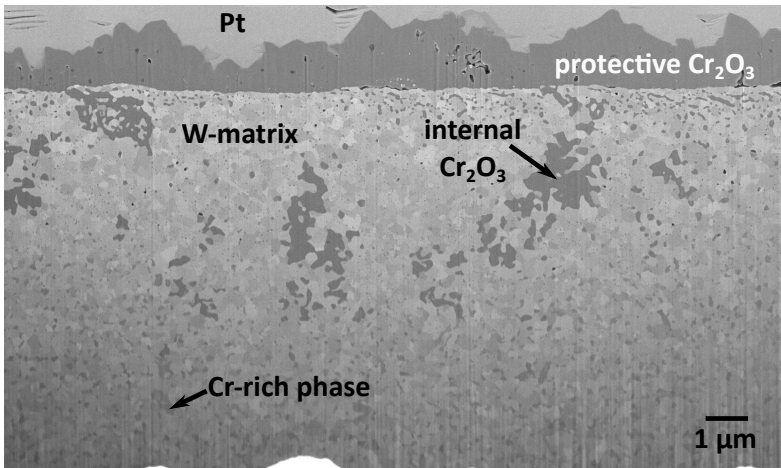
Figure 8.5: Cross section of the W-11.4Cr-0.6Y alloy after oxidation at 1273 K for 44 h.
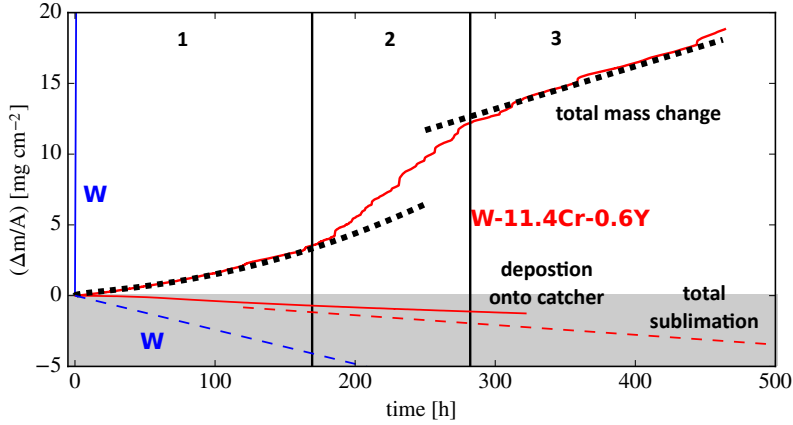
Figure 8.6: Mass change of a W-11.4Cr-0.6Y alloy and pure W as a function of time at 1273 K in synthetic air. The upper part shows the total mass change of the sample. The lower part shows the contribution of sublimation - the deposition onto the catcher and the calculated, total sublimation. Phases 1-3 are labeled. Solid lines are based on measurement data, dotted lines on calculations, and dashed lines on interpolations/calibrations.

This model does not describe the second phase of the oxidation process as labeled in Fig. 8.2/8.6. The second phase is the transition from a protective Cr_2O_3 layer to thick layers of W-Cr-Y oxides reducing the oxidation rate as compared to pure W. The hypothesis is that there builds up a slight Cr depletion under the protective oxide layer during the first phase. The oxidation rate is accelerated until this Cr depletion is compensated in the third phase of the oxidation kinetics shown in Fig. 8.2.

On the sublimation

The sublimation of material from the smart alloy is given by equation 8.7. Within the first two days the sublimation rate is very small, afterwards the sublimation rate s_{SA} is measurable. s_{SA} allows the estimation of the radiological hazard in case of a LOCA: the fraction of sublimated material depositing elsewhere in the reactor depends on the specific conditions in the power plant and on the accident. In the worst case, all material that sublimates is also released into the environment. Thus, the potential release of W from a reactor having a W-Cr-Y first wall armor with surface area of $1000\,m^2$ is 41 kg/month. The activity of this amount of material would be around 4×10^{16} Bq. Depite the degradation of the protective Cr_2O_3 layer, this release is a major improvement as compared to a pure W wall where 140 kg/month corresponding to 12×10^{16} Bq would be released under the same conditions - dry air at 1273 K. In comparison the total release due to the nuclear accident in Fukushima was 52×10^{16} Bq, excluding noble gases [20].

The key findings of this section are summarized as follows:

- The mass change of the sample is divided into four contributions which are quantified individually.

- Smart alloys cannot fully suppress sublimation and radioactive contamination of the environment in case of a LOCA. However, the consequences are significantly mitigated. Firstly, smart alloys provide a time of around 2 days after the accident before oxide sublimation starts at the low rate of $s_{\mathrm{SA}} = -2 \times 10^{-6}\,\mathrm{mg\,cm^{-2}\,s^{-1}}$.

- Unlike in the case of W the wall is not mechanically destroyed and one could potentially imagine to restart cooling - cooling would cause sublimation to drop due to a lower temperature.

8.2 Oxidation and sublimation at 1273 K in humid air

All experiments on oxidation of W-Cr-Y alloys presented in the previous sections are performed in dry atmosphere. However, the air from the environment and water from a cooling system are potential sources of humidity in case of a LOCA. Thus, the presence of humidity, which introduces H as additional reaction partner, must be considered. In chapters 3 and 4 it is already shown that humidity influences the oxidation and sublimation of W and Cr individually: humidity increases the sublimation rate at a constant temperature and thus increases the radiological hazard. Wegener et al. [83] published the first study on the effects of humidity on the oxidation behavior of W-Cr-Y alloys. However, the study was based on thin films allowing only short exposure times, as discussed in chapter 5.

The oxidation of the alloys in this section is performed at atmospheric pressure in synthetic air with a relative humidity level of 70 % at 313 K corresponding to 5 vol. % humidity. In the following these conditions are referred as humid air. The temperature is set to 1273 K, a duration of 10 days is investigated. Elemental composition, sintering parameters, and grinding steps are chosen according to the optimization presented in chapter 7: W-11.4Cr-0.6Y is sintered at a pressure of 50 MPa and a heating rate of $200\,\mathrm{K\,min^{-1}}$ to the maximum sintering temperature of 1740 K which is held for 0 s to 30 s. It was shown that such a small difference in the holding time does not change the oxidation resistance [53]. Therefore, samples with both holding times are selected to have a better availability of samples. Cubic samples with a surface finish using P1200-grade SiC grinding paper are prepared.

Calibration of the sublimation measurement technique

Oxidation and sublimation measurements are performed using the thermogravimetric analyzer, as described in section 2.16. Sublimation is measured by detecting the mass change of the catcher, as illustrated in Fig. 2.4 c. Due to a different atmosphere as compared to the calibration in chapter 8.1, the calibration of the catcher is repeated for the specific experimental conditions. In chapter 4 it is shown that in humid air not only WO_3 sublimates, but also Cr_2O_3 volatilizes. Thus, separate calibrations are performed for W and Cr: the results are shown in Fig. 8.7. Measurement of the mass change of fully oxidized thin films yields sublimation rates of $s_W = 1.4 \times 10^{-4}\,\mathrm{mg\,cm^{-2}\,s^{-1}}$ and $s_{Cr} = 2 \times 10^{-6}\,\mathrm{mg\,cm^{-2}\,s^{-1}}$ for W oxide and Cr oxide, respectively. These rates are compared to the deposition rates of material onto the catcher s_i^c when a sample i is hung into the catcher at 1273 K in humid air: $s_W^c = 6 \times 10^{-5}\,\mathrm{mg\,cm^{-2}\,s^{-1}}$ and $s_{Cr}^c = -3 \times 10^{-8}\,\mathrm{mg\,cm^{-2}\,s^{-1}}$ are measured for W and Cr, respectively. s_{Cr}^c is within the measurement uncertainty of the device, thus $s_{Cr}^c \approx 0\,\mathrm{mg\,cm^{-2}\,s^{-1}}$. The efficiencies η_h^i of the catcher detecting W and Cr sublimation in humid air are given by

$$\eta_h^W = \frac{s_W^c}{s_W} = 43\,\% \text{ and } \eta_h^{Cr} = \frac{s_{Cr}^c}{s_{Cr}} = 0\,\% \tag{8.9}$$

Thus, around half of the sublimating tungsten oxide deposits onto the catcher whereas the deposition of chromium oxides is below the detection limit.
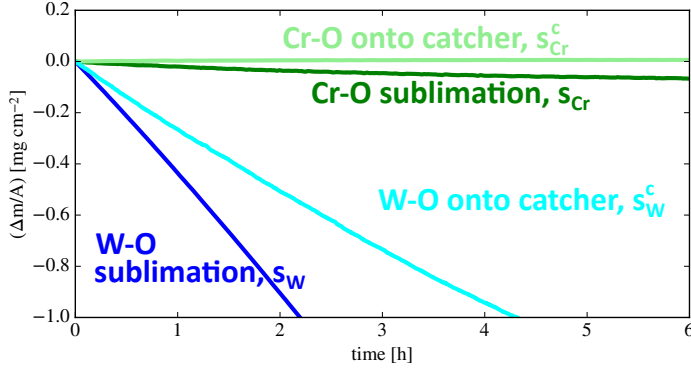
Figure 8.7: Calibration of the catcher for sublimation measurements at $1273\,\mathrm{K}$ in humid air. The sublimation rate of element i measured by the mass loss of a fully oxidized thin film is given as s_i. The mass gain of the catcher due to deposition of sublimated material from the sample i is multiplied by (-1) and plotted as s_i^c. Figure adapted from F. Klein et al. [98].

Material analysis after oxidation in humid air

A W-11.4Cr-0.6Y alloy is oxidized in humid air for 10 days at $1273\,\mathrm{K}$. The surface of the sample after oxidation is analyzed using EDX and XRD: the EDX spectrum is shown in Fig. 8.8 a. A composition of $37\,\mathrm{at.\,\%}$ Cr, $62\,\mathrm{at.\,\%}$ O, and $0.3\,\mathrm{at.\,\%}$ W is found. The XRD measurement is shown in Fig. 8.8 b. The peak positions and heights correspond to the expected peaks for Cr_2O_3 according to [94]. No other peaks are found. The concentration of $0.3\,\mathrm{at.\,\%}$ W detected in the EDX is too low to give rise to a clear XRD peak corresponding to a W-containing oxide. Both measurements agree that there is a Cr_2O_3 layer on the surface of the sample. An overview SEM image of the surface is shown in Fig. 8.9 a: there are two regions. One region is labeled 'thick', a lamella-like structure is observed indicating that multiple layers are stacked above each other. The other region is labeled 'thin', the surface appears rather smooth. The FIB-cut performed in the 'thin' region is visible in the overview image in Fig. 8.9 a.

FIB-cuts are performed in both regions. The cross section in the 'thin' region is shown in Fig. 8.9 b. A closed protective oxide layer with a thickness of $\sim 2.8\,\mathrm{\mu m}$ is found on the surface on top of the metal. Internal oxidation is detected within the first $12\,\mathrm{\mu m}$ of the metal. The cross section in the 'thick' region is shown in Fig. 8.9 c. The protective oxide layer is more than $20\,\mathrm{\mu m}$ thick, which is the depth of the crater. Pores are detected within the protective oxide layer. The shape of the pores coincides with the lamella-like structure seen on the surface in Fig. 8.9 a. Further, there are brighter spots within the Cr_2O_3 which are identified as W-32.2Cr-11.8Y-10.8O using EDX at an energy of $10\,\mathrm{keV}$. The information depth of EDX at $10\,\mathrm{keV}$ on WO_3 is around $0.5\,\mathrm{\mu m}$. Thus, a significant fraction of the Cr-K_α radiation originates from Cr outside the white spot. Graphical contrast analysis of Fig. 8.9 c yields that around $5\,\%$ of the cross section is covered with this W-containing oxide. However, the W-containing oxide is trapped within the Cr_2O_3 layer and cannot be released to the environment. Trapped W-containing oxides are no radiological hazard.

In contrast, the W-containing oxides on the surface may sublimate and thus pose a radiological hazard. Contrast between W-containing oxides and Cr_2O_3 on the non-
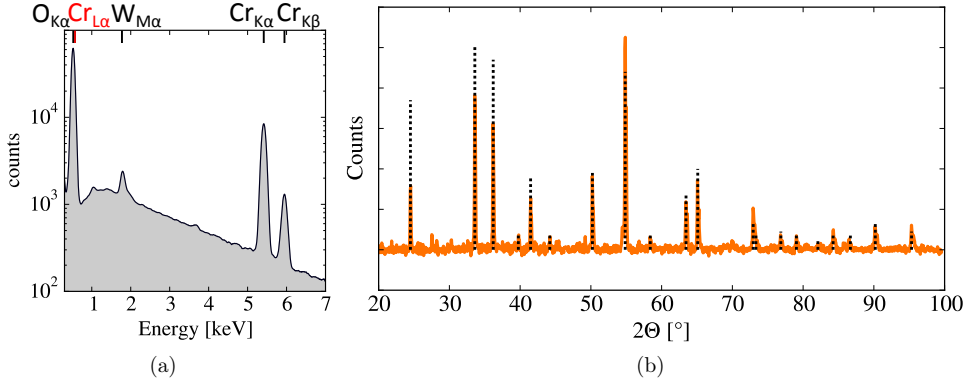
Figure 8.8: Surface characterization of the W-11.4Cr-0.6Y alloy after oxidation for 10 days in humid air by (**a**) EDX and (**b**) XRD. The vertical dotted lines represent the expected peak positions and intensities for Cr_2O_3 [94].

polished oxide surface is obtained by imaging using the ESB detector, see section 2.14 for more details on the ESB detector. Fig. 8.9 d shows an exemplary ESB image. Seven ESB images are taken on randomly selected spots on the surface of the sample. Graphical analysis by counting the dark and the bright pixels of the images yields an average surface coverage of $(1.0 \pm 0.8)\%$ with W-containing oxides. EDX at 10 keV identifies them as W-32Cr-9Y-23O $\approx 8\,(WO_2) \cdot 2\,(Y_2O_3) \cdot 13\,(Cr_2O_3)$. This is a similar composition as compared to the bright spots on the cross section shown in Fig. 8.9 c. Cr signal originates again from Cr_2O_3 in close vicinity of the W-containing oxide.

Despite samples following the same production route, this is a much better suppression of W oxide formation as compared to the studies in dry air presented in section 8.1. The key difference of the experiments is the presence of water in the atmosphere. In the presence of water, oxidation is mainly caused by the dissociation of water [75]. The Gibbs free energy of the reaction of H_2 and O_2 to H_2O is $-353\,kJ\,mol^{-1}$ at 1273 K whereas the Gibbs free energy of the reaction of Cr and O_2 to Cr_2O_3 is $-530\,kJ\,mol^{-1}$ [79], thus the Gibbs free energy of the reaction to Cr_2O_3 is more negative than the Gibbs free energy of the reaction to H_2O: water reacts with Cr leaving free H. This reaction continues as long as there is a sufficient supply of Cr. If an excess concentration of oxygen occurs due to a lack of Cr supply, there are two options: the free O can either react with W or H. The Gibbs free energy of the reaction of W and O_2 to WO_3 $-347\,kJ\,mol^{-1}$ is less negative than the Gibbs free energy of the reaction to water [79]. Thus, free O reacts with the available H first. WO_3 only forms if both Cr and H are depleted. Therefore, H acts a buffer suppressing the formation of W-containing oxides until more Cr has diffused to the surface and participates in forming the protective Cr_2O_3 layer [98].

A first estimation of the sublimation rate is possible: the sublimation rates of Cr_2O_3 $s_{Cr} = 2 \times 10^{-6}\,mg\,cm^{-2}\,s^{-1}$ and WO_3 $s_W = 1.4 \times 10^{-4}\,mg\,cm^{-2}\,s^{-1}$ are given from the measurement shown in Fig. 8.7. An approximation assumes that WO_3 sublimates at the same rate as the mixed W-containing oxide. The surface coverage of the oxide is 1% W-containing oxides and 99% Cr_2O_3, as shown in Fig. 8.9 d. Thus the total sublimation rate s is calculated to

$$s = 0.99 s_{Cr} + 0.01 s_W = 3 \times 10^{-6}\,mg\,cm^{-2}\,s^{-1}. \tag{8.10}$$
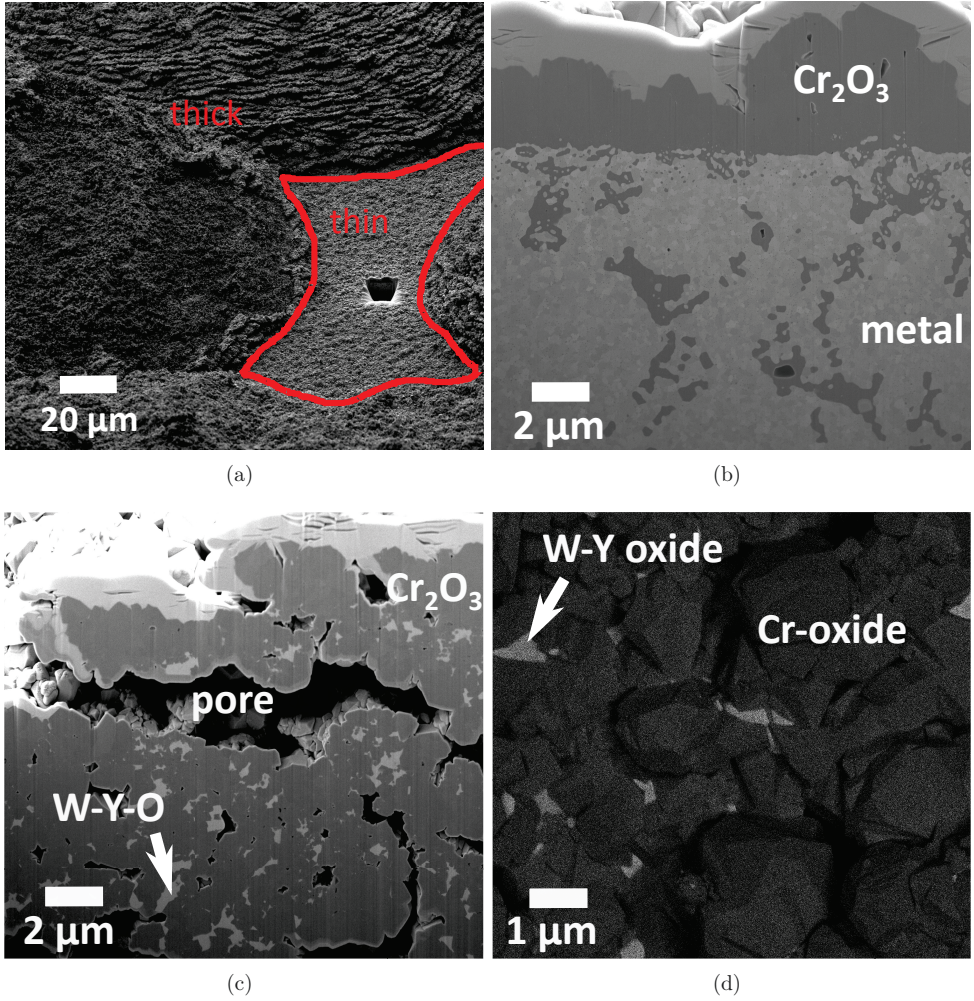
Figure 8.9: SEM images of the W-11.4Cr-0.6Y alloy after oxidation for 10 days at 1273 K in humid air. (**a**) overview of the surface, the region 'thin' and 'thick' are labeled. (**b**) a cross section in the thin region. (**c**) cross section in the thick region. (**d**) ESB image with a grid voltage of 1 kV resolving both W-Y oxide and Cr oxide, the W-Y oxides have a lighter color in the image. The ESB image is representative for both regions 'thin' and 'thick'. Figure adapted from F. Klein et al. [98].

Oxidation and sublimation kinetics

Measuring the mass change of the catcher, while the alloy inside the catcher is oxidizing and sublimating, is another method to determine the sublimation rate. The results of the sublimation measurement as well as the total mass change of the sample are shown in Fig. 8.10. A measurement on oxidation and sublimation of pure W is included for comparison. Further, the sublimation rate of Cr_2O_3 is included, interpolated from the results shown in Fig. 8.7.

The total mass gain of the alloy is $1 \times 10^{-5}\,\mathrm{mg\,cm^{-2}\,s^{-1}}$. The alloy follows a linear oxidation kinetics, just as shown in dry air in section 8.1. The lamella-like structure of the protective oxide layer (see Fig. 8.9) indicates continuous failure and self-healing of the protective oxide layer. The concept of a failure probability as introduced in section 8.1 remains valid - the key difference is the presence of H allowing the Cr_2O_3 to heal as discussed above.

The mass gain of the catcher while the alloy hangs inside the catcher is $s_{\mathrm{catcher}} = 0.23 \times 10^{-6}\,\mathrm{mg\,cm^{-2}\,s^{-1}}$. Using the calibration shown in Fig. 8.7, the amount of W-containing oxide sublimating from the alloy is calculated

$$s_{\mathrm{W}}^{\mathrm{A}} = \frac{s_{\mathrm{catcher}}}{0.43} = 0.5 \times 10^{-6}\,\mathrm{mg\,cm^{-2}\,s^{-1}}. \tag{8.11}$$

This result is a half as compared to the calculation based on the surface coverage with W-containing oxides. Both methods have measurement uncertainties: for the catcher it is neglected that material can also sublimate from the catcher after long oxidation times. Further, it is assumed without experimental proof that the efficiency of the catcher independent on the absolute sublimation rate. On the other hand, the calculation based on the surface coverage already has an uncertainty of a factor of 2 due to the uncertainty on the exact surface coverage with W-containing oxides. Further, the assumption that the W-containing oxide on the surface of the alloy sublimates at the same rate as WO_3 requires experimental verification. Overall, the two independent methods for determining the sublimation of W oxides from the alloy yield the same results within the measurement uncertainties. This result indicates that the aforementioned approximations are reasonable.
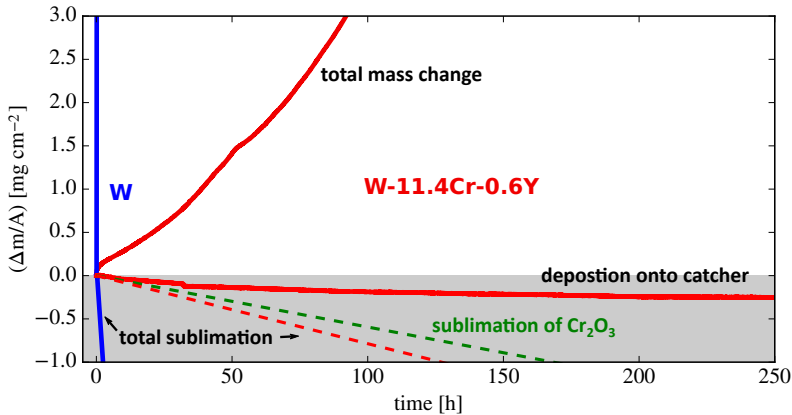
Figure 8.10: Mass change of a W-11.4Cr-0.6Y alloy and pure W as a function of time at 1273 K in humid air. The upper part shows the total mass change of the sample. The lower part shows the contribution of sublimation - the deposition onto the catcher and the calculated total sublimation are plotted.

Radiological considerations

For the first time it is achieved, that the total sublimation rate from the alloy is dominated by the sublimation of Cr_2O_3 $s_{\mathrm{Cr}}^{\mathrm{A}} = 0.99 s_{\mathrm{Cr}} = 2 \times 10^{-6}\,\mathrm{mg\,cm^{-2}\,s^{-1}}$. Adding

the contribution from W-containing oxides yields a total sublimation rate around $s = 3 \times 10^{-6}\,\mathrm{mg\,cm^{-2}\,s^{-1}}$ in case of a LOCA featuring humid air and a temperature of $1273\,\mathrm{K}$, as plotted in Fig. 8.10.

The activity after $5\,\mathrm{fpy}$ of neutron irradiation is $8.74 \times 10^{14}\,\mathrm{Bq\,kg^{-1}}$ and $2.91 \times 10^{14}\,\mathrm{Bq\,kg^{-1}}$ for W and Cr, respectively [19]. The activity $5.3\,\mathrm{min}$ after neutron irradiation stopped is used in order to discard very short lived isotopes from the estimation of the radiological hazard. The radioactive release r_r is calculated assuming a first wall surface area of $1000\,\mathrm{m^2}$ and that all sublimated material is released to the environment. The calculation yields $r_r = 3 \times 10^{16}\,\mathrm{Bq/month}$ for the smart alloy as compared to $r_r = 3 \times 10^{18}\,\mathrm{Bq/month}$ for pure W first wall armor at $1273\,\mathrm{K}$. Thus, the potential release of radioactivity is suppressed by a factor of almost 100 by employing smart alloys. Nevertheless, a radioactive safety hazard remains; the required safety limits for future fusion power plants should be specified and additional means to mitigate the radiological hazard should be considered.

8.3   Influence of temperature on oxidation

Optimized W-11.4Cr-0.6Y bulk alloys are oxidized in humid air at atmospheric pressure for $2\,\mathrm{days}$ at three different temperatures: $1100\,\mathrm{K}$, $1273\,\mathrm{K}$, and $1473\,\mathrm{K}$. The milling, sintering, and grinding procedure still follows the recommendations from chapter 7.

In contrast to the other samples in this thesis, there is a different storage time of the powder between milling and sintering: the powder for all samples in this section is stored for month while the powder for the samples in section 8.2 is stored only days. The long powder storage causes an increase of the O content from $0.15\,\mathrm{wt.\,\%}$ to $0.19\,\mathrm{wt.\,\%}$ in the sintered sample. The N content stays constant at $8 \times 10^{-3}\,\mathrm{wt.\,\%}$. O and N content are measured using the LECO determinator described in section 2.6. The results of the oxidation experiment are shown in Fig. 8.11.

At $1473\,\mathrm{K}$ a total mass change at the rate of $-5 \times 10^{-4}\,\mathrm{mg\,cm^{-2}\,s^{-1}}$ is measured after $4\,\mathrm{h}$ of oxidation, see Fig. 8.11. This mass change includes the mass gain due to oxidation and the mass loss due to sublimation, which is dominating. Thus, the sublimation rate is even higher. The sample is mechanically destroyed after $44\,\mathrm{h}$, as shown in the photograph. The protection observed at $1273\,\mathrm{K}$ and discussed in section 8.2 cannot be maintained at $1473\,\mathrm{K}$. The alloy cannot provide radiological safety in case of a LOCA featuring such high temperatures.

At $1273\,\mathrm{K}$ a total mass change at the rate of $2 \times 10^{-5}\,\mathrm{mg\,cm^{-2}\,s^{-1}}$ is measured, see Fig. 8.11. The photograph after $44\,\mathrm{h}$ of oxidation shows that the cubic shape of the sample is preserved. The sample turns green as a protective Cr_2O_3 layer forms.

A detailed characterization and discussion of the protective oxide layer formed at $1273\,\mathrm{K}$ is found in section 8.2. The oxidation rate doubled compared to the samples presented in section 8.2 due the increased O level in the initial samples - the reaction of the contained Y to Y_2O_3 can only bind up to $0.16\,\mathrm{wt.\,\%}$, leaving at least $0.03\,\mathrm{wt.\,\%}$ of excess O which is bound by Cr. More details on how Y and O are bound in the material are given in chapter 9. The fact that such a small amount of O has such a strong effect indicates that binding O in the material is one important role of the contained Y. The author assumes that a higher O content would yield further degradation of the oxidation resistance. Still, in the present samples the O content is increased by only $0.04\,\mathrm{wt.\,\%}$ as compared to the samples presented in section 8.2, the protective Cr_2O_3 is still formed and maintained, and the sample can be used for analysis.

At 1100 K the total mass change is reduced by a factor of 20 as compared to the experiment at 1273 K due to the lower temperature. The durability time of the alloy is increased.

Studies of influences on the oxidation resistance should continue. Important tests include the oxidation behavior in atmospheres with higher water content. Further, the activation of the material is highest at the end of the life-time of the first-wall armor components when they were exposed to the highest total neutron fluence. Thus, a good oxidation resistance is most crucial in case of an accident at the end of the life-time of the first-wall armor material. Therefore, changes of characteristics after usage in the power plant must be assessed. Most critical influences are sputtering of the surface by the plasma, long-term exposure to elevated temperatures of around 900 K for years, and transmutations of alloying elements. First studies on the influence of sputtering of the surface by the plasma indicate that the oxidation resistance remains similar as compared to unexposed samples [99, 100].
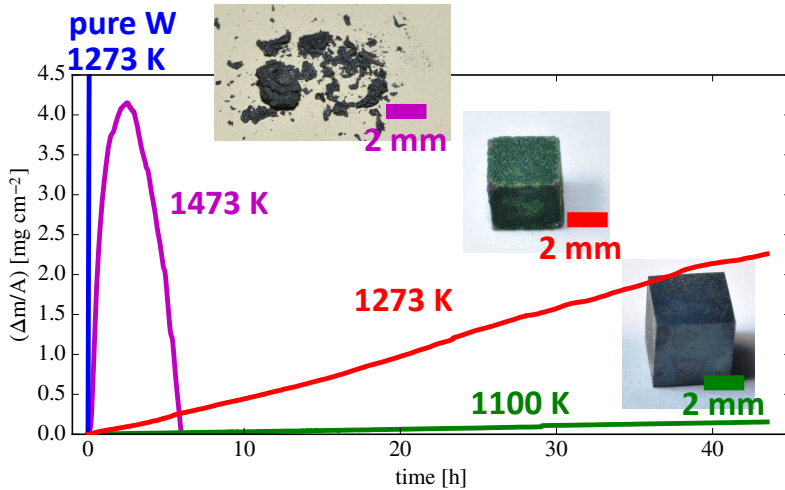
Figure 8.11: The total mass change as function of time for three identical W-11.4Cr-0.6Y alloys at different temperatures as compared to pure W. Measurements are performed in humid air at a temperature as specified in the label. The photographs are taken after 44 h of oxidation. Figure adapted from F. Klein et al. [98].

The key findings of the oxidation and sublimation process in humid air are as follows:

- At 1273 K sublimation from the smart alloy in humid air is dominated by the slow release of the protective Cr_2O_3. A total sublimation rate around $s = 3 \times 10^{-6}\,mg\,cm^{-2}\,s^{-1}$ is measured.

- A continuous, self-healing protective Cr_2O_3 layer forms on the surface of smart alloys during oxidation.

- Smart alloys can withstand the exposure up to 1273 K in humid air suppressing the release of radioactive material. Design concepts of future fusion power plants should take this information into account.

Chapter 9

Oxidation mechanisms of smart alloys

In previous chapters it was shown that W-Cr-Y alloys have an improved oxidation resistance as compared to pure W. The influence of various parameters on the oxidation and sublimation process was discussed. This chapter is dedicated to experiments contributing to an advanced understanding of the oxidation mechanisms of smart alloys. Thin films deposited by magnetron sputtering (see section 2.1 and chapter 5) and bulk samples produced via the optimized procedure given in chapter 7 are investigated. The type of sample is specified for each experiment.

9.1 Oxidation mechanisms of thin films on a micro-scale

9.1.1 On diffusion of O

The growth of a protective oxide layer is the essential part for the improved oxidation resistance. Fundamentally there are two options for the growth direction as illustrated in Fig. 9.1. The first option, illustrated in Fig. 9.1 a, is that the oxide grows at the interface of the oxide with the alloy. Cr has a Pilling–Bedworth ratio of 2 [44], thus the volume expansion of the new oxides can cause spallation of the oxide scale once sufficient stresses built up. The other option - Cr_2O_3 growth at the outermost surface is illustrated in Fig. 9.1 b. In that case the Cr_2O_3 can expand freely, which is desired in order to have a stable, protective oxide layer.
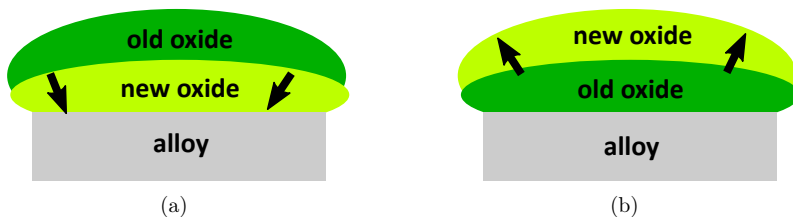
Figure 9.1: Schematic of the two options for the oxide growth direction. (**a**) The oxide grows at the interface of the alloy and the oxide. (**b**) The oxide grows at the surface, the interface of the atmosphere and the oxide.

The growth direction of the oxide of a W-12Cr-0.6Y alloy is determined in a dedicated experiment consisting of two parts:

- Part 1: the sample is oxidized for 65 min in natural O_2 + Ar flow. While keeping a constant temperature and a constant flow, the natural O_2 is substituted by isotope $^{18}O_2$ and oxidation is continued for another 11 min. During these 11 min $^{16}O_2$ still remains in the furnace but is gradually replaced by the $^{18}O_2$, thus the ratio of $^{18}O/^{16}O$ changes.

- The sample is removed from the furnace and the oxygen-isotope content in dependence of depth is measured using SIMS, see Fig. 9.2.

- Part 2: oxidation of the same sample is continued at 1273 K in natural O_2 + Ar for 20 min.

- The sample is removed from the furnace and the oxygen-isotope content in dependence of depth is measured again using SIMS, see Fig. 9.2.

The SIMS device cannot measure ^{18}O and ^{16}O isotopes in parallel in the oxide layer and in the alloy: a low $Bi_3{}^+$ current allows to measure ^{16}O throughout the entire sample. However, using a low current the ^{18}O signal drops below the detection limit in the alloy. A high $Bi_3{}^+$ current allows to measure ^{18}O throughout the entire sample. However, using a high current the ^{16}O signal saturates in the oxide layer and cannot be used for determining the isotope abundance. The high current allows to also measure the molecules $^{16}O_2$ and $^{16}O^{18}O$ in the oxide. The different O-isotopes are chemically identical. Therefore, the ^{18}O isotope abundance in the oxide, which is marked with gray background in Fig. 9.2, is calculated using the ratio of $^{16}O^{18}O/^{16}O_2$. In the alloy the ratio of $^{16}O/^{18}O$ is used to calculate the ^{18}O isotope abundance $p(^{18}O)$.

The exact formulas for the calculations are derived in the following. The ^{18}O isotope abundance $p(^{18}O)$ is the probability to have an ^{18}O atom if one finds any O-atom. That implies

$$p(^{16}O) + p(^{17}O) + p(^{18}O) = 1 = 100\,\% \tag{9.1}$$

Accordingly $p(^{18}O^{16}O)$ is the probability to have an $^{18}O^{16}O$ molecule if one has a molecule consisting of any two oxygen atoms. The concentration of ^{17}O is assumed constant at the natural abundance for all employed oxygen, thus $p(^{17}O) = 0.038\,\%$.

In the alloy SIMS measures counts for both $^{18}O^-$- and $^{16}O^-$-ions. The value

$$a = \frac{\text{counts}(^{18}O^-)}{\text{counts}(^{16}O^-)} \tag{9.2}$$

can be introduced. As both ions are chemically identical, the count ratio of ions equals the probability ratio of atoms, thus

$$a = \frac{p(^{18}O)}{p(^{16}O)} \Rightarrow p(^{18}O) = \frac{a(1 - p(^{17}O))}{1 + a}. \tag{9.3}$$

In the oxide SIMS measures counts for the O_2 molecules. $^{18}O^{16}O$ and $^{16}O_2$ can be detected while the signal from $^{18}O_2$ is too small. The value

$$b = \frac{\text{counts}(^{18}O^{16}O^-)}{\text{counts}(^{16}O_2{}^-)} \tag{9.4}$$

can be introduced. As both molecules are chemically identical, the count ratio of ionized molecules equals the probability ratio of molecules. The ^{18}O isotope abundance in the oxide can be calculated using equations 9.1 and 9.4.

$$
\begin{aligned}
b &= \frac{p(^{18}\text{O}^{16}\text{O})}{p(^{16}\text{O}_2)} \\
&= \frac{p(^{18}\text{O}) \times p(^{16}\text{O}) + p(^{16}\text{O}) \times p(^{18}\text{O})}{p(^{16}\text{O}) \times p(^{16}\text{O})} \\
\Rightarrow p(^{18}\text{O}) &= \frac{b(1 - p(^{17}\text{O}))}{2(1 + b/2)}
\end{aligned}
\tag{9.5}
$$

Thus, the physical value $p(^{18}\text{O})$ is calculated in the oxide and the alloy. The results are combined in Fig. 9.2. Both measurements show a small maximum at the interface between the oxide and the alloy. This is the point where the accuracy of both calculation methods for $p(^{18}\text{O})$ decreases as a mixture of oxides and metals is measured. Therefore, this maximum at depth of $\sim 0.5\,\mu\text{m}$ is attributed to an artifact in the measurement.

After part one of the experiment, see Fig. 9.2, $p(^{18}\text{O})$ has a maximum at the surface of the oxide layer and decreases with higher depth. At a depth of around $1\,\mu\text{m}$ $p(^{18}\text{O})$ increases gradually by $0.1\,\%$ to a local maximum at a depth of around $2\,\mu\text{m}$.

After part two of the experiment, see Fig. 9.2, $p(^{18}\text{O})$ is close to the natural abundance at the surface of the sample. A maximum of $p(^{18}\text{O}) \approx 2.5\,\%$ is found $\sim 0.1\,\mu\text{m}$ below the surface. The following decrease of $p(^{18}\text{O})$ is steeper as compared to the decrease in part one. Throughout the remaining oxide and in the first $\sim 0.5\,\mu\text{m}$ of the alloy $p(^{18}\text{O})$ is constant below $0.5\,\%$. A broad local maximum in $p(^{18}\text{O})$ is found at a depth of around $2\,\mu\text{m}$, the same depth where the local maximum after part one is seen. Thus, a fraction of O must have diffused to a depth of $2\,\mu\text{m}$ during the $0.5\,\text{h}$ oxidation.

Combining the result from part one and two of the experiment shown in Fig. 9.2 there are two main conclusions:

- The ^{18}O supplied during the last minutes of part one of the experiment is enriched at the surface of the protective oxide layer. New Cr_2O_3 forms on top of the ^{18}O enriched Cr_2O_3 during part two. Thus, the oxide layer grows primarily at the surface in direct contact with the oxidizing atmosphere. This is an important finding as the the new Cr_2O_3 can freely expand, as illustrated in Fig. 9.1 b. There is no risk of spallation due to volume expansion of Cr_2O_3.

- The second finding is based on the maximum of $p(^{18}\text{O})$ at a depth of $2\,\mu\text{m}$ and the narrowing of the ^{18}O peak in the oxide, see Fig. 9.2. The broadening of the $p(^{18}\text{O})$ peak in the oxide after part one is caused by ^{18}O which is not bound to Cr and immobile at room temperature; cooling after part one is performed at a rate of $40\,\text{K}\,\text{min}^{-1}$. In part two, this free ^{18}O diffuses to the maximum depth of the internal oxide where new internal oxides can form and the local maximum in $p(^{18}\text{O})$ appears at a depth of $2\,\mu\text{m}$. The maximum is an evidence that the duration of the oxidation was long enough to allow diffusion. Longer oxidation in ^{18}O would only cause an plateau in the ^{18}O isotope abundance starting at the depth of the current maximum and extending to higher depth. The internal oxide remains immobile once formed and O must diffuse into the alloy to form internal oxides.
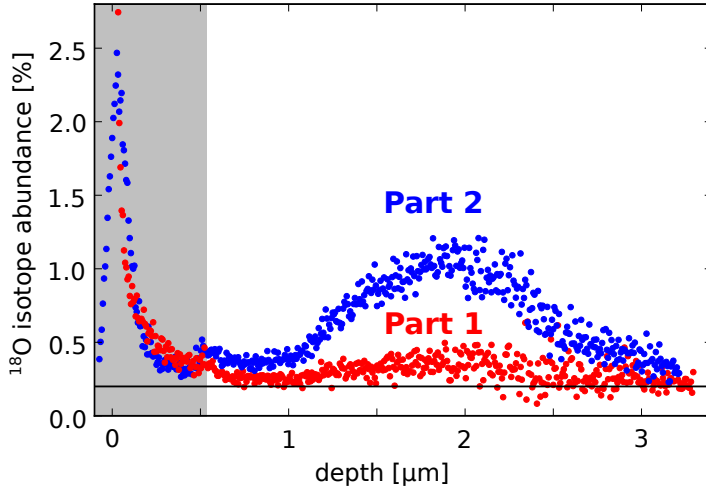
Figure 9.2: The ^{18}O isotope abundance after oxidation of W-12Cr-0.6Y at 1273 K. Times and atmosphere are chosen as follows: part 1: 65 min in Ar + ^{16}O$_2$ atmosphere followed by 11 min with increased ^{18}O abundance. Part 2: continued oxidation of the sample from part 1 for 20 min in Ar + ^{16}O$_2$ atmosphere. The depth to which the Cr$_2$O$_3$ layer extends is marked in gray. The natural abundance of 0.2 % ^{18}O is marked by the black line [101]. Figure adapted from F. Klein et al. [78].

9.1.2 On diffusion of Cr

From the studies on the diffusion of O in the previous section it is already known that the formation of the protective oxide layer is caused by the diffusion of Cr. Here, the diffusion of Cr is studied in more detail. For that purpose a 7.6 µm thick W-13Cr-1Y film is oxidized for 6 h at 1273 K. The cross section is shown in Fig. 9.3: SEM, EDX, and SIMS show a Cr$_2$O$_3$ layer followed by the alloy with a relatively constant Cr concentration. Within the first few µm of the alloy (region B), pores with the size of 50 nm to 100 nm are found. Cr-rich and -poor phases are found in region C. First the findings on a local scale - phase and pore formation - are discussed. Second, the transport of Cr to the surface replenishing the protective oxide scale is discussed.
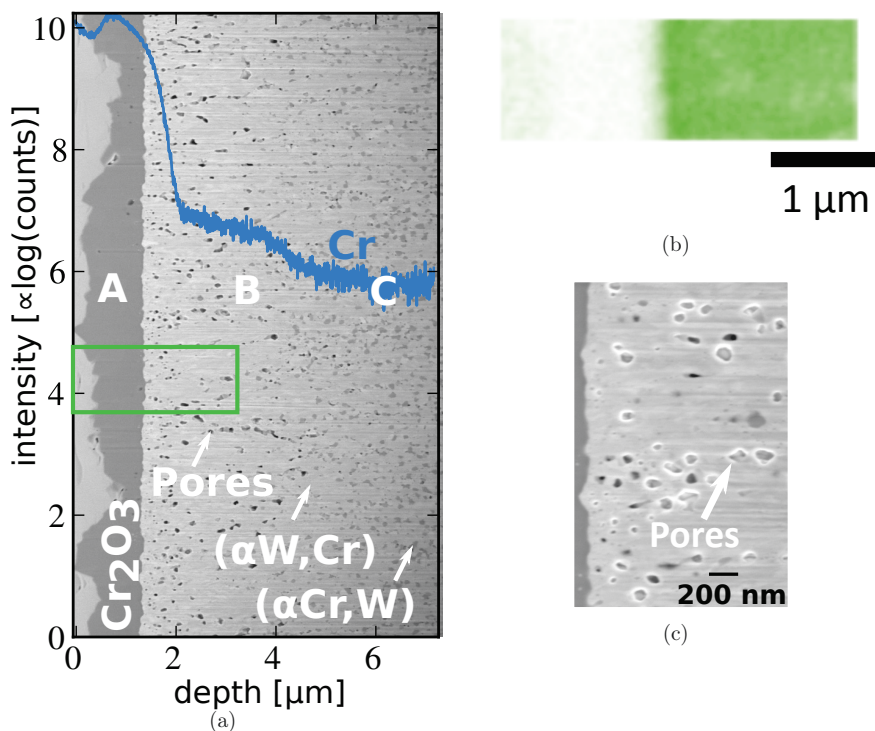
Figure 9.3: (**a**) Cross section of a 7.6 μm thick W-13Cr-1Y alloy exposed to a temperature of 1273 K in 20 kPa O_2 and 80 kPa Ar atmosphere for 6 h. The corresponding Cr profile measured using SIMS and (**b**) an EDX map of W based on the W M_α line at the location of the green box in (a) are included. (**c**) Increased magnification, showing the pores more clearly.

Local Cr-rich phase formation

The pores and the Cr rich phase shown in Fig. 9.3 have a similar size and shape. This observation yields the hypothesis that grains from the Cr-rich phase form porosity once their Cr is consumed - a first indication that Cr in the Cr-rich phase participates in replenishing the protective oxide layer. An additional experiment is presented in the following in order to verify this hypothesis.

The effects of phase formation and of oxidation are separated in a dedicated experiment: the furnace is evacuated and filled with 99.9999 % pure Ar. This procedure is repeated 9 times for optimum purity. The minimum pressure reached in the furnace during evacuation is 0.8 Pa for the atmosphere labeled Ar_a. For the atmosphere labeled Ar_b the minimum pressure is 0.6 Pa resulting in a different residual oxygen level as compared to Ar_a. 3.6 μm thick films are annealed in the created Ar atmosphere for 1.25 h and 3 h. The residual oxygen causes slow mass gain due to oxidation during annealing, the oxygen level and thus the mass gain rate is different in Ar_a and Ar_b.

The microstructure of the sample after annealing for 3 h is shown in Fig. 9.4 a. EDX identifies the darker regions as the (αCr, W) phase, whereas the brighter regions are identified as the (αW, Cr) phase. The annealed samples are oxidized at 1273 K

in 20 kPa O_2 and 80 kPa Ar atmosphere. The oxidation kinetics of the samples are shown in Fig. 9.4 b. A sample without annealing prior to oxidation is included as a reference measurement. The details on the different stages of the oxidation process are explained in section 5.2.1. The plotted mass change is relative to the mass of the sample before oxidation and before annealing. To allow a better comparison to the reference measurement, the oxidation curves after annealing are shifted in time. The time shift is chosen so that the mass gain of the sample after annealing matches the mass gain of the reference measurement.

Despite annealing the three stages of the oxidation process are still observed, no clear effect on the oxidation behavior is found. The transition to oxidation stage III occurs at a mass gain above ~ 0.15 mg cm^{-2} due to the depletion of Cr, as discussed in section 5.2.3. The region of Cr depletion is shaded in Fig. 9.4 b.

This finding suggests, that the oxidation resistance in stages I and II is not driven by the phase formation. The Cr dissolved in the (αCr, W) phase remains available for replenishing the protective oxide layer. As a consequence for future alloy development, it is not crucial to find ways to avoid phase formation on a nano-scale. A homogeneously distributed (αCr, W) phase, with clusters not larger than a few tens of nm - which are seen in Figure 9.4 a - does not degrade the oxidation resistance of the alloy.

(a)   (b)
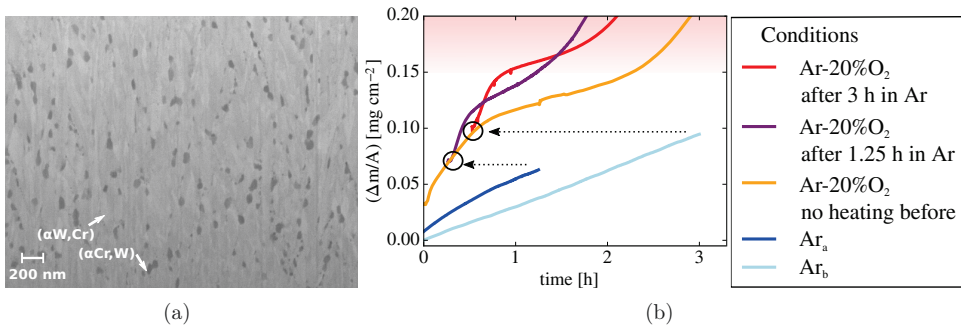
Figure 9.4: (**a**) Phase formation in a W-12Cr-0.5Y film after 3 h annealing in Ar; (**b**) Mass change with respect to time of annealed W-12Cr-0.5Y samples at 1273 K in 20 kPa O_2 and 80 kPa Ar atmosphere. The annealing times in Ar are 0 min, 1.25 h, and 3 h. Figure adapted from F. Klein et al. [78].

Transport of Cr to the surface

The Cr transport is estimated based on SIMS measurements of the Cr concentration as a function of depth shown in Fig. 5.5 b and 9.3. The surface roughness and pores cause smearing out of sharp interfaces: according to the SEM image the transition from the protective oxide to the metal occurs within 0.05 µm. However, in the SIMS profile the transition zone is around 0.6 µm which limits the analysis to a micro-scale. No conclusions on the material within nanometers from the interface can be drawn.

Further, matrix effects change the probability of ionization, therefore the intensity of the secondary Cr ions is increased when sputtering CrO_x instead of pure Cr [102]. This effect is observed in region B (the first 2 µm in Fig. 9.3) where internal oxidation is present. Thus, the gradient in region B may not be caused by a variation in Cr content, but by a reduction of O. The SIMS measurement resolves a constant Cr level in region C starting

from a depth of $2\,\mu m$. The Cr profile is similar for the samples shown in Fig. 5.5 b and 9.3 despite the different sample thickness and the different oxidation time. In both cases, a concentration gradient in region B (near the protective oxide layer) is expected to cause a concentration gradient in region C (near the substrate). Therefore, the measurement of a constant Cr concentration in region C allows to conclude that the Cr concentration with depth is constant in the entire alloy on a micrometer scale.

The constant Cr concentration is essential for continuously replenishing the protective Cr_2O_3 layer suppressing the formation of WO_3. The details are discussed in section 5.2.3 where the lifetime of a $2\,mm$ thick W-Cr-Y component is estimated in case of a LOCA. Diffusion of Cr is the key for providing the constant concentration.

The diffusion coefficient D of Cr impurities in W is given by

$$D(T = 2084\,\text{K}) = D_0 \times \exp\left(-\frac{Q}{k_B T}\right) = 1.74 \times 10^{-18}\,\text{m}^2\,\text{s}^{-1} \qquad (9.6)$$

with the Boltzmann constant k_B, the pre-exponential factor $D_0 = 0.89 \times 10^{-4}\,\text{m}^2\text{s}^{-1}$, and the diffusion energy $Q = 5.669\,\text{eV}$ valid in the temperature range from $2084\,\text{K}$ to $2658\,\text{K}$ [103]. The diffusion coefficient D is proportional to the mean square displacement s of atoms in three dimensions. After $75\,min$ of oxidation $s = \sqrt{6Dt} = 2 \times 10^{-7}\,\text{m}$. The expected displacement in the experiment in this work is much smaller as the temperature is only $1273\,\text{K}$ instead of the $2084\,\text{K}$ in the calculation. The displacement in the experiment is estimated based on the depth d from which Cr in the oxide layer must originate. d is given by

$$d = \frac{m_{\text{Cr}}}{A\rho c} = 5 \times 10^{-7}\,\text{m} \qquad (9.7)$$

where $m_{\text{Cr}} = 0.09\,mg$ is the mass of Cr in the scale, $A = 1.1\,cm^2$ the sample area, $\rho = 15\,\text{g}\,\text{cm}^{-2}$ the measured alloy density, and $c = 12\,\text{wt}.\,\%$ the Cr concentration. d is the minimum displacement of Cr and larger than s calculated above. Thus, Cr diffuses faster than expected from [103]. Yttrium, the nano-structure of the alloy, which is investigated in section 9.2, and the sub-micron grain size cause this behavior.

9.2 Oxidation mechanisms of smart alloys on a nano-scale

9.2.1 Scanning transmission electron microscopy on a thin film after oxidation

The W-12Cr-0.5Y alloy shown in Fig. 5.5 b is chosen for the STEM measurement. An insight on a nano-scale into the material during working passivation is anticipated, the distribution of Y is of particular interest as Y is crucial for the oxidation resistance but not resolved by measurements previously presented in this work. A lamella is cut by FIB perpendicular to the substrate conserving the layered structure of oxide and alloy. The lamella has a thickness of $\sim 0.08\,\mu\text{m}$, a width of $\sim 11\,\mu\text{m}$, and a height of $\sim 8.6\,\mu\text{m}$ and is imaged by STEM and EDX with an electron energy of $200\,\text{keV}$. A finite thickness of the lamella allows overlapping of features in viewing direction as illustrated in the schematic Fig. 9.5 a. Overlapping yields a superposition of structures in the 2D-image.

STEM in the metallic thin film

STEM and EDX images of region A, the lower half of the sample as illustrated in Fig. 9.5 a, are shown if Fig. 9.5 b-d. Lines of different contrast are seen parallel to the surface at a periodicity of $7\,\text{nm}$. These lines indicate a variation in concentration parallel to the surface. In the magnetron deposition process around $7\,\text{nm}$ of material are deposited during each rotation of the stage. Thus the concentration gradients are generated during the deposition process. In addition, different grains and their boundaries are shown. The EDX measurements shown in Fig. 9.5 c confirm that the brighter grains have a higher Cr content as compared to the darker grains. Thus, the brighter grains are referred as Cr-rich phase. The mapping of Y in Fig. 9.5 d cannot resolve Y particles or agglomerations despite the high resolution down to a few nanometers. However, the K_α line of Y in the spectrum in the inset shows clearly that Y is detected. In conclusion, Y/Y_2O_3 within the observed area is dispersed in fine particles (or individual atoms) which are smaller than the image resolution of around $3\,\text{nm}$.

The fine dispersion of the Y atoms after the magnetron deposition is stable at elevated temperatures throughout the oxidation experiment. In contrast, [45] has shown that Y segregates at the grain boundaries. In the absence of data on the diffusion of Y_2O_3 or $YCrO_2$ in W, it is calculated if metallic Y had sufficient time to diffuse to the grain boundaries during the oxidation experiment: the diffusion coefficient D of Y in W at a temperature between $1473\,\text{K}$ and $1873\,\text{K}$ is calculated from equation 9.6 with $D_0 = 6.7 \times 10^{-7}\,\text{m}^2\text{s}^{-1}$, and $Q = 2.953\,\text{eV}$ [104]. Interpolation to $1273\,\text{K}$ yields that the Y atoms have a displacement of around the grain size in the alloy after $75\,\text{min}$. However, the Y in the alloy is bound to O. In order to diffuse as Y, the binding energy to O of around $1 \times 10^1\,\text{eV}$ must be overcome. The length of an Y-O bond is $2.3\,\text{Å}$ [105], whereas the atomic radius of an Y^{3+} ion is only $0.9\,\text{Å}$ [84]. Thus, Y-O is less mobile than Y and segregation at the grain boundaries within the given time was not to be expected.
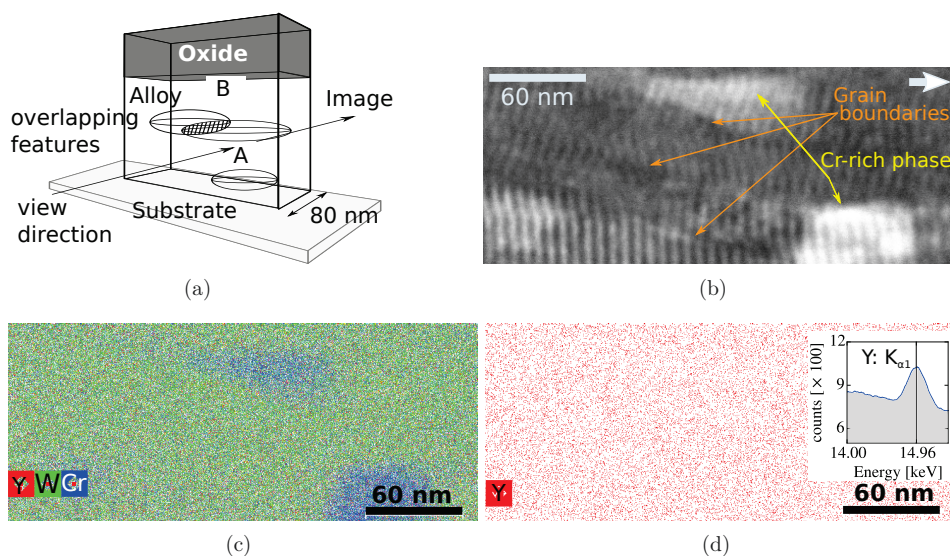
Figure 9.5: W-12Cr-0.5Y alloy oxidized at 1273 K for 75 min in 20 kPa O_2 and 80 kPa Ar atmosphere. (**a**) Schematic drawing of a lamella, not in scale. Measurements are conducted in regions A and B; (**b**) STEM measurement in region A. The white arrow points towards the surface oxide layer; (**c**) combined EDX map of W, Cr, and Y corresponding to the area shown in (b); (**d**) separate EDX map of Y and the spectrum added up over the whole mapping area in the inset. Figure adapted from F. Klein et al. [78].

STEM at the interface of the oxide and the metallic thin film

STEM and EDX images of region B - the interface between alloy and surface oxide layer, as illustrated in Fig. 9.5 a - are shown in Fig. 9.6. Fig. 9.6 a is the dark-field image where the scattered electrons are detected. Scattering in a metal is different as compared to scattering in an oxide. Therefore, there is a large brightness deviation between the surface oxide layer and the alloy: good contrast in both regions is achieved by using two different color scales.

A sharp change in composition at the interface is found in the EDX maps of all contained elements (W, Cr, Y, and O) - see Fig. 9.6 b-f. EDX detects Cr and O in the oxide layer, neither W nor Y is detected by EDX in the oxide layer. W is detected in the alloy, with a decreased intensity at the spots where internal oxides are present. The internal oxides cause an increased Cr and O signal.

The Y signal in EDX, see Fig. 9.6 e, is homogeneous within the alloy, it is independent of grain boundaries and internal oxides. A single circular spot with a diameter of 30 nm is detected at the interface of the alloy and the protective oxide layer. This is a nucleation site with an increased Y content as compared to the alloy. No contrast is seen in the electron image as the yttrium content is only a few percent higher as compared to the W matrix. The effect of Y and such nucleation sites on the oxidation resistance is discussed in section 9.2.3 where the observations from STEM and atom probe tomography are combined.
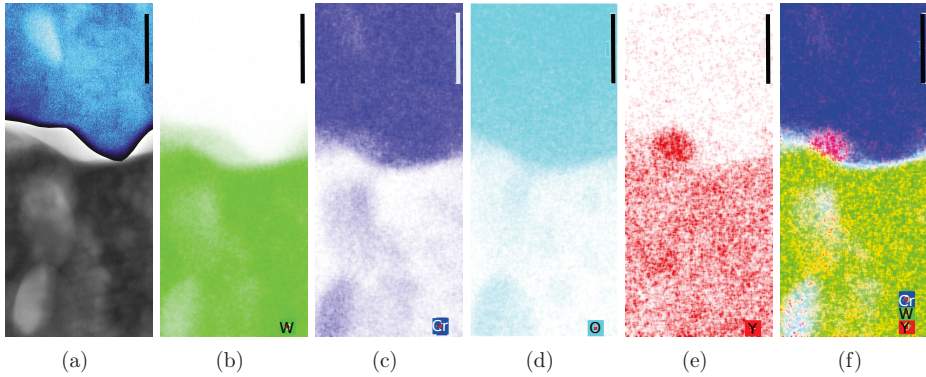
Figure 9.6: STEM measurement in region B, as indicated in Fig. 9.5 a. The W-12Cr-0.5Y alloy is oxidized at 1273 K in 20 kPa O_2 and 80 kPa Ar atmosphere for 75 min. The length of the scale bar in the top right corner is 50 nm for all images. (**a**) Dark-field image using two different color maps: one for the Cr_2O_3 layer and one for the alloy; EDX map measurements of (**b**) W, (**c**) Cr, (**d**) O, and (**e**) Y. (**f**) Overlay of images (**b,c,e**). Figure adapted from F. Klein et al. [78].

9.2.2 Atom probe tomography on a bulk sample after oxidation

Overall, the STEM measurement alone does not provide a concise answer on the exact mechanism how the Y improves the oxidation resistance. This section presents Atom Probe Tomography (APT) studies on sintered bulk smart alloys. The results are complementary to the STEM results from section 9.2.1 and yield first qualitative hypotheses on how Y improves the oxidation resistance, as presented in section 9.2.3.

A sample with the best known oxidation resistance as investigated in Fig. 8.10 is chosen - the powder in the optimized elemental composition is stored only a few days ensuring an O content below 1.4 at. %; it is compacted with optimized sintering parameters, and the grinding procedure follows the optimized routine. Oxidation is performed in humid air at 1273 K for 20 h. Thus, the alloy is studied in an early stage of the oxidation process where the protecting mechanisms are fully in operation. After cooling the sample to room temperature a tip, as shown in Fig. 9.7, is cut using FIB. The tip has a height of $\sim 1.6\,\mu$m and a diameter of $\sim 0.3\,\mu$m.
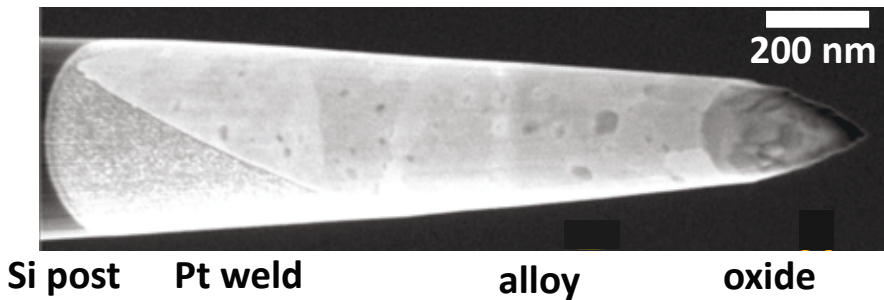
Figure 9.7: A SEM image of the tip cut for the APT study.

Measurements on the top of the tip are performed as explained in section 2.15. The region around the interface of the Cr_2O_3 layer to the alloy is chosen as region of interest. The adhesion of the oxide layer to the alloy is not strong enough to allow a measurement across the interface. Thus, there is one measurement of the oxide scale just above the interface, see Fig. 9.8, and one measurement of the alloy just below the interface, see Fig. 9.9.

Atom probe tomography on the oxide

The dataset in the oxide, shown in Fig. 9.8, contains 7.3×10^6 ions. Fig. 9.8 a shows Cr, Y, W, and WO. O not bound to W is excluded from the plot for improved visibility of the other elements, the O is shown in a separate elemental map (see Fig. 9.8 b). The W and Y impurities within a grain of the Cr_2O_3 are below 0.002 at. %, i.e. the Cr_2O_3 oxide grains are very pure. Y is detected at the grain boundaries of the Cr_2O_3, as shown in Fig. 9.8 a. Fig. 9.8 c shows a line scan across a grain boundary. A grain boundary has a width of around 4 nm with a maximum Y concentration of 0.6 at. %.

The finding on Y at the grain boundaries does not contradict the finding in section 9.2.1 where the STEM study on thin films did not detect Y in the Cr_2O_3: the grain

(a)

(b)

(c)
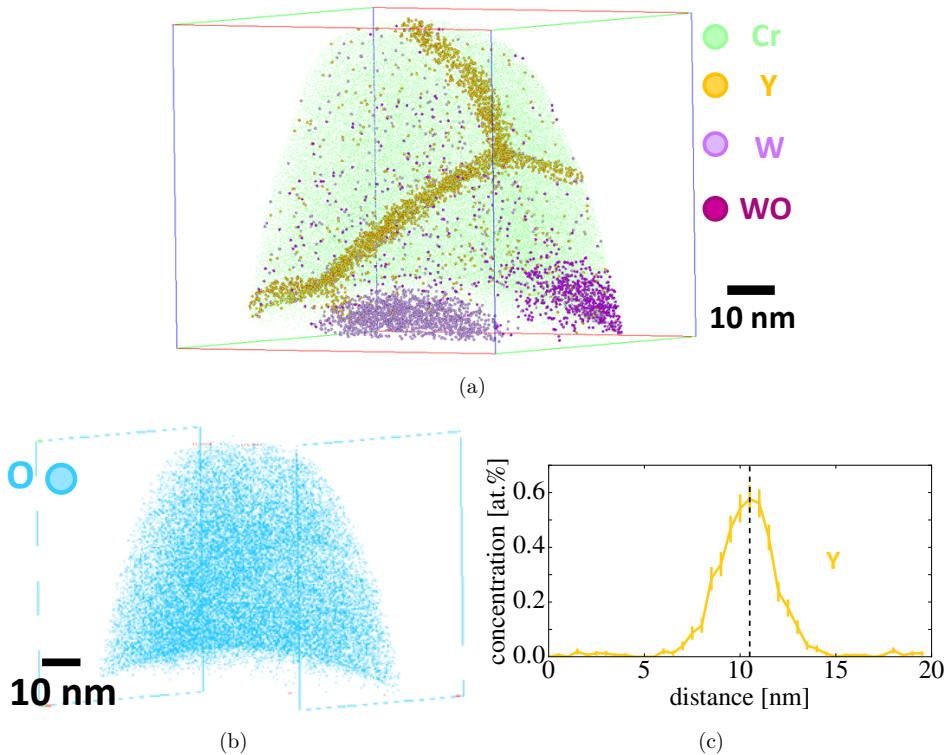
Figure 9.8: Results of the APT measurement in the Cr_2O_3 scale. (**a**) the elemental distribution of Cr, Y, W, and WO in a three dimensional image. (**b**) the elemental distribution of O in a three dimensional image. (**c**) the concentration of Y in a line scan across a grain boundary.

boundary with a size of 4 nm is very localized and the increase of the Y content at the grain boundary is small - thus, the increase expected in the lamella with a thickness 20 times larger than a grain boundary is $0.6\,\text{at.\%}/20 = 0.03\,\text{at.\%}$. Such a small, localized increase is lost in the noise of the EDX measurement.

The interface between the protective oxide layer and the metal is located at the bottom of Fig. 9.8 a: below the Cr_2O_3, W and a W oxide particle are detected. The interface of the Cr_2O_3 to the metal is resolved in detail in Fig. 9.9. At the interface between Cr_2O_3 and the W oxide, the Y content increases from $0\,\text{at.\%}$ to $\sim 2\,\text{at.\%}$. Both Cr and Y signals drop to $0\,\text{at.\%}$ within the WO_3. The formation of WO_3 causes volume expansion resulting in weakening of the protective oxide layer. Thus, WO_3 formation is undesirable. One hypothesis is that the increased Y content in the vicinity of WO_3 suppresses the formation of WO_3 particles, as W-containing oxides are more dominant in Y-free alloys, see Fig. 5.5.

Atom probe tomography below the oxide

APT analysis of the alloy below the Cr_2O_3 layer is shown in Fig. 9.9. The dataset contains 8.7×10^6 ions. Fig. 9.9 a shows an overview of the analyzed volume where regions of increased interest are marked as (b) and (c) which are shown at higher magnification in Fig. 9.9 b and c, respectively: Fig. 9.9 b depicts the Y-Cr-O nano-particles in the metal while Fig. 9.9 c shows the interface between the metal and the oxide.

As seen in Fig. 9.9, in particular Fig. 9.9 b, all Y contained in the alloy is located in nano-particles with a diameter of 10 nm to 50 nm. Concentration profiles in the nano-particles can be depicted by a proximity histogram. A proximity histogram is generated in three steps [106]: first, a regular grid is generated based on the positions of the atoms. Second, an isoconcentration surface is identified in this grid. Third, the local concentration of an atom as a function of proximity to the surface is determined and plotted in a histogram. The result for the biggest nano-particle is depicted in Fig. 9.9 d. The transition zone from the alloy to the nano-particle has a thickness of around 3 nm. W, Cr, Y, and O are detected in the nano-particle. The measured concentration of W in the nano-particles is lower as compared to the measured concentration in the alloy. However, a reconstruction artifact explained in the following must be considered.

Reconstruction of the APT measurement to the 3D-image assumes a hemispherical shape of the tip. The nano-particles have a different ionization threshold as compared to the W alloy. The different ionization threshold results in a deviation of the spherical shape and the real surface as illustrated in Fig. 9.10. The ion trajectories are normal to the real surface. This deviation is not considered in the reconstruction and the reconstructed ion trajectories are normal to the assumed hemispherical surface. This artifact yields a misplacement of the reconstructed atom positions. A misplacement by 2 nm to 3 nm is possible.

Therefore, it is assumed that the measurement of W in the nano-particles is an artifact of the APT and that the approximate composition of the nano-particles is $YCrO_3$. Equivalent analysis yielding the same result is performed for the smaller nano-particles. The O concentration in the bulk of the alloy is below $1\,\text{at.\%}$. This finding is an indication that the nano-particles bind the O impurities from the alloy.

The concentration of Cr in the bulk, less than 100 nm from the interface to the protective Cr_2O_3, is inhomogeneous, as seen in Fig. 9.9 b. There are Cr-high regions with a Cr content of around $9\,\text{at.\%}$ and Cr-low regions with a Cr content of around $1\,\text{at.\%}$. A line scan across a grain boundary of grains with different Cr content is shown
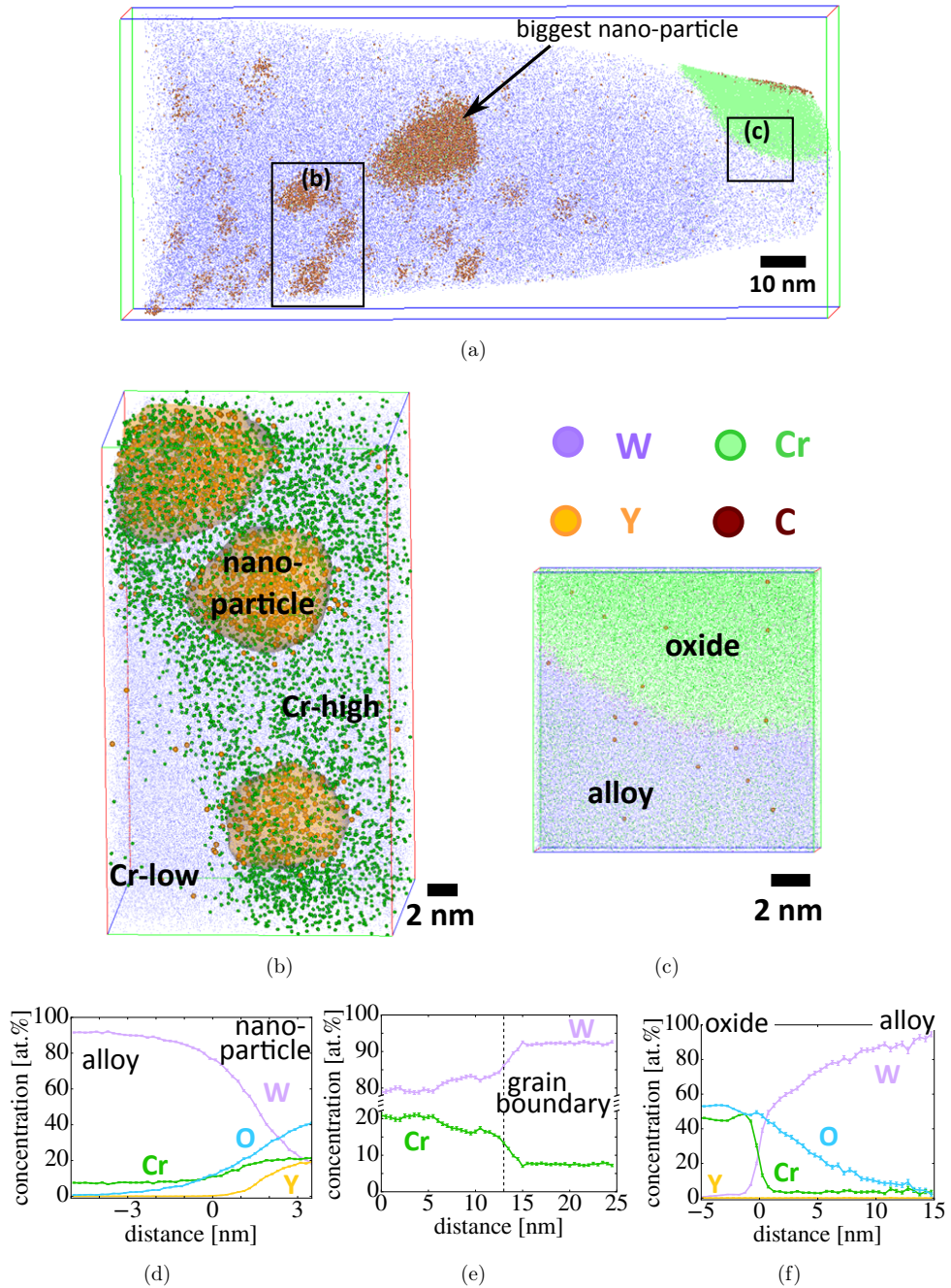
Figure 9.9: Results of the APT measurement in the alloy directly beneath the Cr_2O_3 scale. (**a**) the elemental distribution in an three dimensional overview image. (**b**) and (**c**) zoomins of the regions marked in (a). (**d**) the elemental composition in a proximity histogram around the biggest nano-particle, as labeled in (a). (**e**) the elemental concentrations in a proximity histogram across two different grains. (**f**) the elemental composition in a proximity histogram from the oxide to the alloy.

in Fig. 9.8 e, the transition occurs within 3 nm. Overall, the Cr content is reduced from the initial 31 at. % due to Cr consumption in the protective oxide layer.

The spatial resolution of the APT is much higher as compared to SIMS, where the concentration is averaged over a plane of $\sim 100\,\mu m$ by $100\,\mu m$ and has an depth uncertainty around $0.6\,\mu m$, see section 9.1.2. Therefore, the result of an inhomogeneous Cr distribution on a nanometer scale does not contradict the SIMS result of a homogeneous Cr distribution on a micrometer scale (see section 9.1.2).

The reduced Cr concentration near the interface (see Fig. 9.9) indicates that the Cr consumption by formation of the Cr_2O_3 is higher than the Cr supply by diffusion from the bulk of the alloy during the first 20 h of the oxidation process. The low Cr content in the alloy directly below the Cr_2O_3 decreases the ability to compensate local failures of the protective oxide and thus decreases the reliability of the protective function. However, as shown in section 8.2, the Cr supply is sufficient to maintain a continuously growing protective Cr_2O_3 layer at 1273 K.

A magnified view of the interface between the protective Cr_2O_3 and the alloy is shown in Fig. 9.9 c. No Y is detected at the interface. The transition from 0 at. % W in the oxide to 90 at. % W in the alloy occurs within less than 2 nm, as shown in the proximity histogram at the interface in Fig. 9.9 f. However, only one tip with an interface area of $\sim 0.02\,\mu m^2$ is analyzed. The STEM study (see section 9.2.1) detected one nucleation site on an interface area of $\sim 0.03\,\mu m$. Thus, the study is inconclusive on the frequency of nucleation sites. It is not clear whether nucleation sites are a peculiarity of thin film smart alloys or whether nucleation sites also occur in bulk smart alloys, just not on the analyzed tip. The author expects that the concept of nucleation sites (see section 9.2.3) works similar in bulk and thin film samples, thus APT analysis on more locations should show nucleation sites also on bulk samples.
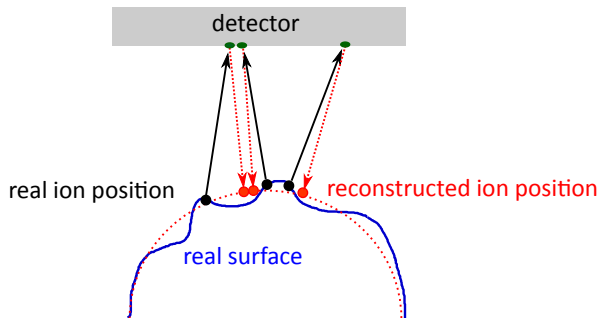
Figure 9.10: Sketch illustrating the reconstruction artifact when the real surface deviates from the hemispherical tip shape assumed for the reconstruction. The artifact is exaggerated in the sketch for clarity.

9.2.3 Discussion on the effect of yttrium

The beneficial effects of Y on the oxidation resistance of W-Cr alloys is already shown in section 5.2. When discussing the role of Y on the oxidation process, four parts are considered:

1. The diffusion of Cr and O ions in the oxide scale.

2. The diffusion of chromium in the metallic alloy.

3. Oxygen in the metallic alloy.

4. The adhesion of the oxide scale.

The diffusion of Cr and O ions in the oxide scale

Y agglomerates in a continuous film along the grain boundaries of the Cr_2O_3. Such a behavior is reported to decrease the diffusion flux of O and Cr through the oxide scale [45]. The mechanism is illustrated schematically in Fig. 9.11: Cr diffusion is the process of Cr ions moving from one vacancy to the other. Y occupies some of the vacancies and they are no longer available for Cr transport. This occupation has two consequences: first, the concentration of Cr ions is lower which reduces the flux. Second, the energy required for the movement of one vacancy to the other increases as a larger distance must be covered - the flux of ions is reduced further. An analogous behavior is expected for O ions and the oxidation rate is decreased. Further experimental and theoretical work is required in order to verify and refine this hypothesis.

The diffusion of chromium in the metallic alloy

The initial protective Cr_2O_3 layer forms from the Cr near the surface of the alloy. Continued oxidation causes an increase in thickness of the Cr_2O_3 layer. Cr from deeper in the bulk of the alloy must not only diffuse through the Cr_2O_3 layer as shown in section 9.1.1, but also to the interface of the oxide and the metal. Faster diffusion in the alloy is desirable as it allows more reliable replenishing of the protective Cr_2O_3 to suppress the formation of W oxides.

O impurities in W are reported to occupy interstitial sites [107]. The hypothesis is that O on interstitial sites in W yields a reduction of the Cr diffusion in the alloy as compared to an O-free alloy. The mechanism is illustrated in Fig. 9.11, it is the same mechanism as Y on the grain boundaries in the Cr_2O_3 layer. Y, Cr, and O agglomerate in nano-particles (see Fig. 9.9). Thus, unlike in the Cr_2O_3, Y does not occupy interstitial sites. Further, O which is in the nano-particle occupies no longer interstitial sites. Therefore, a lower occupation level of the interstitial sites as compared to an Y-free alloy is expected. A similar phenomena is discussed in [108], where the addition of Y is reported to purify a superalloy. This understanding yields to the hypothesis that the addition of Y decreases the number of occupied interstitials in the alloy which increases the diffusion of Cr in the alloy as compared to an Y free alloy. This model predicts that an increased O content as compared to the O content of the investigated alloy increases the number of occupied interstitials and decreases the oxidation resistance. Experimental confirmation of this prediction is given in section 8.3. Still, further experimental and theoretical work is required in order to verify and refine the understanding.

Oxygen in the metallic alloy

Oxygen in the metallic alloy causes occupation of interstitial sites and consumption of Cr for internal, non-protective oxidation. Both effects are not desirable, in particular the formation of W-containing oxides with large volumetric expansion degrades the oxidation resistance, as shown in section 7.1. The protective chromium oxide layer minimizes the penetration of O into the metal. Above, it was suggested that Y improves the
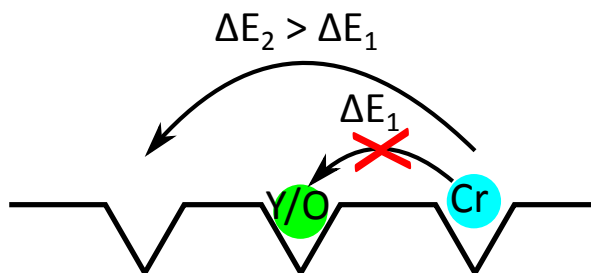
Figure 9.11: Simplified schematic of diffusion in the presence of impurities. Movement of Cr to the nearest vacancy requiring the energy ΔE_1 is blocked by Y or O. Movement to the next nearest vacancy requires a higher energy ΔE_2.

protective function of the oxide by minimizing the amount of interstitial O in the metal. A complementary hypothesis is that the nano-particles attract oxygen and purify the smart alloy also during oxidation. Such a purification process avoids the oxidation of W.

The adhesion of the oxide scale

Nucleation sites can promote the selective oxidation of Cr forming the protective oxide layer and suppressing the oxidation of W: the reaction of Y_2O_3 with Cr_2O_3 to form $YCrO_3$ has a standard Gibbs energy of $-2 \times 10^2 \, \mathrm{kJ \, mol^{-1}}$. $YCrO_3$ has a high oxygen vacancy concentration and thus offers a fast diffusion path for oxygen while blocking cation diffusion [109]. Such a behavior is expected to increase the adhesion of the oxide scale. Nucleation sites are detected on thin films (see Fig. 9.6 e), yet they are to be found in the case of bulk alloys.

More experimental and theoretical work is required on the field of adhesion of the oxide scale, open questions include the influence of the growth rate and the ratio Φ_{Cr}/Φ_O of Cr ion flux Φ_{Cr} and O ion flux Φ_O in the oxide layer. Current work presented in section 9.1.1 shows only $\Phi_{Cr} > \Phi_O$.

This subsection 9.2.3 is a compilation of plausible hypotheses on the effect of yttrium supported by experimental results and information from literature. The following list presents the key facts found in this chapter in order to avoid confusion between facts and hypotheses:

- The Cr_2O_3 grows primarily at the outermost surface (see section 9.1.1).

- A homogeneously distributed (αCr, W) phase with clusters not larger than a few tens of nm is acceptable (see section 9.1.2).

- After oxidation Cr is homogeneously distributed on a µm scale in the alloy (see section 9.1.2), while inhomogeneities are visible on a nm scale (see section 9.2.2).

- Y in thin films is distributed homogeneously on an atomic scale while Y enriched nucleation sites are detected at the interface to the Cr_2O_3 layer (see section 9.2.1).

- Y is found at the grain boundaries of the protective Cr_2O_3 (see section 9.2.2).

- All Y in bulk smart alloys is bound in nano-particles containing Y, Cr, and O (see section 9.2.2).

Chapter 10

Modeling of W-Cr-Y alloys

Extensive modeling is performed in the field of High Entropy Alloys (HEA) [110]. These models are applied on the W-Cr-Y alloys presented in this thesis in order to develop a mathematical description of the W-Cr-Y alloys. HEA are introduced in section 10.1 while section 10.2 presents the modeling results on smart alloys.

10.1   Introduction to high entropy alloys

The term HEA refers to alloys with multiple principle elements which are all present in a roughly equal atomic composition. A HEA may contain four or five up to twenty different elements. There should be one dominant solid solution phase [111].

Classical alloy development usually starts with one base material which has certain desirable properties. In case of the oxidation resistant alloys presented in this work, the base material is W. However, this base material has properties which require improvement - for example the oxidation resistance. Alloying elements are added to the material in order to improve the properties of the material while keeping the advantageous properties of the base material. In this work Cr and Y are added. The largest fraction of the material remains the base element and the composition of the alloying elements is adjusted in order to achieve optimized parameters. Such an approach yields to well explored edges in the phase diagrams, but little knowledge to the center of the phase diagram where multiple elements are present in equal fractions.

The concept of HEA offers a fundamentally different starting point for alloy development. Mixing multiple elements in equal atomic composition may yield new material properties and opens the field to less explored regions in a phase diagram [112]. Computation of the short range order (SRO) as pair correlation of the atoms is an important tool to predict the phase stability [111]. The SRO is introduced in section 10.2.

There is a very large compositional space for new HEA and it is impossible to fabricate all options. Therefore, materials modeling and computational alloy design are indispensable tools for investigations [113]. The first aim is to predict which elements form a stable, single solid solution phase (or two-phase solid solution) when alloyed in equal atomic composition [113]. The exact composition is only adjusted, once a promising combination of four, five, or more elements in equal atomic composition is found. Simulations can be extended to thermodynamic, microstructural, and mechanical properties [113].

In general a system tries to minimize its energy and to maximize its entropy. In the

case of HEA each atom aims to occupy a position of minimum site and bonding energy. These energies depend on the local chemical environment, inter-atomic interactions, and atomic volumes of the constituent elements [111]. The entropy of a system increases with random mixing. The configurational entropy per mole (S_{conf}) due to the formation of a solid solution from n elements with equal atomic composition is given by

$$S_{\mathrm{conf}} = -k \ln w = k N_A \ln n \qquad (10.1)$$

where k is the Boltzmann constant, N_A is the Avogadro constant, and w is the number of ways of mixing [112]. This entropy change stabilizes the solid solution.

Simulation and modelling of HEA can be performed using prior experimental knowledge or ab-initio methods:

- The atomic size difference of the contained elements is one important prior experimental knowledge. This difference can be expressed in a parameter δ and the mixing enthalpy ΔH_{mix} is calculated based on the regular melt model [114]. Such calculations allow predictions whether a solid solution forms with a certain elemental composition. More reliable simulations include various other thermodynamic properties [113].

- Ab-initio methods are based on the density functional theory (DFT). The many-body Schrödinger equation is solved to calculate electronic wave functions and extract properties of the material. A cluster expansion (CE) method can be employed to write the enthalpy of mixing of the multicomponent alloy in the form of an Ising-like Hamiltonian [110].

Various HEA alloys were manufactured and showed promising properties:

- Cantor et al. [115] in 2004 were among the first to fabricate a HEA. It is shown that the five-component alloy $Fe_{20}Cr_{20}Mn_{20}Ni_{20}Co_{20}$ forms a single solid solution phase which can dissolve transition metals such as Nb, Ti, and V. The indices give the atomic composition, i.e. the aforementioned alloy contains 20 at. % of each element.

- Yeh et al. [112] fabricated CuTiVFeNiZr, AlTiVFeNiZr, MoTiVFeNiZr alloys among others and showed that the hardness after annealing for 12 h at 1273 K remains constant as compared to the as-cast hardness.

- Daoud et al. [116] investigated the oxidation resistance of HEA. Cr or Al content appears to be required for a good oxidation resistance [113], as Cr or Al are capable of forming a protective oxide layer - the mechanism is the same as compared to other alloys. $Al_{17}Co_{17}Cr_{17}Cu_{17}Fe_{17}Ni_{17}$ alloys exhibit oxidation resistance in air - the parabolic oxidation rate is $1 \times 10^{-7}\,\mathrm{mg}^2\,\mathrm{cm}^{-4}\,\mathrm{s}^{-1}$ at a temperature of 1073 K [116].

- El-Atwani et al. [117] manufactured $W_{38}Ta_{36}Cr_{15}Ta_{11}$ alloys and demonstrated their outstanding radiation resistance. The mobilities of vacancies and self-interstitials are similar. This fact maximizes recombination and reduces the defect concentration. Therefore, no signs of radiation-induced dislocation loops are found.

- The author of this thesis prepared $W_{22}Cr_{26}Ta_{25}V_{27}$ HEA using the magnetron device. The alloy consists of a dominant solid solution phase, but shows poor oxidation resistance despite the fairly high Cr content. Further research is ongoing and the results are to be published elsewhere.

HEA are a new field of research aiming to develop alloys with excellent mechanical properties and a high radiation resistance. Further, HEA are a model system for computational alloy development contributing to a new level of understanding of alloys. In this thesis, the aim is to use the knowledge for developing a mathematical description of oxidation resistant W-Cr-Y smart alloys.

10.2 Understanding of W-Cr-Y alloys using knowledge from HEA

The ab-initio modelling methods in the field of HEA are versatile and designed to be applied to any potentially new HEA. Thus, it is also possible to insert the composition of the optimized, oxidation resistant W-Cr-Y alloys. This calculation is presented in this section, providing an enhanced understanding of the observed processes in the alloy and providing the base for future computational optimization of the alloy.

The free energy of formation F of an alloy must be minimized for a stable configuration. In basic thermodynamics F is given by the equation

$$F = H_{\text{mix}} - T(S_{\text{conf}} + S_{\text{vibr}} + S_{\text{elec}} + S_{\text{mag}}) \qquad (10.2)$$

where T is the temperature, and S_{conf}, S_{vibr}, S_{elec}, S_{mag} are the configurational, phonon, electron, and magnetic entropies, respectively. H_{mix} is the enthalpy of mixing. A negative H_{mix} between two components in a multi-component alloy yields a low free energy F. Therefore, a negative H_{mix} indicates that these two components form an intermetallic phase instead of going into a solid solution. On the contrary, a positive H_{mix} between two components in a multi-component alloy yields a high free energy F. Therefore, these components repel each other which inhibits a solid solution. Consequently $H_{\text{mix}} \approx 0\,\text{eV/atom}$ between each two components is ideal for forming a solid solution in a multi-component alloy.

In the Cluster Expansion (CE) method H_{mix} is associated with the configuration of the atoms and written as an Ising-like Hamiltonion:

$$H_{\text{mix}} = \sum_{\omega} J_{\omega} m_{\omega} \langle \Gamma_{\omega'}(\overrightarrow{\sigma}) \rangle. \qquad (10.3)$$

J_{ω} are the effective cluster interactions corresponding to cluster ω; m_{ω} is the multiplicity corresponding to the number of clusters equivalent to ω by symmetry; $\overrightarrow{\sigma}$ is the configurational variable specifying the atomic configuration; $\langle \Gamma_{\omega'}(\overrightarrow{\sigma}) \rangle$ is the cluster function. The cluster function is the product of point functions of occupation variables.

The optimum number and configuration of the clusters are benchmarked using first principle density functional theory (DFT). DFT and CE calculations must yield the same H_{mix} [110]. The cluster functions are required for further calculations discussed later in this section.

The present section investigates the ternary W-Cr-Y alloy. There are three components and the occupation variables $\gamma_j(\sigma_i)$ are defined by

$$\gamma_j(\sigma_i) = \begin{cases} 1 & \text{if } j = 0 \\ -\cos(2\pi \lceil \frac{j}{2} \rceil \sigma_i / 3) & \text{if } j > 0 \text{ and odd} \\ -\sin(2\pi \lceil \frac{j}{2} \rceil \sigma_i / 3) & \text{if } j > 0 \text{ and even} \end{cases} \qquad (10.4)$$

which allows to calculate the cluster function

$$\langle \Gamma_{|\omega|,m}^{ijk}(\overrightarrow{\sigma}) \rangle = \sum_{pqr} \gamma_i(\sigma_p) \gamma_j(\sigma_q) \gamma_k(\sigma_r) y_m^{pqr} \qquad (10.5)$$

where y_m^{pqr} is probability of finding the atomic species p,q,r located at the atomic configuration m. m is an integer numbering the atomic configurations.

The results of these calculations are shown in Fig. 10.1 a-c. The calculations are performed for different alloy compositions at different configurations. Different configurations are needed as DFT input into the Cluster Expansion model in order to predict the low energy configurations. Thus, for a thermodynamically stable configuration, the enthalpy of mixing is given by the lowest value at the given elemental composition. The higher values for the enthalpy of mixing relate to non-stable configurations, but are necessary for the construction of the CE model. As shown in Fig. 10.1 a-c, the DFT data and the CE points predict almost the same values, which confirms that the CE is constructed successfully.

Based on the calculated enthalpies H_{mix} and the cluster functions, short range order (SRO) parameters can be calculated and exchange Monte Carlo (MC) simulations can be performed. The SRO parameters describe the occupational deviations from the average random configuration at a local atomic scale. The MC simulations predict the stability of the alloys and result in structure images, as shown in Fig. 10.2.

Short range order parameters The Short Range Order (SRO) is described as pair correlation by the parameter

$$\alpha_{2,m}^{p,q} = 1 - \frac{y_m^{pq}}{c_p c_q} \tag{10.6}$$

where c_i is the average atomic concentration of atom species i and y_m^{pq} is defined as above - the probability of finding the atomic species p,q located at the atomic configuration m [111]. In the case that the atoms are randomly distributed, the probability y_m^{pq} is given by $c_p c_q$. The configuration that an atom of species p is located at a specific position and an atom of species q is the nearest neighbor of that atom is described. Thus, a random distribution of atoms results in $\alpha_{2,1}^{p,q} = 0$. In the case that atoms of the same species are preferentially nearest neighbor of each other $\alpha_{2,1}^{p,q} > 0$. In the case that atoms of different species are preferentially nearest neighbor of each other $\alpha_{2,1}^{p,q} < 0$.

W and Cr have a body-centered cubic (bcc) lattice structure [118] and the SRO parameters of $W_{70}Cr_{29}Y_1$ are calculated for a bcc lattice structure. The distance between the nearest neighbors and the distance between the second nearest neighbors differs by only 13 %. Therefore, the SRO parameter are averaged over the first and second nearest neighbors. The averaged SRO α_{1+2} is given by

$$\alpha_{1+2} = \frac{z_1 \alpha_{2,1}^{p,q} + z_2 \alpha_{2,2}^{p,q}}{z_1 + z_2} \tag{10.7}$$

where $z_1 = 8$ and $z_2 = 6$ are the number of first and second nearest neighbors, respectively.

The result of this calculation for a $W_{50}Cr_{50}$ alloy is plotted in Fig. 10.1 e. At low temperatures $\alpha_{1,2} > 0$ is found which predicts the formation of two phases, one Cr rich and one W rich phase. α_{1+2} decreases to 0 in the temperature range from 1000 K to 2000 K. Thus, starting from a temperature of around 2000 K a solid solution is predicted. These results are in agreement with the phase diagram shown in Fig. 1.2 b where a solid solution of $W_{50}Cr_{50}$ is found starting from a temperature of 1950 K, a deviation of less than 3 % from the calculated temperature.

After successful benchmarking of binary calculations with experimental results, the calculation is performed for the ternary smart alloys. The calculated SRO parameters for the $W_{70}Cr_{29}Y_1$ alloy are plotted in Fig. 10.1 d. At temperatures below 1000 K $\alpha_{1+2} > 0$ is calculated for all pairs of contained species. This result indicates that the atoms

segregate into 1-atom-type clusters, i.e. Y particles, a Cr rich phase, and a W rich phase are predicted.

$\alpha_{1+2} > 0$ remains valid for the W-Y and Cr-Y pairs up to 3000 K and Y particles are expected to be stable beyond the melting point of Y which is at 1795 K [119].

α_{1+2} for W-Cr drops towards 0 in the range of 750 K to 1500 K and remains at 0 for higher temperatures. This results indicates that W and Cr in the given elemental composition form a solid solution starting from 1500 K. In comparison, the experimental, binary phase diagram shown in Fig. 1.2 b shows a solid solution of $W_{70}Cr_{30}$ starting from 1820 K. Based on this result, the addition of Y appears to stabilize the W-Cr phase resulting in a solid solution down to lower temperatures and in an increased solubility of Cr in W at a given temperature.

Stabilization of the microstructure due to addition of Y is know as Zener pinning for decades [121]. The presence of grain boundaries is crucial for Zener pinning. However, the ab-initio modeling does not consider grain boundaries. Therefore, a phase stabilization due to the addition of Y appears also independently on the microstructure: the addition of Y keeps more Cr in solid solution with W which is expected to increases the mobility of Cr in the metallic alloy. A higher mobility of Cr in the metallic alloy allows more efficient
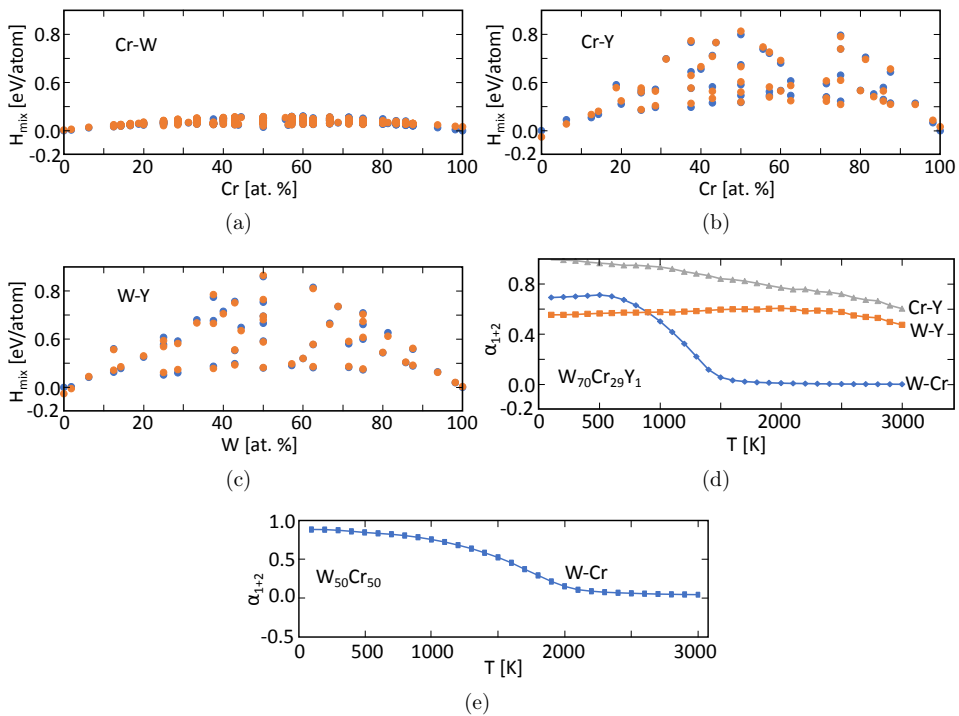
Figure 10.1: (**a**)-(**c**) The calculated enthalpy of mixing H_{mix} for all possible pairs in the W-Cr-Y system as a function of the elemental composition. The blue dots are based on DFT calculations while the orange dots are calculated via CE. (**d**) The calculated average short range order (SRO) for the different pairs in a $W_{70}Cr_{29}Y_1$ alloy as a function of temperature. (**e**) The calculated average SRO for W-Cr pairs in a $W_{50}Cr_{50}$ alloy as a function of temperature. Simulations were performed by J. S. Wróbel [120].

replenishing of the protective oxide layer resulting in a better oxidation resistance.

The calculations assume metallic yttrium and do not consider oxygen. However, the manufactured samples always show O in the vicinity of the Y. Future studies should validate this simplification and investigate how O in the material changes its properties. Studies are ongoing and are to be published elsewhere.

Monte Carlo simulations Exchange Monte Carlo (MC) simulations show the elemental distribution in three dimensions which form due to diffusion processes. Input parameters are the effective cluster interactions J_ω, the enthalpy of mixing H_{mix} as given in equation 10.3, and the body centered cubic crystal structure. The starting condition is that a fixed number of each kind of atoms is randomly distributed within an analysis volume at a temperature of 3000 K.

The elemental distributions when cooling to 1200 K, 900 K, 600 K, and 300 K are shown in Fig. 10.2. Clustering of Y atoms is predicted at all investigated temperatures. At 1200 K Cr starts to form clusters in the simulation volume, see Fig. 10.2 a. Increased clustering of Cr is found at 900 K and below. Typically the Cr clusters are found at the edge of the simulation volume, see Fig. 10.2 b-d. The center of the modeled Cr clusters is pure Cr while Cr and W are mixed at the edge of the Cr clusters. These results are in good agreement with the prediction based on the results from the short range order calculation shown in Fig. 10.1 d.

| (a) 1200 K | (b) 900 K | (c) 600 K | (d) 300 K |
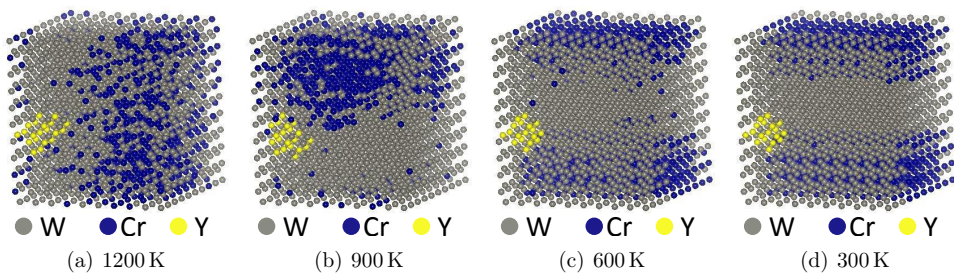
Figure 10.2: The calculated elemental distribution in a $W_{70}Cr_{29}Y_1$ alloy based on a Monte Carlo simulation. Starting point of the simulation is a completely random distribution. The distribution during the cooling process is shown at a temperature of (**a**) 1200 K, (**b**) 900 K, (**c**) 600 K, and (**d**) 300 K. Simulations were performed by J. S. Wróbel [120].

Comparison with the experiment The microstructure of the alloy after 3 weeks at 1273 K is shown in Fig. 10.3. After the heat exposure the sample is cut and polished. This allows imaging several millimeters away from the surface where the phase formation is not dominated by the formation of Cr_2O_3. Separate Y-Cr-O nano-particles are detected and a Cr-rich phase is found, see Fig. 10.3. This result is in qualitative agreement with the modeling results shown in Fig. 10.2 even though the nano-particles in the experiment contain also Cr, see section 9.

This agreement underlines that the simulations can provide a basic understanding of the alloy, despite multiple simplifications: O is not considered in the modeling, grain boundaries are neglected, and the simulation volume is limited.

Interesting questions for further research are to include O, how the grain boundaries can be included into the model and whether modeling can predict new alloying elements

which stabilize the main W-Cr phase further.
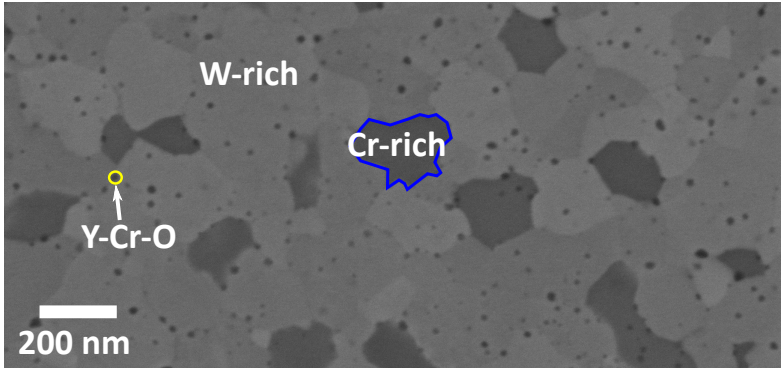
Figure 10.3: Microstructure of a $W_{67}Cr_{32}Y_1$ (W-11.4Cr-0.6Y) alloy after 3 weeks at 1273 K several millimeters away from the surface. The microstructure before heat exposure is shown in Fig. 6.3 e.

Overall, the presented first results on modeling of W-Cr-Y alloys provide new insights into the understanding of smart alloys:

- The addition of Y increases the solubility of Cr in W. This effect could be important for the improved oxidation resistance in the presence of Y.

- Y repels W and Cr and tends to form clusters. This finding is only in partial agreement with the experiment.

- Phase separation of W and Cr in a $W_{70}Cr_{29}Y_1$ alloy is expected below 1500 K. The kinetics of the phase separation are not yet investigated. Experimentally phase separation is observed at 1273 K. No measurements between 1273 K and 1500 K were conducted.

Chapter 11

Zr as an alternative active element to Y in the W-Cr alloy

The previous chapters 5 to 10 focused on W-Cr-Y alloys. The oxidation mechanisms are studied and the importance of Y for the oxidation resistance is discussed in detail. However, it is an open question whether new alloying elements can improve the oxidation resistance further. One candidate is the active element Zr used for instance in [122, 123, 124] and showing promising properties.

Zr is reported to have similar effects as Y: the adherence of the protective oxide layer is increased; impurities such as sulfur (S), carbon (C), and oxygen (O) are bound due to the high affinity of Zr; the grain growth in the alloy is inhibited [40]. Further, Zr has a low Pilling-Bedworth ratio of 1.56 and a high melting point of above 2100 K [40].

This chapter presents first investigations on Zr containing smart alloys using the same methods as presented in chapters 5 to 7. Ternary W-Cr-Zr alloys without Y are investigated in order to see the pure effects of Zr. Investigations of quaternary W-Cr-Y-Zr alloys addressing correlative effects of different active elements are a topic of future studies. C. Lenser investigated quaternary W-Si-Cr-Y, W-Si-Cr-Zr, and W-Si-Cr alloys [125]. He found that the addition of both Y and Zr improve the oxidation resistance.

This chapter is divided in two sections. Section 11.1 investigates W-Cr-Zr thin films deposited by magnetron sputtering. Section 11.2 investigates W-Cr-Zr bulk alloys sintered by FAST. The data presented and discussed in the section 11.1 is already published by X. Y. Tan, F. Klein et al. [126]. The work was performed in close collaboration. The author of this thesis introduced X. Y. Tan to all the employed methods and showed how to use the devices: the magnetron (see section 2.1), the XRD (see section 2.10) and the TGA (see section 2.16). The shown experiments were conducted partially by X. Y. Tan and partially by the author of this thesis. Sample production was performed by X. Y. Tan. Electron microscopy images are taken by the author of this thesis. Data analysis, understanding, and planning of the experiments are the result of the input from X. Y. Tan, the author of this thesis and the other authors of the aforementioned publication [126].

11.1 W-Cr-Zr thin films

11.1.1 Pre-characterization of the films

The samples investigated in this section are thin films deposited by magnetron sputter deposition on sapphire substrates with a diameter of 1.1 cm. Details on the magnetron device and the sputtering process are given in section 2.1 and 5.1. As compared to the procedure used in section 5.1, Y is substituted by Zr and the rotation speed is reduced from 5 rotations/min to 1.7 rotations/min for technical reasons.

A cross section and a surface image of a W-11.2Cr-1.7Zr film is shown in Fig. 11.1 a. The thickness measured on the full cross section is 3.9 μm. A density of 15.4 g cm^{-3} is calculated using the thickness and the mass of the film combined with the surface area of the substrate. The main characteristics are the same as for the W-Cr-Y films: the grain size is around 0.2 μm; no phase separation, no segregation of specific elements, and no oxide segregation are detected using XRD and SEM on a cross section. The main difference as compared to the W-Cr-Y films (discussed in chapter 5) is that the periodic lines of deposition increased from 7 nm (not visible in the cross section but in the STEM analysis in section 9.2.1) to 21 nm which is resolved in the cross section. In both cases the material from one line to the next is deposited within one rotation of the table on which the substrates are placed during sputtering.

The XRD measurement is shown in Fig. 11.1 b. Peaks as expected for a W crystal are detected. The peak positions are given in table 11.1, within the uncertainty given by the FWHM the peak positions are the same as the peak positions measured on W-Cr-Y films also included in the table. The differences in the peak positions are much smaller than the peak widths and the findings from the XRD on W-Cr-Y presented in chapter 5 are identical to the ones on the W-Cr-Zr diffractogram.

Based on these findings it can be concluded that the substitution of Y by Zr is performed successfully. The samples can be used for oxidation tests.

Table 11.1: Measured positions of peaks in the XRD shown in Fig. 11.1 b compared to the results given in chapter 5, table 5.1. The Full-Width-Half-Maximum (FWHM) for the peaks of the W-Cr-Zr films is also given.

	(110)-Plane	(200)-Plane	(211)-Plane	(220)-Plane
W-Cr-Zr	40.4°	58.0°	73.4°	87.1°
W-Cr-Zr, FWHM	0.9°	1.2°	2.0°	1.8°
W-Cr-Y from table 5.1	40.4°	57.8°	73.1°	87.1°
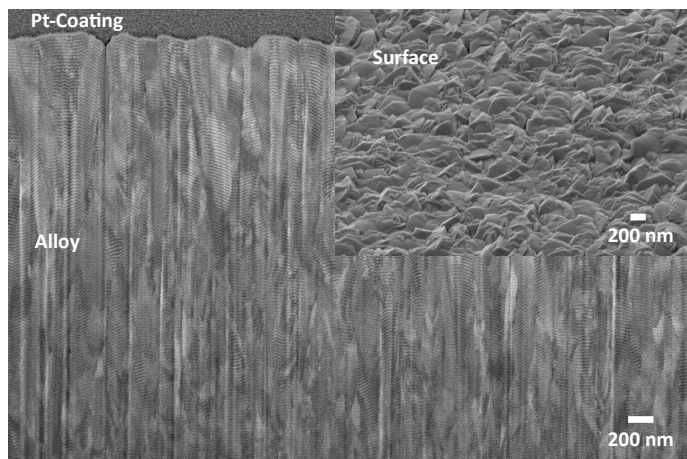
(a)
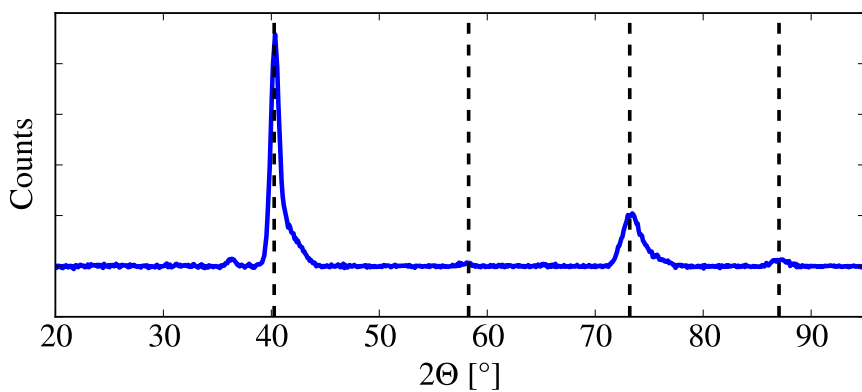
(b)

Figure 11.1: (**a**) SEM image of a W-11.2Cr-1.7Zr alloy deposited by magnetron sputtering. There is a cross section view showing the Pt coating and the alloy and a surface image in the inset. (**b**) Result of a XRD measurement on the sample depicted in (a). The vertical, dashed lines indicate the expected peak positions for W [81].

11.1.2 Oxidation behavior of the films

The oxidation process of W-Cr-Zr thin film alloys is studied at a temperature of 1273 K in 80 % Ar and 20 % O_2 atmosphere at atmospheric pressure. In a first step the elemental composition is varied. The mass change as a function of time is plotted in Fig. 11.2 a. The composition is varied in the range of 9.6 wt. % Cr to 12.5 wt. % Cr and 0.6 wt. % Zr to 3.6 wt. % Zr while W constitutes the remaining fraction. All samples start with mass gain following a parabolic rate law during the $\sim$ 0.5 h and change to a linear oxidation kinetics. W-12.5Cr-0.6Zr exhibits the highest mass gain rate at $2.5 \times 10^{-5}\,\mathrm{mg\,cm^{-2}\,s^{-1}}$ while W-11.2Cr-1.7Zr exhibits the lowest rate at $1.5 \times 10^{-5}\,\mathrm{mg\,cm^{-2}\,s^{-1}}$. Overall, Zr seems to be required in a slighly higher concentration as compared to Y in order to achieve the optimum oxidation resistance. In comparison, a linear approximation of the W-12Cr-0.5Y oxidation kinetics, which is included in Fig. 11.2 a yields a slightly lower rate of $1.0 \times 10^{-5}\,\mathrm{mg\,cm^{-2}\,s^{-1}}$.

The most promising alloy W-11.2Cr-1.7Zr is chosen for further studies. The oxidation time is increased to 10 h while all other oxidation conditions are kept constant. The mass change as a function of time is shown in Fig. 11.2 b. The W-11.2Cr-1.7Zr alloy drops to an oxidation rate of $1 \times 10^{-5}\,\mathrm{mg\,cm^{-2}\,s^{-1}}$ during the 10 h of oxidation while the rate of W-12Cr-0.5Y increases to a linear mass gain of $5 \times 10^{-5}\,\mathrm{mg\,cm^{-2}\,s^{-1}}$.

XRD measurements of the W-11.2Cr-1.7Zr alloy after oxidation for 1.25 h and 10 h are shown in Fig. 11.3. In both cases W peaks remain visible which indicates that the oxide layer on the surface is sufficiently thin for the X-rays to penetrate. The specific thickness is determined in the cross sections shown in Fig. 11.4. Cr_2O_3 is the only oxide detected by the XRD measurement in case of oxidation for 1.25 h. After 10 h of oxidation Cr_2O_3 remains the dominating oxide. In addition, small peaks corresponding to W-containing oxides Cr_2WO_6 and WO_3 appear.
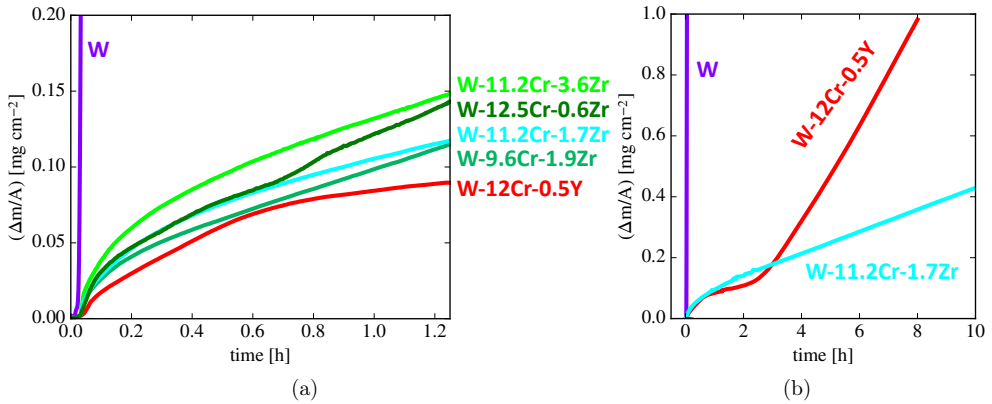
Figure 11.2: Mass gain due to oxidation of magnetron-deposited thin films as a function of time. Oxidation is performed at 1273 K in 80 % Ar and 20 % O_2 atmosphere at atmospheric pressure. The elemental composition of the samples is given in the labels in weight %. The oxidation time is 1.25 h in (**a**) and 10 h in (**b**).
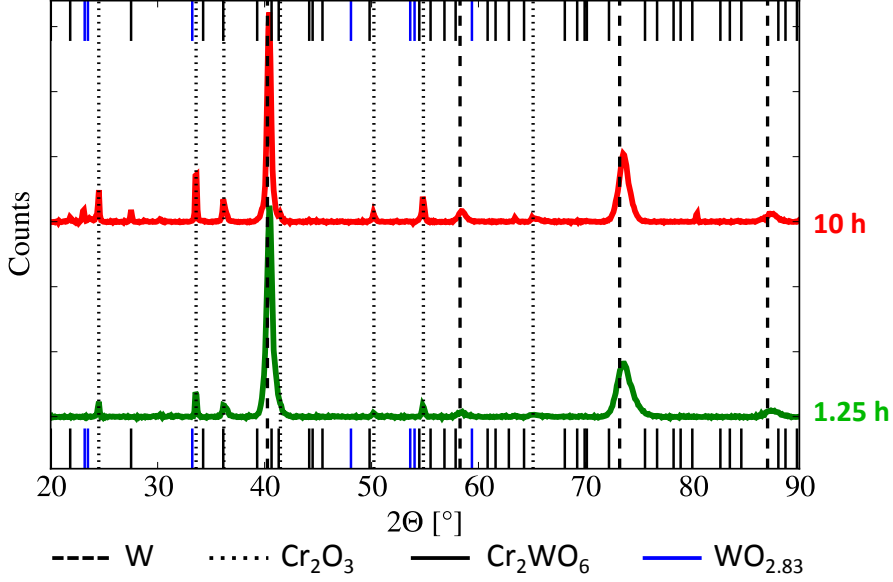
Figure 11.3: Results of XRD measurements on W-11.2Cr-1.7Zr alloys after oxidation at 1273 K in 80 % Ar and 20 % O_2 atmosphere at atmospheric pressure. One sample is oxidized for 1.25 h, the other is oxidized for 10 h. Peak positions for W [81], Cr_2O_3 [94], Cr_2WO_6 [95], and $WO_{2.83}$ [127] are marked.

The cross sections corresponding to the samples analyzed in the XRD in Fig. 11.3 are shown in Fig. 11.4. After 1.25 h of oxidation a 0.3 μm thick Cr_2O_3 layer is found on the surface, as shown in Fig. 11.4 a. Internal oxidation is found within the first 2 μm from the interface of the alloy and the oxide. The alloy layer has a thickness of 3.9 μm, which is constant compared to the thickness of the film before oxidation.

After 10 h of oxidation the thickness of the protective Cr_2O_3 layer increases to 1 μm, as shown in Fig. 11.4 b. W-containing oxides, identified using the EDX in combination with the XRD measurement shown in Fig. 11.3, are found at small, localized spots as marked in Fig. 11.4 b. Internal oxidation and pores originating from material diffusing to the surface are found throughout the entire film. Internal oxides are identified by a darker color in the image; pores are identified by a white border in Fig. 11.4 b. The thickness of the alloy layer decreased by 0.1 μm to 3.8 μm. The cross section and the XRD measurement are done in the center of the sample. The photograph in the inset of Fig. 11.4 b shows a green color in the center of the sample and a black color at the edge. This observation indicates that a cross section in the center is not representative for the edge of the sample where the adhesion of the film to the substrate and the oxide to the alloy is weaker as compared to that in the center.

The most stable oxides of Cr and Zr are Cr_2O_3 and ZrO_2 with Gibbs free energies for the reaction with O_2 of $\Delta G_{Cr_2O_3}^{T=1273\,K} = -5.3 \times 10^2\,kJ/(mol\,O_2)$ [41] and $\Delta G_{ZrO_2}^{T=1273\,K} = -8.6 \times 10^2\,kJ/(mol\,O_2)$, respectively. The Gibbs free energy of the reaction of W to WO_3 is $\Delta G_{WO_3}^{T=1273\,K} = -3.6 \times 10^2\,kJ/(mol\,O_2)$, which is higher as compared to the aforementioned energies for the oxidation of Cr and Zr. Thus, Cr and Zr oxidize preferentially to W if access to O is provided.

Internal oxides are present in the entire film. Formation of internal oxides requires the

(a) 1.25 h   (b) 10 h
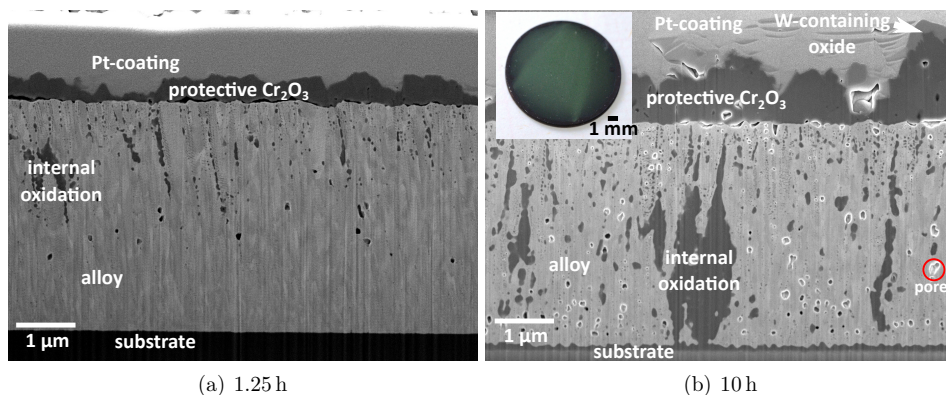
Figure 11.4: Cross sections of W-11.2Cr-1.7Zr alloys after oxidation at 1273 K in 80 % Ar and 20 % O_2 atmosphere at atmospheric pressure. (**a**) shows the sample after 1.25 h of oxidation while (**b**) shows it after 10 h of oxidation. The inset in (**b**) shows a photograph after 10 h of oxidation.

presence of O. Thus, access to O is provided to the elements in all parts of the alloy. The oxygen partial pressure must be in the range of 1×10^{-22} bar to 1×10^{-14} bar - the lower boundary is given by the partial pressure required for the formation of Cr_2O_3 which is detected; the upper boundary is given by the partial pressure required for the formation of WO_3 which is not detected.

The total initial weight of the W-11.2Cr-1.7Zr alloy shown in Fig. 11.4 b before oxidation is 6.66 mg. Thus, it contains 0.75 mg of Cr and 0.11 mg of Zr. The reaction of 0.75 mg of Cr to Cr_2O_3 and 0.11 mg of Zr to ZrO_2 causes a mass gain of 0.34 mg and 0.04 mg as O is added to the material. Normalized to the surface area of the sample, a total mass gain of 0.34 mg cm^{-2} is expected if all contained Cr and Zr reacted to their oxides. However, as shown in Fig. 11.2 b the mass gain after 10 h of oxidation is 0.43 mg cm^{-2}. This calculation combined with the presented measurements allow multiple conclusions:

- Most Cr and Zr contained in the alloy has oxidized.

- A constant oxidation rate is found beyond the point of almost full oxidation of Cr and Zr, see Fig. 11.2, and the formation of W-oxides is suppressed in the center of the sample: the protective oxide layer maintains its protective function despite not being replenished anymore. This finding is major difference as compared to W-Cr-Y alloys where W starts to oxidize as soon as the protective oxide is not replenished anymore, see chapter 5. Thus, Zr appears to be very efficient in stabilizing the protective oxide layer.

- A mass gain of at least 0.09 mg is caused by the oxidation of W. This corresponds to 0.34 mg of W, 6 % of the W contained in the film. However, the cross section shown in Fig. 11.4 b proves that the oxidation of W is suppressed in the center of the sample. Thus, oxidation of W must occur at the edge of the sample where the adhesion of the protective oxide layer is weaker - this effect causes the color change of the oxide at the edge of the sample, see Fig. 11.4 b.

- The W-11.2Cr-1.7Zr alloy shows a very promising oxidation resistance.

11.1.3 On the influence of Zr

From the cross sections shown in the previous section it is clear that Cr acts as protecting element and forms the protective Cr_2O_3 layer. Zr is crucial in the oxidation process as the oxidation resistance of binary W-Cr alloys is much weaker, see chapter 5. However, Zr is not resolved and its role in the protection process is not clear. A dedicated experiment is performed attempting to clarify the role of Zr.

Two types of samples are deposited by magnetron sputtering. The first type is a pure Cr sample with a thickness of $2.2\,\mu m$ on a sapphire substrate. The second type is shown and illustrated in Fig. 11.5 a: a $2.2\,\mu m$ thick layer of Cr on the sapphire substrate is coated by $0.15\,\mu m$ thick layer of Cr-9Zr using the magnetron.

Both samples are oxidized at $1273\,K$ in $80\,\%$ Ar and $20\,\%$ O_2 atmosphere at atmospheric pressure. The mass gain as a function of time is shown in Fig. 11.5 b. Parabolic oxidation rates of $2.8 \times 10^{-5}\,mg^2\,cm^{-4}\,s^{-1}$ and $1.2 \times 10^{-6}\,mg^2\,cm^{-4}\,s^{-1}$ are found for Cr and Cr-9Zr coated Cr, respectively.

This result indicates that the presence of Zr decreases the permeability of Cr oxide layers for Cr and O ions. Thus, one can assume that the protective Cr_2O_3 layers shown in Fig. 11.4 contain small amounts of Zr yielding the good oxidation resistance of the samples. Future studies on the mechanisms involving Zr could analyze the protective oxide layer using APT, similar to the study presented in section 9. Such a study allows predictions whether Y and Zr have similar functions improving the oxidation resistance or whether different mechanisms are involved.
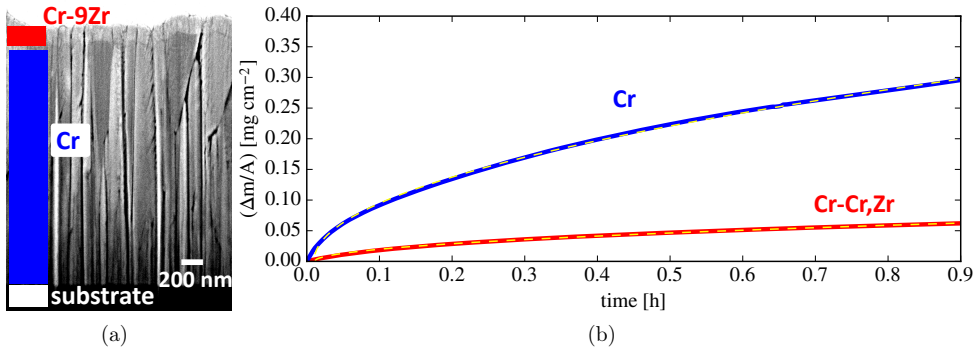
Figure 11.5: (**a**) Cross section and schematic illustration of the magnetron deposited Cr layer coated with Cr-9Zr by magnetron sputter deposition. This sample is referred as Cr-Cr,Zr. (**b**) Mass gain due to oxidation of magnetron-deposited thin films as a function of time. Oxidation is performed at $1273\,K$ in $80\,\%$ Ar and $20\,\%$ O_2 atmosphere at atmospheric pressure.

11.2 W-Cr-Zr bulk alloys

11.2.1 Pre-characterization of the sintered alloy

In section 11.1 a very promising oxidation resistance of W-11.2Cr-1.7Zr films deposited by magentron sputtering is shown. Therefore, bulk W-11.2Cr-1.7Zr alloys are sintered, aiming to understand whether the same mechanisms apply for the oxidation process of bulk samples and thin films. In a first step milling, sintering, and grinding follow the routine optimized on the W-11.4Cr-0.6Y system as presented in chapter 7: 60 h of mechanical alloying followed by sintering at a pressure of 50 MPa while heating at a rate of 200 K min^{-1} to 1740 K followed by an immediate cooling at a rate of 300 K min^{-1}. The obtained sample is cut into cubes with a width of ~ 4 mm and ground with a surface finish of P1200-grade SiC paper. A relative density of 98 % is measured using Archimedes principle.

Fig. 11.6 a shows the microstructure of the sintered alloy. The grain size is around 0.3 µm with 0.05 µm ZrO$_2$ particles at the grain boundaries. As compared to the W-Cr-Y alloys investigated in chapter 7 this corresponds to a medium grain size. The size of the Zr containing particles is doubled as compared to the Y-Cr-O nano-particles - however, there is also three times more Zr than Y in the alloy. No Cr-rich phases or pores are detected in the cross section.

The result of the XRD measurement is shown in Fig. 11.6 b. The diffractogram is almost identical to the one of W-Cr-Y shown in Fig. 6.4: the main phase gives rise to three peaks which are characteristic for a body-centered-cubic lattice. Alloying shifts their position μ from the expected peak position of pure W which is marked in Fig. 11.6 b. Further, a peak due to the secondary K_β X-ray wavelength and a peak from a Cr-rich phase are detected. Peak positions μ and width σ in a Gaussian Fit are given in table 11.2.

(a)

(b)
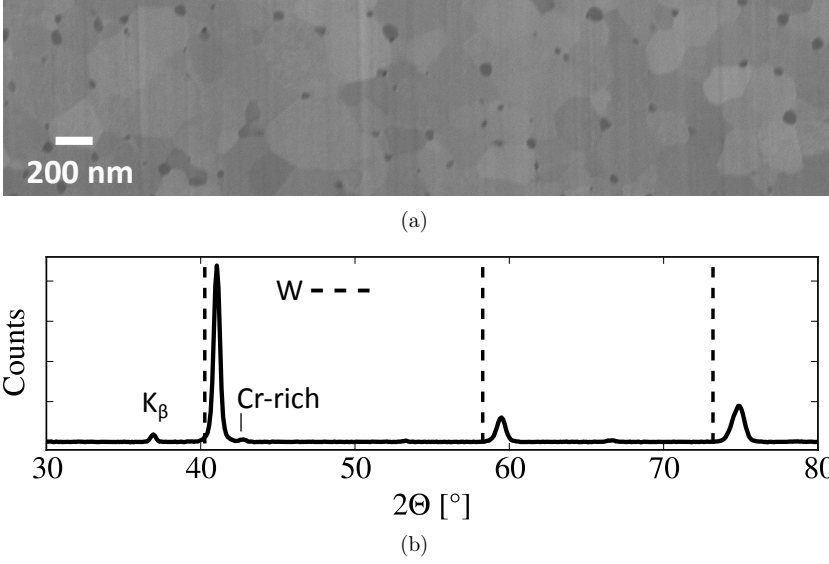
Figure 11.6: Results on the characterization of the sintered W-11.2-1.7Zr alloy. (**a**) the microstructure in a cross section. (**b**) the XRD diffractogram. The peak positions expected for pure W are marked [81].

μ of the three main peaks is shifted on average by 0.04° towards the peak position of pure W as compared to the μ of the W-Cr-Y alloys. This shift corresponds to a change from (6.7±0.016) wt. % for W-Cr-Y to (6.5±0.013) wt. % for W-Cr-Zr. The calculation follows the equations given in section 6.2, the error bar is based on the error on the mean of the three peaks, the systematic error of a few % is not included (see chapter 6 for a more detailed discussion). The peak widths remain constant. Thus, the peaks of the main phase do not indicate significant differences between the W-Cr-Y and W-Cr-Zr alloy.

The position of the peak of the Cr-rich phase, as given in table 11.2, suggests a Cr-rich phase containing 29 wt. % Cr. The shift of the peak position as compared to the W-Cr-Y alloy is 0.5°. The shift is smaller as compared to the shift of the peak during the sintering process, as analyzed in section 6.2. Further, the amplitude of the peak from the Cr-rich phase is 70 times lower than the peak from the main phase, see Fig. 11.6 b. Therefore, it is concluded that the alloy is suitable for comparing the oxidation resistance of W-Cr-Zr and W-Cr-Y.

Table 11.2: Results of Gaussian fits to the XRD peaks from the W lattice planes (110), (200), (211), and the Cr-rich phase shown in Fig. 11.6 b. μ is the mean and σ is the standard deviation of the Gaussian fit. The results of W-Cr-Y given in table 6.1 are repeated for comparison.

sample		(110)	(200)	(211)	Cr-rich
W-Cr-Zr	μ [°]	41.04	59.47	74.84	42.72
	σ [°]	0.2	0.3	0.4	0.2
W-Cr-Y from table 6.1	μ [°]	41.06	59.51	74.89	42.19
	σ [°]	0.2	0.3	0.4	0.3

11.2.2 Oxidation behavior in dry atmosphere

The sintered W-11.2Cr-1.7Zr alloy is oxidized at 1273 K in synthetic air at atmospheric pressure. The mass change due to oxidation as a function of time is plotted in Fig. 11.7. The mass gain is 16 times higher than the mass gain of the W-11.4Cr-0.6Y alloy. Thus, the promising oxidation resistance observed on thin films is not achieved using bulk alloys.

The XRD of the sample after oxidation for 44 h is shown in Fig. 11.8: the diffractogram matches the fingerprint characteristics for Cr_2WO_6 [95]. No other relevant peaks, in particular no Cr_2O_3 peaks are detected. The absence of the protective Cr_2O_3 is the reason for the degraded oxidation resistance.

These findings allow multiple conclusions:

- The grain size of the W-Cr-Zr is larger compared to the W-Cr-Y alloys with the smallest grains but smaller compared to the W-Cr-Y alloys with the largest grains, see section 7.1. All W-Cr-Y alloys in section 7.1 show a higher oxidation resistance than W-Cr-Zr shown in Fig. 11.7. Thus, the grain size is not expected to be the crucial aspect for the degraded oxidation resistance.

- The magnetron films have a finer dispersion of Zr as compared to the bulk alloys. Zr might be efficient only in such a fine dispersion. Optimization of the sintering process should target to reach a finer Zr distribution with smaller zirconia particles. Sintering of the W-Cr-Zr alloy was performed on the optimum parameters for W-Cr-Y. However, it is not clear that these parameters are also the optimum for W-Cr-Zr.

- Zr is a very efficient active element once there is a protective Cr_2O_3 layer, see section 11.1.3. However, this requires the initial formation of such a Cr_2O_3 scale. This finding suggests that Y in comparison to Zr is more efficient in initiating the formation of the protective oxide layer - see the results on nucleation sites in section 9.2. Zr on the other hand is more efficient in stabilizing and maintaining the protective Cr_2O_3 scale - see the results in section 11.1.2 where the oxide layer remains stable despite full depletion of the alloying elements.

These conclusions and hypotheses strongly suggest to investigate quaternary W-Cr-Zr-Y alloys in future research. The aforementioned benefits of Y and Zr could be combined to an alloy with further improved oxidation resistance. The elemental composition of such an alloy should be optimized. The author suggests to orientate on the composition of the optimized, ternary alloys and use W-11Cr-1Zr-0.5Y as a starting point.
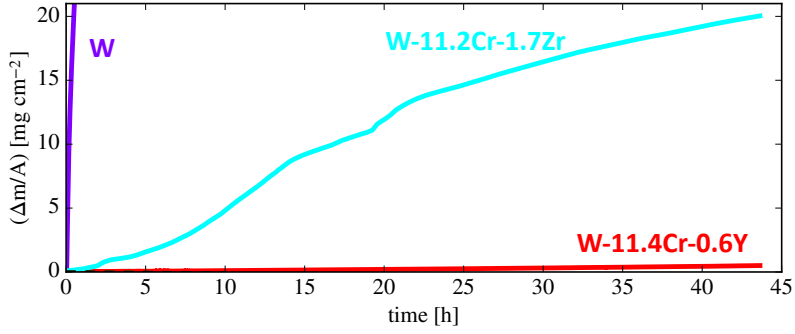
Figure 11.7: Mass gain due to oxidation as a function of time. The performance of W, W-11.2Cr-1.7Zr, and W-11.4Cr-0.6Y is compared. Oxidation is performed at 1273 K in synthetic air at atmospheric pressure.
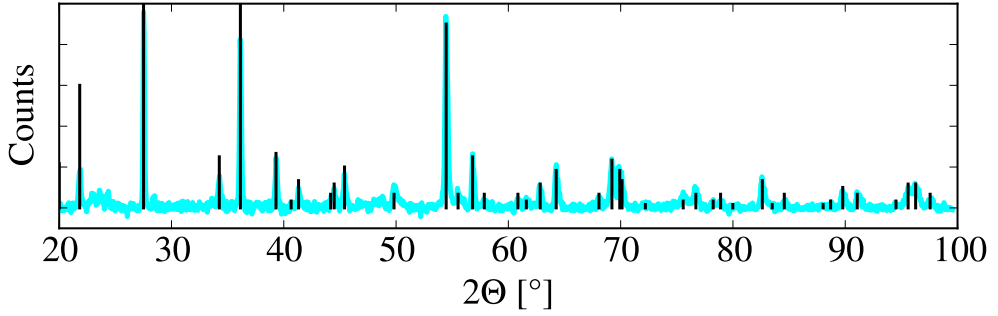
Figure 11.8: The result of an XRD measurement of the W-11.2Cr-1.7Zr bulk alloy oxidized for 44 h at 1273 K in synthetic air at atmospheric pressure. The vertical, black lines mark the peak positions and intensities expected for Cr_2WO_6 [95].

Chapter 12

Conclusions and outlook

12.1 Conclusions

Fusion power on earth is a fundamentally new source of electricity. Technological realization poses multiple challenges to research, an understanding of the underlying physics is crucial. This work investigates new oxidation resistant W alloys as plasma-facing armor material of future fusion power plants.

Oxidation resistance is important for intrinsic safety of the power plant in case of a loss of cooling accident and simultaneous air ingress into the vacuum vessel (LOCA). W oxidizes and sublimates in case of a LOCA causing the release of radioactive material to the environment. Therefore, pure W cannot be used as first wall armor material in future fusion power plants (see section 3.2).

This thesis presents investigations on a material having W-like properties during operation of the power plant and passively forming a protective oxide layer in case of a LOCA which stops the sublimation of radioactive material. It is called 'smart alloy' as it automatically adapts to the environment. Smart alloys contain W as base material, Cr as main alloying element to form a protective oxide layer when required, and Y in small amounts to support the protective Cr_2O_3 formation and stability.

Measurements on thin films deposited by magnetron sputtering prove the feasibility of the concept (see [53, 30] and chapter 5). Dedicated studies on the oxidation mechanisms (see chapter 9) show that Cr diffuses to the surface of the oxide layer to continuously replenish the protective oxide. The oxidation resistance appears invariant to phase formation of a Cr-rich phase on a nano-scale - the Cr still participates in replenishing the protective oxide layer.

Thin films have a limited material reservoir and thus are not suitable for oxidation experiments lasting days or longer. Bulk samples are prepared by mechanical alloying of elemental powders followed by compacting of the alloyed powder using field assisted sintering technology (FAST). The technology is already applied in industry for various materials [56] and has the potential to be upscaled for production of the armor material of a future fusion power plant. The size of the bulk samples investigated in this thesis is relevant for application in future fusion power plants where the thickness of the first wall armor is envisaged to be around 3 mm [128]. The mechanisms of the sintering process for W-Cr-Y are discussed in section 6: the lower the thermal energy and the shorter the exposure time to elevated temperatures the smaller is the grain size of the resulting alloy. The process of compacting and grain structure formation occurs within minutes.

The mechanisms of the sintering process are considered when studying the influences

of the sintering parameters on the oxidation resistance in chapter 7. The mobility of Cr within the metal increases with a decreasing grain size and allows effective replenishing of the protective oxide layer. Therefore, the grain size is minimized to around $0.2\,\mu m$ by using a heating rate of $200\,K\,min^{-1}$ to a maximum sintering temperature of $1740\,K$ without holding time at $1740\,K$. Full compacting is not achieved at lower sintering temperatures due to a lack of ductility of the powder particles.

The influence of the surface roughness on oxidation (see section 7.2) is studied using an alloy compacted with the optimized sintering parameters. A smooth surface appears to be required to provide a good oxidation resistance. Sharp edges and scratches initiate the failure of the protective oxide layer. Thus, a careful surface preparation is required before introducing smart alloys into the reactor - the plasma operation is not expected to create new scratches on the material.

Further, the required elemental composition and the role of Y is investigated. Experimental results yield various hypotheses on the effect of Y:

- More than $1\,wt.\,\%$ of Y destabilizes the protective oxide layer and causes breakaway oxidation. The optimum Y content is $0.6\,wt.\,\%$ (see section 7.3).

- Y binds O in the alloy in the form of $YCrO_3$ nano-particles. O impurities in the alloy are a cause for degradation of the oxidation resistance (see sections 8.3 and 9.2.2).

- A continuous layer of Y is detected at the grain boundaries of the oxide where it reduces the diffusion of O and Cr ions slowing down the oxidation rate (see section 9.2.2).

- Y can promote the selective oxidation of Cr during the initial formation of the protective oxide layer by providing nucleation sites (see section 9.2). So far these nucleation sites are only detected on thin films.

- Y appears to stabilize the W-Cr phase. This can appear via effects of grain boundary pinning by nano-particles [121], but also via the change in configurational entropy of the system which increases the solubility of Cr in W (see the calculations in section 10.2).

The excellent oxidation resistance of the W-11.4Cr-0.6Y alloys is the result of a combination from these effects.

The interaction of the new material with dry and humid air is studied for an experiment duration of up to three weeks. A new method of measuring the sublimation rate is developed and calibrated during this Ph.D. work (see section 2.16). Knowledge about the sublimation allows estimates of the radiological hazard and quantification of the improvement brought by smart alloys as compared to pure W:

- In dry air at $1273\,K$ the sublimation rate is reduced by a factor of 3 (see section 8.1).

- In humid air the sublimation rate is reduced by more than one order of magnitude (see section 8.2).

In the presence of humidity the total sublimation from smart alloys is dominated by the sublimation of Cr_2O_3. Water reacts with Cr_2O_3 and increases the sublimation rate of

Cr_2O_3 as compared to dry air but also promotes the selective oxidation of Cr suppressing the formation of W oxides.

The protection mechanism works up to 1273 K. At temperatures as high as 1473 K smart alloys cannot stop the release of radioactive material (see section 8.3). Current developments cannot offer a solution to this problem. Al_2O_3 is known to be stable to temperatures beyond 1300 K [129] - however, it is not suitable in a fusion reactor environment as it forms very long-lived radioactive isotopes under neutron irradiation [19]. An elemental screening study showed that Cr is required for the oxidation resistance, possible substitutes for Cr were not found [29]. Therefore, the design concept of a future fusion power plant should be adapted in a way that the first-wall temperature peaks around 1250 K in case of an accident.

The potential of mutual benefit of materials development from different fields is demonstrated (see chapter 10). The methods employed on oxidation resistant W alloys are used to manufacture and characterize high-entropy alloys. Computational methods typically employed for the development of high-entropy alloys are employed on smart alloys. The computational models have predicted first experimental results and are used to improve the understanding of smart alloys.

Zr is investigated as an alternative active element to Y (see chapter 11). It shows a promising oxidation resistance on thin films and the protective function of a Cr-Zr-O layer is significantly improved as compared to a pure Cr-O layer. However, direct transfer of the knowledge on the sintering and production of W-Cr-Y alloys onto the production of bulk W-Cr-Zr alloys yields a significantly worse oxidation resistance of W-Cr-Zr as compared to W-Cr-Y. The main hypothesis is that the promotion of formation of the initial protective oxide scale is not efficient for W-Cr-Zr, further research is required.

12.2 Next steps towards smart alloys in a fusion power plant

The results shown in this thesis show that W-11.4Cr-0.6Y alloys are a strong candidate as first wall armor material for future fusion power plants. A mitigation of the radioactive hazard in case of a LOCA is demonstrated up to 1273 K on bulk, laboratory samples. An advanced understanding of the new alloy is demonstrated. This successful work opens a full new field of research. The most critical topics are addressed in the following.

12.2.1 Analytic understanding

Various experiments were performed yielding a general understanding of smart alloys. Still, a mathematical description is lacking. First steps to improve that situation are presented in chapter 10 where computational methods are employed. So far the kinetics are not considered and multiple simplifications are made. For example oxygen and grain boundaries are not considered. Such an understanding may yield to new concepts improving the material further and to solutions for some of the issues presented in the following.

12.2.2 Application in a fusion environment

The application in a fusion environment requires the understanding and investigation of the interplay of different parameters influencing the alloy such as:

- Plasma-alloy interaction. First studies on this topic are published in [21, 99].

- Exposure to elevated temperatures. Exposure to 923 K for 1000 h did not yield a change in the microstructure [130]. On the other hand an enrichment of a few monolayers of Cr on the surface is detected by low energy ion-scattering starting from a temperature of 700 K [131]. The consequences and mechanisms should be investigated in more detail.

- Neutron irradiation: defects and new impurity elements due to transmutations. So far little work in this direction is done. A first step is to calculate the expected composition after neutron irradiation and to prepare samples accordingly. For example a pure W sample would contain around 1 at. % Re, 0.33 at. % Ta, and 0.1 at. % Os after 2 years of DEMO-like irradiation [19]. The effect of such alloying elements should be studied in a non-activated environment.

The applicability of smart alloys in the divertor is another field of research. In ITER the surface area of the divertor will be 120 m^2 while the first wall will have a surface area of ~ 700 m^2, thus the divertor constitutes 15 % of the total surface area [132]. As an approximation one can assume the same ratio in DEMO. Smart alloys on the first wall would suppress the sublimation in case of a LOCA by a factor of e.g. 47 as compared to pure W (see section 8.2). These assumptions yield that 89 % of the sublimated material would originate from the divertor at 1273 K in humid air. Thus, the W divertor would become the main source of volatile, radioactive material. The surface temperature of the divertor during operation of DEMO is foreseen to be above 2000 K [133]. Such a temperature is expected to decompose smart alloys due to phase formation, Cr diffusion

to the surface, and Cr erosion from the surface. The author is skeptical that the current concept of smart alloys can be applied successfully in the divertor.

Finally, the transport and deposition of mobilized material in case of a LOCA should be studied. Such studies may yield to the development of additional safety measures to trap mobilized, radioactive material. Also, acceptable radiological boundaries for the potential release of material should be specified.

12.2.3 Merging different advanced materials concepts

Besides understanding and development of the alloy itself one should face the challenges which may arise when merging advanced concepts for plasma-facing materials in fusion and smart alloys. Most concepts are developed for W and a transition of technology to W-Cr-Y seems feasible but requires demonstration and testing.

One issue is joining the first wall armor to the structural material while avoiding plastic strains potentially causing delamination. Currently two main approaches are tested: a graded layer near the interface [134] and ductile foils at the interface [135]. The ideal solution is not yet found and one should investigate these possibilities by joining W-Cr-Y instead of W to a structural steel. The aim should be to manufacture a flat-tile prototype for testing.

Another issue is the intrinsic brittleness of W. Alloying is not expected to improve the mechanical properties. Therefore, the concepts of tungsten fiber reinforced tungsten (W_f/W) [136] and alloying should be merged. W_f/W provides pseudo ductility to the material by increasing the resistance to crack propagation. Thus, the risk of catastrophic failure is reduced.

In a first step a tungsten fiber reinforced W-Cr-Y alloy ($W_f/WCrY$) is compacted by FAST. A photograph of the sample is shown in Fig. 12.1 a, W fibers touching the surface are visible. The sample is oxidized for 15 min at 1273 K in 20 kPa O_2 and 80 kPa Ar atmosphere. Yellow spots of WO_3 are visible on the surface, as seen in Fig. 12.1 b. The W fibers do not contain any Cr which could form a protective oxide layer. Thus, W fibers touching the surface oxidize rapidly and dominate the oxidation and sublimation characteristics. The surface layer is gradually eroded during plasma operation, thus it is not feasible to have a fiber-free coating. The approach which should be tested is to draw the fibers from the alloy material.
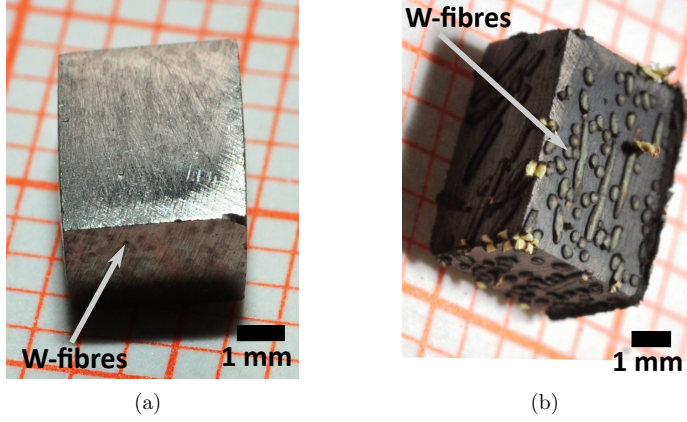
Figure 12.1: (**a**) A photograph of a sintered tungsten fiber reinforced tungsten sample. (**b**) A photograph of the sample shown in (a) after 15 min of oxidation at 1273 K in 20 kPa O_2 and 80 kPa Ar atmosphere.

12.2.4   Up-scaling and industrialization

A 2 mm thick first wall armor on an area of $1000\,\mathrm{m}^2$ made from the developed W-Cr-Y-alloy weighs more than 30 t. Therefore, up-scaling and industrialization are a crucial step for the material to be actually employed in future fusion power plants. Science should deliver the knowhow on the materials to industry and accompany the technology development for industrial production. This activity should be conducted in parallel to final optimization and understanding of the new material in order address new questions as early as possible.

Industrial manufacturing may follow the FAST route described in this thesis. In that case one should investigate and predict the influence of the stamp diameter and estimate the significance of inhomogeneities. Currently, the powder is prepared by mechanical alloying and requires multiple manual steps. It yields only $\sim 100\,\mathrm{g}$/process. Realistic specifications and tolerances must be found for up-scaling and automation of the powder production.

The specifications should include information on allowed impurities during production. Impurities in a material change properties and the oxidation resistance of the alloy. For example, O impurities are addressed in this work in section 8.3.

Also other manufacturing routes should be considered and tested. Potential candidates are RF plasma spraying and 3D-printing. Plasma spraying allows to directly spray the alloy onto the structural material avoiding multiple intermediate processing steps. 3D printing of a full component is an appealing but challenging approach. The outcome of all approaches should be an industrial monoblock for accidental and thermo-mechanical tests coupled with supportive tokamak studies.

12.3 Aluminum as an alloying element?

Oxidation resistance at high temperatures is also relevant for applications outside the field of nuclear fusion. Examples are the blades of new generation gas turbines, heat exchangers, or the receiver of concentrated solar power plants. Ceramics have the problem of a low thermal or electrical conductivity. Coatings are always subject to a risk of spallation and sudden loss of the protective function. Superalloys are restricted by their melting point at around 1600 K [137]. Currently new concepts such as MAX phases are developed [138]. Oxidation resistant W alloys are another candidate.

The alloy developed in this thesis provides good oxidation resistance up to 1273 K. Aluminium (Al) as alloying element is the most logical choice to increase the application temperature. Al forms radioactive isotopes with a half-life of 7.2×10^5 years under neutron irradiation [19], that is an exclusion criterion only in a fusion environment. Analogous methods as used in this thesis could be employed to investigate W-Al-xx alloys, where xx are further alloying elements.

First promising tests on binary W-4Al alloys are conducted. A film is deposited by magnetron sputtering (as explained in section 2.1) by applying a DC power of 500 W to the W target and 756 W to the Al target. The resulting composition of W with 4 wt. % Al is measured using EDX. A cross section of the deposited alloy is shown in Fig. 12.2 a.

The cross section of the W-4Al alloy after an oxidation test at 1273 K in 20 kPa O_2 and 80 kPa Ar atmosphere for 10 min is shown in Fig. 12.2 b. A 0.2 µm thick alumina layer forms on the surface of the alloy suppressing the formation of tungsten oxides. Phase separation and pore formation is observed in the entire film with a thickness of ~ 3.2 µm.

The surface image of the W-4Al alloy after an oxidation test at 1273 K in 20 kPa O_2 and 80 kPa Ar atmosphere for 80 min is shown in Fig. 12.2 c. Spallation and failure of the protective oxide scale is observed. Failure of the protective oxide layer occurs after shorter times as compared to the W-Cr-Y films investigated in chapter 5.

Further research is required in order to achieve a good oxidation resistance of W-Al-xx alloys. Different elemental compositions should be tested. Complementary computational analysis, similar as presented in section 10.2, is helpful.
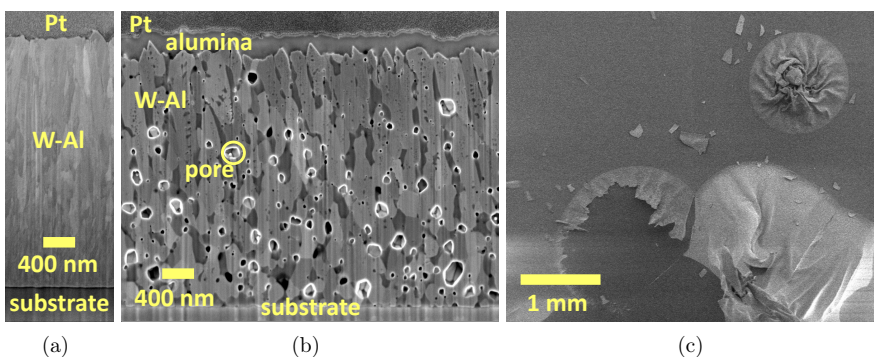
Figure 12.2: W-4Al alloy (**a**) as deposited and after oxidation at 1273 K in 20 kPa O_2 and 80 kPa Ar atmosphere for (**b**) 10 min and (**c**) 80 min.

Chapter 13

Bibliography

[1] OECD/IEA, F. Birol. Key world energy statistics. *IEA Publishing*, 2017.

[2] D. Connolly, H. Lund, B. V. Mathiesen, E. Pican, and M. Leahy. The technical and economic implications of integrating fluctuating renewable energy using energy storage. *Renew. Energ.*, 43:47–60, 2012.

[3] Foratom. What people really think about nuclear energy. *atw*, 62(3):157, 2017.

[4] Nicolas Cooper, Daisuke Minakata, Miroslav Begovic, and John Crittenden. Should we consider using liquid fluoride thorium reactors for power generation? *Environ. Sci. Technol.*, 45:6237–6238, 2012.

[5] OECD and Nuclear Energy Agency, editors. *Nuclear Energy Today (Second Edition)*. 2013.

[6] K. Miyamoto. *Plasma physics for nuclear fusion*. Cambridge, Mass., MIT Press, 1980.

[7] J.R. Jr. McNally, K.E. Rothe, and R.D. Sharp. Fusion reactivity graphs and tables for charged particle reactions. Technical report, Oak Ridge National Lab., TN (USA), 1979.

[8] H.-S. Bosch. Review of data and formulas for fusion cross-sections. Max-Planck-Institut für Plasmaphysik, IPP I/252, 1990.

[9] J. Wesson. *Tokamaks, Fourth Edition*. Oxford University Press, 2011.

[10] F. Maviglia, R. Albanese, R. Ambrosino, W. Arter, C. Bachmann, T. Barrett, G. Federici, M. Firdaous, J. Gerardin, M. Kovari, et al. Wall protection strategies for DEMO plasma transients. *Fusion Eng. Des.*, 136(A):410–414, 2018.

[11] Ch. Linsmeier, M. Rieth, J. Aktaa, T. Chikada, A. Hoffmann, J. Hoffmann, A. Houben, H. Kurishita, X. Jin, M. Li, et al. Development of advanced high heat flux and plasma-facing materials. *Nucl. Fusion*, 57(9):092007, 2017.

[12] E. Lassner and W. D. Schubert. *The Element Tungsten. In: Tungsten*. Springer, Boston, MA, 1999.

[13] G. Wouch, E. L. Gray, R. T. Frost, and A. E. Lord. Estimation of thermodynamic properties from solidification and cooling curves of containerless melts in the terrestrial environment and in space. *High Temp. Sci.*, 10(4):241–259., 1978.

[14] T. Tanabe. Review of hydrogen retention in tungsten. *Phys. Scr.*, 2014(T159):014044, 2014.

[15] M. R. Gilbert, T. Eade, C. Bachmann, U. Fischer, and N. P. Taylor. Activation, decay heat, and waste classification studies of the European DEMO concept. *Nucl. Fusion*, 57(4):046015, 2017.

[16] T. Tanno, A. Hasegawa, J. C. He, M. Fujiwara, S. Nogami, M. Satou, T. Shishido, and K. Abe. Effects of transmutation elements on neutron irradiation hardening of tungsten. *Mater. Trans.*, 48(9):2399–2402, 2007.

[17] D. Maisonnier, I. Cook, P. Sardain, L. Boccaccini, E. Bogusch, K. Broden, L. Di Pace, R. Forrest, L. Giancarli, S. Hermsmeyer, et al. The european power plant conceptual study. *Fusion Eng. Des.*, 75:1173–1179, 2005.

[18] J. E. Battles, G. R. St. Pierre, and R. Speiser. Research on the oxidation behavior of tungsten: Part III. volatility of the oxides of tungsten. *Report under Contract No. AF33(616)-5721 between the Ohio State University Research Foundartion and the U.S. Air Force*, 1962.

[19] Mark R. Gilbert, J.-C. Sublet, and R. A. Forrest. *Handbook of activation, transmutation, and radiation damage properties of the elements simulated using FISPACT-II & TENDL*. Culham Center For Fusion Energy, 2015.

[20] G. Steinhauser, A. Brandl, and T. E. Johnson. Comparison of the Chernobyl and Fukushima nuclear accidents: A review of the environmental impacts. *Science of The Total Environment*, 470 - 471:800 – 817, 2014.

[21] J. Schmitz, A. Litnovsky, F. Klein, T. Wegener, X. Y. Tan, M. Rasinski, A. Mutzke, P. Hansen, A. Kreter, A. Pospieszczyk, et al. WCrY smart alloys as advanced plasma-facing materials - exposure to steady-state pure deuterium plasmas in PSI-2. *Nucl. Mater. Energy*, 15:220–225, 2018.

[22] F. Koch and H. Bolt. Self passivating W-based alloys as plasma facing material for nuclear fusion. *Phys. Scr.*, T128:100–105, 2007.

[23] J. S. Dunn. The oxidation of tungsten. *J. Chem. Soc.*, 0:1149–1150, 1929.

[24] O. Kubaschewski and A. Schneider. Measurements on the oxidation-resistance of high-melting-point alloys. *J. Inst. Met.*, 75:403–416, 1949.

[25] A. Kelly and W. R. Tyson. Tensile properties of fibre-reinforced metals: Copper/tungsten and copper/molybdenum. *J. Mech. Phys. Solids*, 13:329–350, 1965.

[26] R. C. Wetherhold and L. J. Westfall. Thermal cycling of tungsten-fibre-reinforced superalloy composites. *J. Mater. Sci.*, 23:713–717, 1988.

[27] K. T. Jacob. Phase relationships in the system Cr-W-O and thermodynamic properties of $CrWO_4$ and Cr_2WO_6. *J. Mater. Sci.*, 15(9):2167–2174, 1980.

[28] S. V. Nagender Naidu, A. M. Sriramamurthy, and P. Rama Rao. The Cr-W (chromium-tungsten) system. *Bulletin of Alloy Phase Diagrams*, 5(3):289–292, 1984.

[29] F. Koch, J. Brinkmann, S. Lindig, T. P. Mishra, and Ch. Linsmeier. Oxidation behaviour of silicon-free tungsten alloys for use as the first wall material. *Phys. Scr.*, 2011(T145):014019, 2011.

[30] T. Wegener, F. Klein, A. Litnovsky, M. Rasinski, J. Brinkmann, F. Koch, and Ch. Linsmeier. Development of yttrium-containing self-passivating tungsten alloys for future fusion power plants. *Nucl. Mater. Energy*, 9:394–398, 2016.

[31] H.T. Greenaway. The constitutional diagram of the chromium-tungsten system. *J. Inst. Met.*, 80:589–592, 1952.

[32] E. Rudy. Compendium of phase diagram data. *Tech. Rpt. AFML-TR-65-2, Part V, Wright-Patterson Air Force Base, OH*, pages 151–153, 1969.

[33] W. Trzebiatowski, H. Ploszek, and J. Lobzowski. X-ray analysis of chromium-molybdenum and chromium-tungsten alloys. *Anal. Chem.*, 19:93–95, 1947.

[34] F. J. A. Den Broeder. Interface reaction and a special form of grain boundary diffusion in the Cr-W system. *Acta Metallurgica*, 20(3):319–332, 1972.

[35] T. Margaria, C. Allibert, I. Ansara, and J. Driole. High-temperature study of the tungsten-nickel-chromium system. *High Temp.-High Pressures*, 8:451–459, 1976.

[36] L. El-Guebaly, P. Wilson, M. Sawan, D. Henderson, and A. Varuttamaseni. Recycling issues facing target and RTL materials of inertial fusion designs. *Nucl. Instr. Meth. Phys. Res. A*, 544(1-2):104–110, 2005.

[37] A. Calvo, C. Garcia-Rosales, F. Koch, N. Ordas, I. Iturriza, H. Greuner, G. Pintsuk, and C. Sarbud. Manufacturing and testing of self-passivating tungsten alloys of different composition. *Nucl. Mater. Energy*, 9:422–429, 12 2016.

[38] W. T. Griffiths and L. B. Pfeil. Patent U.K. 459848, 1937.

[39] E. Lang, editor. *The Role of Active Elements in the Oxidation Behaviour of High Temperature Metals and Alloys.* Elsevier Applied Science, 1989.

[40] R. Buergel, H. J. Maier, and T. Niendorf. *Handbuch Hochtemperatur-Werkstofftechnik.* PRAXIS, 2011.

[41] Thomas B. Reed, editor. *Free Energy of Formation of Binary Compounds.* MIT Press, Cambridge, 1971.

[42] M. K. Miller, E. A. Kenik, K. F. Russell, L. Heatherly, D. T. Hoelzer, and P. J. Maziasz. Atom probe tomography of nanoscale particles in ods ferritic alloys. *Mater. Sci. Eng. A*, 353(1-2):140–145, 2003.

[43] P. R. Aimone and R. L. McCormick. The effects of yttrium and sulfur on the oxidation resistance of an advanced single crystal nickel based superalloy. *Superalloys*, 26(8):817–823, 1992.

[44] N. Birks, G. H. Meier, and F. S. Pettit. *Introduction to the High-Temperature Oxidation of Metals*. Cambridge University Press, 2006.

[45] K. Przybylski, A. J. Garratt-Reed, and G. J. Yurek. Grain boundary segregation of yttrium in chromia scales. *J. Electrochem. Soc.*, 135(2):509–517, 1988.

[46] R. Mevrel. Cyclic oxidation of high-temperature alloys. *J. Mater. Sci. Technol.*, 3(7):531–535, 1987.

[47] J. Stringer, B. A. Wilcox, and R. I. Jaffee. The high-temperature oxidation of nickel-20 wt. % chromium alloys containing dispersed oxide phases. *Oxid. Met.*, 5(1):11–47, 1972.

[48] W. J. Quadakkers, H. Holzbrecher, K. G. Briefs, and H. Beske. The effect of yttria dispersions on the growth mechanisms and morphology of chromia and alumina scales. In E. Lang, editor, *The Role of Active Elements in the Oxidation Behaviour of High Temperature Metals and Alloys*, pages 155–173. Springer Netherlands, 1989.

[49] D. J. Young. *High temperature oxidation and corrosion of metals*. Elsevier, 2008.

[50] C. V. Robino. Representation of mixed reactive gases on free energy (Ellingham-Richardson) diagrams. *Metall. Mater. Trans. B*, 27(1):65–69, 1996.

[51] T. B. Reed. *Free energy of formation of binary compounds: an atlas of charts for high-temperature chemical calculations*. MIT Press in Cambridge, Mass., 1971.

[52] J. Schilz, M. Riffel, K. Pixius, and H.-J. Meyer. Synthesis of thermoelectric materials by mechanical alloying in planetary ball mills. *Powder Technol.*, 105(1-3):149–154, 1999.

[53] T. Wegener. *Tungsten-Chromium-Yttrium as Self-Passivating Tungsten Alloy*. PhD thesis, Rheinisch-Westfälische Technische Hochschule Aachen, presumably 2019.

[54] C. Kittel. *Introduction to Solid State Physics*. John Wiley & Sons, 2005.

[55] A. Calvo, N. Ordas, I. Iturriza, J. Y. Pastor, E. Tejado, T. Palacios, and C. Garcia-Rosales. Manufacturing of self-passivating tungsten based alloys by different powder metallurgical routes. *Phys. Scr.*, 2016(T167), 2016.

[56] O. Guillon, J. Gonzalez-Julian, B. Dargatz, T. Kessel, G. Schierning, J. Räthel, and M. Herrmann. Field-assisted sintering technology/spark plasma sintering: Mechanisms, materials, and technology developments. *Adv. Eng. Mater.*, 16(7):830–849, 2014.

[57] E. A. Olevsky and D. V. Dudina. *Field-Assisted Sintering*. Springer, Cham, 2018.

[58] L. Spiess, R. Schwarzer, H. Behnken, and G. Teichert. *Moderne Röntgenbeugung: Röntgendiffraktometrie für Materialwissenschaftler, Physiker und Chemiker*. Springer-Verlag, 2015.

[59] S. Fearn. *An Introduction to Time-of-Flight Secondary Ion Mass Spectrometry (ToF-SIMS) and its Application to Materials Science*. Morgan & Claypool Publishers, 20105.

[60] N. P. Lockyer and J. C. Vickerman. *Encyclopedia of Materials: Science and Technology*, chapter SIMS, Time-of-flight, and Surface Analysis, pages 8624–8628. Elsevier Ltd., 2001.

[61] T. E. Everhart and R. F. M. Thornle. Wide-band detector for micro-microampere low-energy electron currents. *J. Sci. Instrum.*, 37(7):246, 1960.

[62] B. J. Griffin. A comparison of conventional everhart-thornley style and in-lens secondary electron detectors - a further variable in scanning electron microscopy. *Scanning*, 33(3):162–173, 2011.

[63] P. J. Potts. *A Handbook of Silicate Rock Analysis (Electron probe microanalysis)*. Springer Netherlands, 1987.

[64] Ernst Ruska-Centre for Microscopy and Spectroscopy with Electrons. FEI Titan 80-300 STEM. *JLSRF*, 2(A42), 2016.

[65] B. Gault. A brief overview of atom probe tomography research. *Applied Microscopy*, 46(3):117–126, 2016.

[66] A. W. Coats and J. P. Redfern. Thermogravimetric analysis. a review. *Analyst*, 88:906–924, 1963.

[67] W. T. Ebihara, W. P. Meuli, R. Speiser, J. W. Spretnak, and G. R. St. Pierre. Research on the oxidation behavior of tungsten: Part II. the kinetics of oxidation of tungsten. *Report under Contract No. AF33(616)-5721 between the Ohio State University Research Foundartion and the U.S. Air Force*, 1962.

[68] E. Lassner and W. D. Schubert. *Tungsten: Properties, Chemistry, Technology of the Element, Alloys, and Chemical Compounds*. Springer Science+Business Media, LLC, 1999.

[69] G. R. St. Pierre, W. T. Ebihara, M. J. Pool, and R. Speiser. Research on the oxidation behavior of tungsten: Part I. the thermodynamics of the tungsten-oxygen system. *Report under Contract No. AF33(616)-5721 between the Ohio State University Research Foundartion and the U.S. Air Force*, 1962.

[70] E. A. Gulbransen and W.S. Wysong. Thin oxide films on tungsten. *Trans. AIME*, 175:611–627, 1948.

[71] W. W. Webb, J. T. Norton, and C. Wagner. Oxidation studies in metal-carbon systems. *J. Electrochem. Soc.*, 103(2):112–117, 1956.

[72] G. A. Greene and C. C. Finfrock. Vaporization of tungsten in flowing steam at high temperatures. *Exp Therm Fluid Sci*, 25(3-4):87–99, 2001.

[73] P. E. Blackburn, K. F. Andrew, E. A. Gulbransen, and F. A. Brassart. Oxidation of tungsten and tungsten based alloys. WADC technical report 59-575, Armed Services Technical information agency, Arlington Hall Station, Arlington 12, Virgina, USA, 1961.

[74] G. R. Belton and R. L. McCarron. The volatilization of tungsten in the presence of water vapor. *J. Phys. Chem.*, 68(7):1852–1856, 1964.

[75] W. J. Quadakkers and J. Zurek In: J. A. Richardson et al (eds). *Shreir's Corrosion*, volume 1, chapter Oxidation in Steam and Steam/Hydrogen Environments, pages 407–456. Elsevier, 2010.

[76] Y.-W. Kim and G. R. Belton. The thermodynamics of volatilization of chromic oxide: Part I. the species CrO_3 and $CrO_2 OH$. *Metall Trans.*, 5:1974–1811, 1974.

[77] D. Caplan and M. Cohen. The volatilization of chromium oxide. *J. Electrochem. Soc.*, 108(5):438–442, 1961.

[78] F. Klein, T. Wegener, A. Litnovsky, M. Rasinski, X. Y. Tan, J. Schmitz, Ch. Linsmeier, J. W. Coenen, H. Du, J. Mayer, and U. Breuer. On oxidation resistance mechanisms at 1273 K of tungsten-based alloys containing chromium and yttria. *Metals*, 8(7):488, 2018.

[79] E.T. Turkdogan. *Physical Chemistry of High Temperature Technology*. Academic Press, 1980.

[80] J. A. Thornton. Influence of substrate temperature and deposition rate on structure of thick sputtered Cu coatings. *J. Vac. Sci. Technol.*, 12(4):830, 1975.

[81] H. E. Swanson. *Standard X-ray Diffraction Powder Patterns*, volume 1, p. 28. Natl. Bur. Stand. (U. S.), 1953.

[82] R. G. Ross and W. Hume-Rothery. High temperature x-ray metallography: I. a new Debye-Scherrer camera for use at very high temperatures II. a new parafocusing camera III. applications to the study of chromium, hafnium, molybdenum, rhodium, ruthenium and tungsten. *J. Less-Common Met.*, 5(3):258–270, 1963.

[83] T. Wegener, F. Klein, A. Litnovsky, M. Rasinski, J. Brinkmann, F. Koch, and Ch. Linsmeier. Development and analyses of self-passivating tungsten alloys for DEMO accidental conditions. *Fusion Eng. Des.*, 124:183–186, 2017.

[84] R. D. Shannon. Revised effective ionic radii and systematic studies of interatomic distances in halides and chalcogenides. *Acta Crystallogr., Sect. A*, 32(5):751–767, 1976.

[85] A. Calvo, K. Schlueter, E. Tejado, G. Pintsuk, N. Ordas, I. Iturriza, R. Neu, J. Y. Pastor, and C. Garcia-Rosales. Self-passivating tungsten alloys of the system W-Cr-Y for high temperature applications. *Int. J. Refract. Met. Hard Mater.*, 73:29–37, 2018.

[86] J. R. Stephens. Effect of interstitial impurities on the low-temperature tensile properties of tungsten. *NASA Technical Note*, 1964.

[87] ASTM Committee E-4 on Metallography, editor. *ASTM E112-13, Standard Test Methods for Determining Average Grain Size*. ASTM International, West Conshohocken, PA, United States, 1996.

[88] B. R. Jennings and K. Parslow. Particle size measurement: the equivalent spherical diameter. *Proc. Roy. Soc. A*, 419(1856):137–149, 1988.

[89] J. R. Davis, editor. *ASM Specialty Handbook: Heat-Resistant Materials.* S. D. Henry, 1999.

[90] S. C. Cifuentes, M. A. Monge, and P. Perez. On the oxidation mechanism of pure tungsten in the temperature range 600 - 800°C. *Corros. Sci.*, 57:114–121, 2012.

[91] F. Klein, T. Wegener, A. Litnovsky, M. Rasinski, X. Y. Tan, J. Gonzalez-Julian, J. Schmitz, M. Bram, J. W. Coenen, and Ch. Linsmeier. Oxidation resistance of bulk plasma-facing tungsten alloys. *Nucl. Mater. Energy*, 15:226–231, 2018.

[92] J. Lee, K. Klockgeter, and Chr. Herzig. Grain boundary self and impurity diffusion in tungsten in the temperature range of activated sintering. *J. Phys. Colloq.*, 51(C1):569–574, 1990.

[93] L. Zhang, Y. Jiang, Q. Fang, R. Liu, Z. Xie, T. Zhang, X. Wang, and C. Liu. Comparative investigation of tungsten fibre nets reinforced tungsten composite fabricated by three different methods. *Metals*, 7(7):249, 2017.

[94] H. F. McMurdie, M. C. Morris, E. H. Evans, B. Paretzkin, W. Wong-Ng, L. Ettlinger, and C. R. Hubbard. Standard x-ray diffraction powder patterns from the JCPDS research associateship. *Powder Diffr.*, 1(2):64–77, 1986.

[95] W. Kunnmann, S. La Placa, L.M. Corliss, J. M. Hastings, and E. Banks. Magnetic structures of the ordered trirutiles Cr_2WO_6, Cr_2TeO_6 and Fe_2TeO_6. *J. Phys. Chem. Solids*, 29(8):1359–1364, 1968.

[96] Yu. A. Barabanenkov, N. D. Zakharov, I. P. Zibrov, V. P. Filonenko, P. Werner, A. I. Popov, and M. D. Valkovskii. High-pressure phases in the system W-O. II. structure determination of $WO_{2.625}$ by HRTEM and x-ray powder diffraction analysis. *Acta Cryst.*, B49(2):165, 1993.

[97] H. J. Borchardt. Yttrium-tungsten oxides. *Inorg Chem*, 2(1):170–173, 1963.

[98] F. Klein, A. Litnovsky, T. Wegener, X. Y. Tan, J. Gonzalez-Julian, M. Rasinski, J. Schmitz, Ch. Linsmeier, M. Bram, and J. W. Coenen. Sublimation of advanced tungsten alloys under DEMO relevant accidental conditions. *Fusion Eng. Des.*, in press, 2019.

[99] J. Schmitz, A. Litnovsky, F. Klein, X. Y. Tan, U. Breuer, M. Rasinski, S. Ertmer, A. Kreter, J. Gonzalez-Julian, M. Bram, et al. Argon-seeded plasma exposure and oxidation performance of tungsten-chromium-yttrium smart alloys. *Tungsten*, 2661-8036:1–10, 2019.

[100] A. Litnovsky, T. Wegener, F. Klein, Ch. Linsmeier, M. Rasinski, A. Kreter, B. Unterberg, J. W. Coenen, H. Du, J. Mayer, et al. Smart tungsten alloys as a material for the first wall of a future fusion power plant. *Nucl. Fusion*, 57(6):066020, 2017.

[101] K. J. R. Rosman and P. D. P. Taylor. Isotopic compositions of the elements 1997. *Pure Appl. Chem.*, 70(1):217–235, 1998.

[102] C. A. Andersen. Progress in analytic methods for the ion microprobe mass analyzer. *Int. J. Mass Spectrom. Ion Phys.*, 2:61, 1969.

[103] S. M. Klotsman, V. M. Koloskov, S. V. Osetrov, I. P. Polikarpova, G. N. Tatarinova, and A. N. Timofeev. Chromium and molybdenum diffusion in tungsten single crystals. *Fiz. Met. Metalloved.*, 67(4):767–774, 1989.

[104] D. S. Gornyy and R. M. Altovskiy. Diffusion of Yt in refractory metals. *Fiz. Met. Metalloved.*, 31:781, 1971.

[105] K. Lazdins and A. Kuzmin. Local structure and lattice dynamics of cubic Y_2O_3: an x-ray absorption spectroscopy study. *IOP Conf. Ser.: Mater. Sci. Eng.*, 77(012031), 2018.

[106] O. C. Hellman, J. A. Vandenbroucke, J. Rüsing, D. Isheim, and D. N. Seidman. Analysis of three-dimensional atom-probe data by the proximity histogram. *Microsc. Microanal.*, 6(5):437–444, 2000.

[107] A. Alkhamees, Y. L. Liu, H. B. Zhou, S. Jin, Y. Zhang, and G. H. Lu. First-principles investigation on dissolution and diffusion of oxygen in tungsten. *J. Nucl. Mater.*, 393(3):508–512, 2009.

[108] Q. Li, H. Zhang, M. Gao, J. Li, T. Tao, and H. Zhang. Mechanisms of reactive element Y on the purification of K4169 superalloy during vacuum induction melting. *Int J Min Met Mater*, 25(6):696, 2018.

[109] Y. Saito, B. Önay, and T. Maruyama. The reactive element effect (REE) in oxidation of alloys. *J. Phys. IV*, 03(C9):217–230, 1993.

[110] J. S. Wróbel, D. Nguyen-Manh, and K. J. Kurzydlowski. Ab initio based modelling of diffusion and phase stability of alloys. *Diffusion Foundations*, 12:1–22, 2017.

[111] A. Fernández-Caballero, J. S. Wróbel, P. M. Mummery, and D. Nguyen-Manh. Short-range order in high entropy alloys: Theoretical formulation and application to Mo-Nb-Ta-V-W system. *J. Phase Equilib. Diffus.*, 38(4):391–403, 2017.

[112] J. A. Yeh, S. K. Chen, S. J. Lin, J. Y. Gan, T. S. Chin, T. T. Shun, C. H. Tsau, and S. Y. Chang. Nanostructured high entropy alloys with multiple principal elements: Novel alloy design concepts and outcomes. *Adv. Eng. Mater.*, 6(5):299–303, 2004.

[113] I. Toda-Caraballo, J. S. Wróbel, D. Nguyen-Manh, P. Pérez, and P. E. J. Rivera-Díaz del Castillo. Simulation and modeling in high entropy alloys. *JOM*, 69(11):2137–2149, 2017.

[114] Y. Zhang, Y. J. Zhou, J. P. Lin, G. L. Chen, and P. K. Liaw. Solid-solution phase formation rules for multi-component alloys. *Adv. Eng. Mater.*, 10(6):534–538, 2008.

[115] B. Cantor, I. T. H. Chang, P. Knight, and A. J. B. Vincent. Microstructural development in equiatomic multicomponent alloys. *Mater. Sci. Eng. A*, 375-377:213–218, 2004.

[116] H. M. Daoud, A. M. Manzoni, R. Völkl, N. Wanderka, and U. Glatzel. Oxidation behavior of $Al_8Co_{17}Cr_{17}Cu_8Fe_{17}Ni_{33}$, $Al_{23}Co_{15}Cr_{23}Cu_8Fe_{15}Ni_{15}$, and $Al_{17}Co_{17}Cr_{17}Cu_{17}Fe_{17}Ni_{17}$ compositionally complex alloys (high-entropy alloys) at elevated temperatures in air. *Adv. Eng. Mater.*, 17(8):1134–1141, 2015.

[117] O. El-Atwani, N. Li, M. Li, A. Devaraj, M. Schneider, D. Sobieraj, J. S. Wróbel, D. Nguyen-Manh, S. A. Maloy, and E. Martinez. Outstanding radiation resistance of tungsten-based high entropy alloys. *Sci. Adv.*, 5(3):eaav2002, 2019.

[118] R. Gross and A. Marx. *Festkörperphysik*. Oldenbourg Verlag München, 2012.

[119] C. R. Hammond. *The Elements*, volume ISBN 978-0-04-910081-7. Fermi National Accelerator Laboratory, 1985.

[120] J. S. Wróbel. Faculty of Materials Science and Engineering, Warsaw University of Technology, ul. Woloska 141, 02-507 Warsaw, Poland.

[121] C. S. Smith. Introduction to grains, phases, and interfaces - an interpretation of microstructure. *Trans. AIME*, 175:15–51, 1948.

[122] K. He and T. N. Baker. Effect of zirconium additions on austenite grain coarsening of C-Mn and microalloy steels. *Mater. Sci. Eng. A*, 256(1):111–119, 1998.

[123] T. N. Baker. The role of zirconium in microalloyed steels. *Mater. Sci. Technol.*, 31(3):265–294, 2015.

[124] A. L. Feild. Some effects of zirconium in steel. *Trans. Am. Inst. Mining Met. Eng.*, 69:848–894, 1923.

[125] C. Lenser. Quaternary self-passivating tungsten alloys. Master thesis, Department of Chemistry at the Technical University of Munich, 2009.

[126] X.Y. Tan, F. Klein, A. Litnovsky, T. Wegener, J. Schmitz, Ch. Linsmeier, J. W. Coenen, U. Breuer, M. Rasinski, P. Li, et al. Evaluation of the high temperature oxidation of W-Cr-Zr self-passivating alloys. *Corros. Sci.*, 147:201–211, 2019.

[127] J. Booth, T. Ekström, E. Iguchi, and R. J. D. Tilley. Notes on phases occurring in the binary tungsten-oxygen system. *J. Solid State Chem.*, 41(3):293–307, 1982.

[128] Yu. Igitkhanov, B. Bazylev, I. Landman, and R. Fetzer. Design strategy for the PFC in DEMO reactor. *KIT Scientific Publishing*, KIT-SR 7637, 2013.

[129] D. Naumenko, B. Gleeson, E. Wessel, L. Singheiser, and W. J. Quadakkers. Correlation between the microstructure, growth mechanism, and growth kinetics of alumina scales on a FeCrAlY alloy. *Metall. Mater. Trans. A*, 38(12):2974–2983, 2007.

[130] C. Garcia-Rosales, E. Sal, I. Iturriza, and I. Andueza. Thermal stability and joining feasibility study of self-passivating tungsten alloys. In *Report on Eurofusion task MAT-3.1.1-T005-D003*, 2018.

[131] R. Koslowski and J. Schmitz. Private communication on ALI measurements using a He beam.

[132] R. A. Pitts, S. Carpentier, F. Escourbiac, T. Hirai, V.Komarov, A. S. Kukushkin, S. Lisgo, A. Loarte, M. Merola, R. Mitteau, et al. Physics basis and design of the ITER plasma-facing components. *J. Nucl. Mater.*, 415(1):957–964, 2011.

[133] Yu. Igitkhanov, B. Bazylev, and R. Fetzer. *The quantification of the key physics parameters for the DEMO fusion power reactor and analysis of the reactor relevant physics issues*. KIT Scientific Publishing, Karlsruhe, page 12, 2014.

[134] S. Heuer, T. Lienig, A. Mohr, Th. Weber, G. Pintsuk, J. W. Coenen, F. Gormann, W. Theisen, and Ch. Linsmeier. Ultra-fast sintered functionally graded Fe/W composites for the first wall of future fusion reactors. *Compos Part B-Eng.*, 164(1):2025–214, 2019.

[135] B. A. Kalin, V. T. Fedotov, O. N. Sevrjukov, A. N. Kalashnikov, A. N. Suchkov, A. Moeslang, and M. Rohde. Development of brazing foils to join monocrystalline tungsten alloys with ODS-EUROFER steel. *J. Nucl. Mater.*, 367-370(B):1218–1222, 2007.

[136] Y. Mao, J. W. Coenen, J. Riesch, S. Sistla, J. Almanstötter, B. Jasper, A. Terra, T. Höschen, H. Gietl, M. Bram, et al. Development and characterization of powder metallurgically produced discontinuous tungsten fiber reinforced tungsten composites. *Phys. Scr.*, 2017(T170):014005, 2017.

[137] P. Caron and T. Khan. Evolution of Ni-based superalloys for single crystal gas turbine blade applications. *Aerosp. Sci. Technol.*, 3(8):513–523, 1999.

[138] J. Gonzalez-Julian, S. Onrubia, M. Bram, and O. Guillon. Effect of sintering method on the microstructure of pure Cr_2AlC MAX phase ceramics. *J. Ceram. Soc. Jpn.*, 124(4):415–420, 2016.

List of Figures

144

List of Tables

Acknowledgment

I would like to thank all people who supported me to write this thesis. The acknowledgment addresses everyone equally, the order of mentioning shall not indicate a grading of the support. In particular I would like to thank the following people:

Prof. Christian Linsmeier hat mir als Institutsleiter und Doktorvater die Möglichkeit geboten diese Arbeit anzufertigen. Während meiner Zeit als Doktorand hat er mir regelmäßig erlaubt an Konferenzen und Fortbildungen teilzunehmen und einen wichtigen Beitrag bei der fachlichen Betreuung geleistet. Danke.

Prof. Achim von Keudell hat mir als Gutachter die Möglichkeit gegeben, die vorliegende Arbeit zu erstellen. Danke.

Dr. Andrey Litnovsky очень поддерживал эту работу в течение всего времени. Он предложил множество полезных идей и неоднократно помогал советом: результаты экспериментов неоднократно обсуждались и он дал множество рекомендаций по усовершенствованию научных статей, презентаций и данной диссертации. Кроме того, руководя нашей небольшой группой Smart Alloys, он всегда поддерживал прекрасную и тёплую научную атмосферу. Спасибо.

Tobias Wegener hat mich während meiner Masterarbeit für das Thema begeistert. Auch im weiteren Verlauf der Doktorarbeit stand er immer für tiefgreifende, wissenschaftliche Diskussionen zur Verfügung und hat bei der praktischen Ausführung vieler Arbeiten im Labor geholfen. Mit seiner Doktorarbeit hat er einen wichtigen Beitrag zu den Grundlagen geleistet, auf denen diese Arbeit aufbaut. Danke.

Dr. Jesus Gonzalez-Julian ha proporcionado valiosas aportaciones de su experiencia en la aleación mecánica de polvo y su sinterización. Además, operó el dispositivo para la sinterización asistida por campo para compactar muestras. Gracias.

Dr. Xiaoyue Tan 给予了实验室宝贵的支持。他多次操作planetary ball mill，提供机械合金粉末。此外，他推动了含锆智能合金的研究，这带来了新的，有趣的结果。谢谢。

Dr. Marcin Rasiński cierpliwie nauczył mnie obsługi przyrządu FIB/SEM. Był zawsze otwarty na dyskusje o technice pomiarów i nowych wyników. Dziękuję.

Dr. Uwe Breuer hat die SIMS Messungen durchgeführt und in ausführlichen Diskussionen der Ergebnisse zu einem guten Verständnis beigetragen. Danke.

Dr. Ivan Povstugar   провел измерения APT и значительно помог в интерпретации и визуализации результатов диагностики. Он всегда был готов обсудить полученные результаты, и не жалел времени на то, чтобы лишний раз проверить данные и найти ответы на поставленные вопросы. Спасибо.

Dr. Jan S. Wróbel   wykonał modelowanie stopów inteligentnych analogicznie do jego pracy o HEA. W połączeniu z dyskusją wyników poprawiło to zrozumienie stopów inteligentnych. Dziękuję.

Dr. Yiran Mao   致力于W-fibre reinforced W 项目。他烧结了含有智能合金的W 纤维，这是合并这两个概念的重要一步。谢谢。

Beatrix Göths   stand im Polierlabor immer mit wichtigen Empfehlungen zur Oberflächenpräparation für Wolframlegierungen zur Seite. Danke.

Freimut Koch   hat mich während meiner Masterarbeit für das Thema begeistert und mich in die Thermogravimetrie eingeführt. Danke, in stillem Andenken.

Dr. Mark Gilbert   has contributed to an improved understanding on neutron irradiation and activation of materials in a fusion device. Further, he helped to initiate the collaboration between Warsaw University of Technology, Culham Science Centre, and Forschungszentrum Jülich on modelling of smart alloys. Thank you.

Dr. Martin Bram   hat die Ausstattung am IEK-1 zur Verfügung gestellt und sich mit Ideen für neue Untersuchungen in die wissenschaftliche Arbeit eingebracht. Danke.

Karsten Schlüter   hat im Rahmen einer europäischen Zusammenarbeit komplementäre Untersuchungen an oxidationsbeständigen Wolframlegierungen gemacht und damit das gemeinsame Verständnis verbessert. Danke.

Janina Schmitz   hat die oxidationsbeständigen Wolframlegierungen unter Plasma-exponierung untersucht. Das hat wichtige, komplimentäre Erkenntnisse geliefert. Im gemeinsamen Büro stand sie immer für wissenschaftlichen Austausch zur Verfügung. Danke.

Dr. Hongchu Du   进行了STEM 测量，提供了对纳米量级智能合金薄膜的一些见解。谢谢。

Andreas Schwaitzer   war bei der Herstellung von speziellen Haltern für Oxidations- und Sublimationsversuche immer hilfsbereit. Danke.

Rudi Caspers   hat die fertig gesinterten Proben zuverlässig geschnitten. Danke.

Dr. Jan Willem Coenen   stand als Gruppenleiter am IEK-4 immer als hilfreicher Ansprechpartner zur Verfügung. Danke.

The IEK-4 as a institute provided an excellent working atmosphere and the infrastructure required for performing the work presented in this thesis. Thank you to all colleagues.

Meiner Familie und meine Freunden für den wichtigen Rückhalt im Leben. Danke.

Lebenslauf

Persönliche Daten

Name:	Felix Klein
Geschlecht:	männlich
Geburtsdatum:	15.08.1990
Geburtsort:	Dresden
Nationalität:	Deutsch

Bildungsweg

1997-2001		Sebastianusschule, Katholische Grundschule Würselen, Deutschland
2001-2010		Gymnasium der Stadt Würselen, Deutschland
	2007/8	Auslandsaufenthalt: Rochedale State High School, Brisbane, Australien
	2010	Abschluss: Abitur mit der Note 1,1
2010-2016		Studium der Physik an der Rheinisch-Westfälischen Technischen Hochschule Aachen, Deutschland
	2013	Abschluss: Bachelor of Science mit der Note 2,5
		Titel der Bachelorarbeit: Confocal Raman Spectroscopy of Graphene on Different Substrates
	2013/4	Studentische Hilfskraft, 2. Physikalisches Institut A, Rheinisch-Westfälische Technische Hochschule Aachen, Deutschland
	2014	Auslandsaufenthalt im Rahmen von ERASMUS an der School of Science, Aalto University, Espoo, Finnland
	2014	Wissenschaftliche Hilfskraft, Department of Micro- and Nanosciences, School of Electrical Engineering, Aalto University, Espoo, Finnland
	2016	Abschluss: Master of Science mit der Note 1,3
		Titel der Masterarbeit: Studies on Yttrium-Containing Smart Alloys
2016-2019		Wissenschaftlicher Mitarbeiter am Forschungszentrum Jülich GmbH, Institut für Energie- und Klimaforschung – Plasmaphysik, Partner of the Trilateral Euregio Cluster (TEC), Jülich, Deutschland; Doktorand der Fakultät für Physik und Astronomie, Ruhr-Universität Bochum, Deutschland

Sprachkenntnisse

Deutsch:	Muttersprache
Englisch:	Verhandlungssicher
Französisch:	Diplôme d'études en langue française DELF A2 (Jahr 2007)
Latein:	Schulkenntnisse, 2 Jahre
Finnisch:	Elementare Sprachverwendung, Niveaustufe A1.2

Curriculum vitae

Personal information

Name:	Felix Klein
Gender:	male
Date of birth:	15/08/1990
Place of birth:	Dresden
Nationality:	German

Education

1997-2001		Sebastianusschule, Catholic Primary School, Würselen, Germany
2001-2010		Gymnasium der Stadt Würselen, Germany
	2007/8	Stay abroad: Rochedale State High School, Brisbane, Australia
	2010	Graduation: Abitur with the mark 1.1
2010-2016		Study of Physics at the Rheinisch-Westfälische Technische Hochschule Aachen University, Germany
	2013	Graduation: Bachelor of Science with the mark 2.5
		Title of the Bachelor thesis: Confocal Raman Spectroscopy of Graphene on Different Substrates
	2013/4	Student research assistant, 2. Physikalisches Institut A, Rheinisch-Westfälische Technische Hochschule Aachen University, Germany
	2014	Stay abroad in the framework of ERASMUS at the School of Science, Aalto University, Espoo, Finland
	2014	Research assistant, Department of Micro- and Nanosciences, School of Electrical Engineering, Aalto University, Espoo, Finland
	2016	Graduation: Master of Science with the mark 1.3
		Title of the Master thesis: Studies on Yttrium-Containing Smart Alloys
2016-2019		Research assistant at the Forschungszentrum Jülich GmbH, Institut für Energie- und Klimaforschung – Plasmaphysik, Partner of the Trilateral Euregio Cluster (TEC), Jülich, Germany; PhD student at the Faculty of Physics and Astronomy, Ruhr-Universität Bochum, Germany

Languages

German: Native speaker
English: Advanced
French: Diplôme d'études en langue française DELF A2 (year 2007)
Latin: School knowledge, 2 years
Finnish: Beginner, level A1.2

Conferences and trainings

2015	Eindhoven, Netherlands	Trilateral Euregio Cluster Meeting Talk: Smart Alloys - Tests and Understanding
2016	Hannover, Germany	DPG-Frühjahrstagung der Sektion Atome, Moleküle, Quantenoptik und Plasmen Talk: Studies on Yttrium-Containing Smart Alloys
2016	Jülich, Germany [Ger]	HITEC Theme Day: Nuclear Waste Disposal and Reactor Safety
2016	Jülich, Ger	HITEC Orientation Week
2016	Jülich, Ger	HITEC Theme Day: Imaging Methods
2016	Jülich, Ger	HITEC Course on Scientific Presentation
2016	Jülich, Ger	HITEC Course on Project Management
2016	Jülich, Ger	HITEC Course on Team Communication
2016	Mol, Belgium	Trilateral Euregio Cluster Meeting Talk: Self-Passivating Smart Alloys for Extreme Environments
2016	Darmstadt, Germany	Materials Science and Engineering Congress Talk: Self-Passivating, Tungsten-Based Smart Alloys for Extreme Environments
2017	Bremen, Germany	DPG-Frühjahrstagung der Sektion Materie und Kosmos Talk: Oxidation Resistance of Plasma-Facing Tungsten Alloys
2017	Karlsruhe, Germany	Karlsruhe International School on Fusion Technologies Poster: Oxidation Behavior of Tungsten-Based Smart Alloys in High Temperatures
2017	Greifswald, Ger	HITEC Theme Day: Fusion
2017	Aomori, Japan	International Conference on Fusion Reactor Materials Poster: Oxidation Resistance of Plasma-Facing Tungsten Alloys
2017	Aomori, Japan	International Energy Agency - Tungsten Workshop Talk: Progress in R&D on Smart Tungsten Alloys - Oxidation Resistance and Plasma Performance
2017	Erlangen, Germany	DPG-Frühjahrstagung der Sektion Atome, Moleküle, Quantenoptik und Plasmen Talk: Tungsten Smart Alloys for the First Wall Armor of Fusion Power Plants

2018	Jülich, Ger	HITEC Course on Getting Published
2018	Delft, Netherlands	HITEC Graduiertenschule Retreat Poster: Oxidation Resistance of Plasma-Facing Tungsten Alloys
2018	Jülich, Germany	HITEC Theme Day: Mitigation of Climate Change: How to achieve the Paris goals? And why?
2018	San Sebastian, Spain	Eurofusion Task Meeting on Self-Passivating Tungsten-Based Alloys Talk: First Results on Bulk W-Cr-Zr; Oxidation and Sublimation of W-Cr-Y Alloys in Humid Air
2018	Weert, Netherlands	Carolus Magnus Summer School on Plasma and Fusion Energy Physics Poster: Sublimation of Advanced Tungsten Alloys Under DEMO Relevant Accidental Conditions
2018	Giardini Naxos, Italy	30th Symposium on Fusion Technology Poster: Sublimation of Advanced Tungsten Alloys Under DEMO Relevant Accidental Conditions
2018	Aix-en-Provence, France	FuseNet PhD Event Talk: Smart Tungsten Alloys for Safer Operation of Future Fusion Power Plants
2019	Karlsruhe, Germany	Eurofusion Monitoring Meeting Talk: Manufacturing of bulk smart alloys systems and thermo-mechanical testing

Used abbreviations:
DPG - German Physical Society
HITEC - Helmholtz Interdisciplinary Doctoral Training in Energy and Climate Research

Publications

- S. Engels, B. Terrés, **F. Klein**, S. Reichardt, M. Goldsche, S. Kuhlen, K. Watanabe, T. Taniguchi, and C. Stampfer. Impact of thermal annealing on graphene devices encapsulated in hexagonal boron nitride. *Physica Status Solidi B*, 251(12):2545-2550, 2014.

- T. Wegener, **F. Klein**, A. Litnovsky, M. Rasinski, J. Brinkmann, F. Koch, and Ch. Linsmeier. Development of yttrium-containing self-passivating tungsten alloys for future fusion power plants, *Nuclear Materials and Energy*, 9:394-398, 2016.

- A. Litnovsky, T. Wegener, **F. Klein**, Ch. Linsmeier, M. Rasinski, A. Kreter, B. Unterberg, M. Vogel, S. Kraus, U. Breuer, C. Garcia-Rosales, and A. Calvo, N. Ordas. Smart alloys for a future fusion power plant: First studies under stationary plasma load and in accidental conditions, *Nuclear Materials and Energy*, 12:1363-1367, 2016.

- T. Wegener, **F. Klein**, A. Litnovsky, M. Rasinski, J. Brinkmann, F. Koch, Ch. Linsmeier. Development and analyses of self-passivating tungsten alloys for DEMO accidental conditions, *Fusion Engineering and Design*, 124:183-186, 2017.

- A. Litnovsky, T. Wegener, **F. Klein**, Ch. Linsmeier, M. Rasinski, A. Kreter, X. Y. Tan, J. Schmitz, J. W. Coenen, Y. Mao, J. Gonzalez-Julian, and M. Bram. New oxidation-resistant tungsten alloys for use in the nuclear fusion reactors, *Physica Scripta*, T170:014012, 2017.

- A. Litnovsky, T. Wegener, **F. Klein**, Ch. Linsmeier, M. Rasinski, A. Kreter, B. Unterberg, J. W. Coenen, H. Du, J. Mayer, C. Garcia-Rosales, A. Calvo, and N. Ordas. Smart tungsten alloys as a material for the first wall of a future fusion power plant, *Nuclear Fusion*, 57:066020, 2017.

- A. Litnovsky, T. Wegener, **F. Klein**, Ch. Linsmeier, M. Rasinski, A. Kreter, X. Y. Tan, J. Schmitz, Y. Mao, J. W. Coenen, M. Bram, and J. Gonzalez-Julian. Advanced smart tungsten alloys for a future fusion power plant, *Plasma Physics and Controlled Fusion*, 59(6):064003, 2017.

- **F. Klein**, T. Wegener, A. Litnovsky , M. Rasinski , X. Y. Tan, J. Schmitz, Ch. Linsmeier , J. W. Coenen, H. Du, J. Mayer, and U. Breuer. On Oxidation Resistance Mechanisms at 1273 K of Tungsten-Based Alloys Containing Chromium and Yttria, *Metals*, 8(7):488, 2018.

- J. Schmitz, A. Litnovsky, **F. Klein**, T. Wegener, X. Y. Tan, M. Rasinski, A. Mutzke, P. Hansen, A. Kreter, A. Pospieszczyk, S. Möller, J. W. Coenen, Ch. Linsmeier, U. Breuer, J. Gonzalez-Julian, and M. Bram. WCrY smart alloys as advanced plasma-facing materials – exposure to steady-state pure deuterium plasmas in PSI-2, *Nuclear Materials and Energy*, 15:220-225, 2018.

- **F. Klein**, T. Wegener, A. Litnovsky, M. Rasinski, X. Y. Tan, J. Gonzalez-Julian, J. Schmitz, M. Bram, J. W. Coenen, and Ch. Linsmeier. Oxidation resistance of bulk plasma-facing tungsten alloys, *Nuclear Materials and Energy*, 15:226-231, 2018.

- A. Litnovsky, **F. Klein**, J. Schmitz, T. Wegener, Ch. Linsmeier, M. R. Gilbert, M. Rasinski, A. Kreter, X. Y. Tan, Y. Mao, J. W. Coenen, M. Bram, and J. Gonzalez-Julian. Smart first wall materials for intrinsic safety of a fusion power plant, *Fusion Engineering and Design*, 136(B):878-882, 2018.

- X. Y. Tan, **F. Klein**, A. Litnovsky, T. Wegener, J. Schmitz, Ch. Linsmeier, J. W. Coenen, U. Breuer, M. Rasinski, P. Li, L. M. Luo, and Y. C. Wu. Evaluation of the high temperature oxidation of W-Cr-Zr self-passivating alloys, *Corrosion Science*, 147:201-211, 2019.

- **F. Klein**, A. Litnovsky, T. Wegener, X. Y. Tan, J. Gonzalez-Julian, M. Rasinski, J. Schmitz, Ch. Linsmeier, M. Bram, and J. W. Coenen. Sublimation of advanced tungsten alloys under DEMO relevant accidental conditions. *Fusion Engineering and Design*, in press, 2019.

- J. Schmitz, A. Litnovsky, **F. Klein**, X. Y. Tan, U. Breuer, M. Rasinski, S. Ertmer, A. Kreter, J. Gonzalez-Julian, M. Bram, J. W. Coenen, and Ch. Linsmeier. Argon-seeded plasma exposure and oxidation performance of tungsten-chromium-yttrium smart alloys. *Tungsten*, 2661-8036:1–10, 2019.

Schriften des Forschungszentrums Jülich
Reihe Energie & Umwelt / Energy & Environment

JÜLICH
Forschungszentrum